NUREG/CR-3689 Vol. I
ANL-83-85 Vol. I

NUREG/CR-3689 Vol. I
ANL-83-85 Vol. I

MATERIALS SCIENCE AND TECHNOLOGY DIVISION LIGHT-WATER-REACTOR SAFETY RESEARCH PROGRAM: QUARTERLY PROGRESS REPORT

January – March 1983

ARGONNE NATIONAL LABORATORY, ARGONNE, ILLINOIS
Operated by THE UNIVERSITY OF CHICAGO

Prepared for the Office of Nuclear Regulatory Research
U. S. NUCLEAR REGULATORY COMMISSION
under Interagency Agreement DOE 40-550-75

Argonne National Laboratory, with facilities in the states of Illinois and Idaho, is owned by the United States government, and operated by The University of Chicago under the provisions of a contract with the Department of Energy.

Available from

GPO Sales Program
Division of Technical Information and Document Control
U. S. Nuclear Regulatory Commission
Washington, D.C. 20555

and

National Technical Information Service
Springfield, Virginia 22161

NUREG/CR-3689 Vol. I
ANL-83-85 Vol. I

(Distribution Codes:
R3 and R5)

ARGONNE NATIONAL LABORATORY
9700 South Cass Avenue
Argonne, Illinois 60439

MATERIALS SCIENCE AND TECHNOLOGY DIVISION LIGHT-WATER-REACTOR SAFETY RESEARCH PROGRAM: QUARTERLY PROGRESS REPORT

January—March 1983

Date Published: April 1984

Previous reports in this series

ANL-82-41 Vol. I	January—March 1982
ANL-82-41 Vol. II	April—June 1982
ANL-82-41 Vol. III	July—September 1982
ANL-82-41 Vol. IV	October—December 1982

Prepared for the Division of Reactor Safety Research
Office of Nuclear Regulatory Research
U. S. Nuclear Regulatory Commission
Washington, D. C. 20555
Under Interagency Agreement DOE 40-550-75

NRC FIN Nos. A2016, A2017, A2212, A2243

MATERIALS SCIENCE AND TECHNOLOGY DIVISION
LIGHT-WATER-REACTOR SAFETY
RESEARCH PROGRAM:
QUARTERLY PROGRESS REPORT

January-March 1983

ABSTRACT

This progress report summarizes the Argonne National Laboratory work performed during January, February and March 1983 on water reactor safety problems. The research and development areas covered are Environmentally Assisted Cracking in Light Water Reactors, Transient Fuel Response and Fission Product Release, Clad Properties for Code Verification, and Long-Term Embrittlement of Cast Duplex Stainless Steels in LWR Systems.

NRC Fin No.	FIN Title
A2016	Transient Fuel Response and Fission Product Release
A2017	Clad Properties for Code Verification
A2212	Environmentally Assisted Cracking in Light Water Reactors
A2243	Long-Term Embrittlement of Cast Duplex Stainless Steels in LWR Systems

TABLE OF CONTENTS

TABLE OF CONTENTS (Contd.)

TABLE OF CONTENTS (Contd.)

MATERIALS SCIENCE AND TECHNOLOGY DIVISION
LIGHT-WATER-REACTOR SAFETY
RESEARCH PROGRAM:
QUARTERLY PROGRESS REPORT

January-March 1983

EXECUTIVE SUMMARY

I. ENVIRONMENTALLY ASSISTED CRACKING IN LIGHT-WATER REACTORS[a]

Six cracks, including two field-induced IGSCC specimens and two thermal-fatigue cracks, have been installed in the acoustic leak detection facility. The loading system has been modified so that the cracks can be stresses at levels that are typical of the in-reactor case. As expected, the IGSCC specimens produce stronger acoustic signals than the thermal-fatigue cracks at equivalent flow rates. Despite significant differences in crack geometry, the acoustic signals from the two IGSCC specimens are virtually identical in the frequency range 200-400 kHz. Thus the quantitative correlations between the acoustic signals and leak rate in the 300-400 kHz band are quite similar for the two cracks. The sensitivity of the acoustic leak detection system installed on the recirculation header sweepolet weld at Hatch-I has been examined. Because the background noise in the 200-400 kHz band is very low at this location, even small leaks (0.002 gal/min) can be detected. However, the system has a very limited dynamic range and would saturate at a 0.006-gal/min leak rate; also, it may be susceptible to spurious alarms caused by benign leakage at relatively large distances.

Samples of centrifugally cast stainless steel have been examined to identify optimal ultrasonic testing conditions for these materials. Both anisotropic and isotropic materials were considered. For the isotropic materials, 0.5-MHz shear waves appear to provide the best combination of penetration and sensitivity for manual inspection. For anisotropic materials, 1-MHz longitudinal waves appear to be the best approach.

---

[a]RSR FIN Budget No. A2212; RSR Contact: J. Muscara.

Additional constant-extension-rate (CERT) test facilities have been completed. In these systems, the specimens are electrically isolated to permit use of the electric potential drop method for in-situ crack length measurements. Weldments prepared with a variety of alternative fabrication and residual stress improvement techniques, such as IHSI, HSW, LPHSW, and CRC, are being subjected to low-temperature long-term aging.

Transgranular stress corrosion cracking was observed in a Type 316NG SS weldment subjected to CERT testing in an environment with 0.2 ppm dissolved oxygen and 0.2 ppm chloride. Tests on the relative susceptibility of Types 304, 316, and 316NG SS are continuing. In tests comparing the effects of sulfuric acid and sodium sulfate additions, very small differences in susceptibility were observed; this suggests that solution pH is of secondary importance compared to the presence of critical anions such as sulfate. An analysis of the effects of strain rate in the CERT test has been developed; it assumes that the stress corrosion crack growth rate is dependent on the crack-tip strain rate and that the final mechanical failure of the specimen can be determined in terms of the conventional elastic-plastic fracture parameter J. Good agreement is obtained between the results of the analysis and test results over a fairly wide range of strain rates.

The effect of frequency and load ratio on stress corrosion crack growth rates is being examined. Although, as noted previously, the CERT tests correlated very well in terms of a crack-tip strain rate, such an approach was unsuccessful in the case of the fracture mechanics tests. This may reflect the inadequacy of the linear elastic fracture mechanics expression for the crack-tip strain rate rather than any fundamental problem with the approach.

Additional information has been obtained on the effect of dissolved oxygen, hydrogen, and sulfate on the stress corrosion susceptibility of sensitized Type 304 SS. As the dissolved oxygen level is decreased, the intergranular cracking susceptibility of the material decreases. The critical level of dissolved oxygen is a function of the impurity level. Dissolved hydrogen per se seems to have a minor effect on material

behavior, and the beneficial effects of hydrogen additions to the feedwater of a BWR are due to subsequent reduction of the dissolved oxygen concentration in the coolant in the recirculation piping. Our results clearly indicate that continuous additions of hydrogen will decrease IGSCC susceptibility by a considerable margin provided impurities are also maintained at very low levels.

II. TRANSIENT FUEL RESPONSE AND FISSION PRODUCT RELEASE[b]

The development of PARAGRASS-MOD 1 was completed this quarter. Also completed was an interim model description and user's guide, which constitutes the main part of the present report. PARAGRASS is an extremely efficient, mechanistic computer code with the capability of modeling steady-state and transient fission product behavior. The models of PARAGRASS are based on the more detailed ones in FASTGRASS. As there are no significant differences in the methodology of the two codes, PARAGRASS provides a comprehensive treatment of fission product behavior. The major differences between PARAGRASS and FASTGRASS are in the treatment of volatile fission products, and in models for the migration of fission products up the temperature gradient. PARAGRASS is ideally suited for incorporation into a whole-core accident analysis code which has the capability of providing PARAGRASS with the relevant fuel operating conditions (e.g., fuel temperatures). PARAGRASS includes a driver which accepts fuel operating conditions; it can be directly interfaced with a thermal-mechanical code with a minimum of difficulty by invoking an appropriate update. PARAGRASS has undergone verification with available steady-state and transient experimental data on fission gas behavior.

---

[b]RSR FIN Budget No. A2016; RSR Contact: G. P. Marino.

III. CLAD PROPERTIES FOR CODE VERIFICATION[c]

Zircaloy fuel cladding is susceptible to local breach-type failures during power transients in LWRs because of stresses imposed by differential thermal expansion of the fuel and cladding. In this program, the effect of stress state, strain rate, and temperature on the deformation characteristics of irradiated Zircaloy fuel cladding is being investigated to provide mechanical-property information and a failure criterion for the cladding under loading conditions conducive to pellet-cladding interaction (PCI). The information will be used in the development of codes to analyze PCI in fuel rods from power ramp experiments in test reactors, and to evaluate the susceptibility of extended-burnup fuel elements and new fuel element designs in commercial reactors to PCI failures during power transients.

SEM examination of the fracture surface morphologies of the irradiated Big Rock Point (BWR) and H. B. Robinson (PWR) fuel cladding has been completed in this reporting period. For cladding tube specimens that failed in a brittle PCI-like manner, characteristic pseudocleavage-plus-fluting maps of the fracture surfaces were constructed. Based on the fracture surface maps, a parameter that defines the extent of cladding wall-thickness penetration by pseudocleavage plus fluting has been tabulated.

TEM-HVEM examination of H. B. Robinson fuel cladding, which exhibits brittle-type PCI-like failures in stress-rupture experiments, confirmed the previously reported observation of copious amounts of Zr_3O precipitates in the vicinity of a failure site that is characterized by extensive pseudocleavage plus fluting. Besides the two previously reported orientational relationships between the α-Zr matrix (α_I) and Zr_3O phase (α_{II}), an additional orientation has been identified. It is believed that the brittle-type PCI-like failures of the Big Rock Point and H. B. Robinson fuel cladding produced during the gas pressurization tests are associated with segregation of oxygen to dislocation substructures and irradiation-induced defects, which lead to the formation of the Zr_3O phase, an immobilization of dislocations, and minimal plastic

---

[c]RSR FIN Budget No. A2017; RSR Contact: H. H. Scott.

deformation in the material. The mechanism of oxygen segregation has been discussed in association with strain aging and radiation-induced segregation (RIS) phenomena reported in the literature.

Several specimens of high-burnup H. B. Robinson fuel cladding have been fractured at 325°C by the expanding-mandrel technique. Under this loading condition, as well as during in-reactor service, the effective stress at the inner surface is several times greater than that at the outer surface. Consequently, cracks should initiate on the inner surface and propagate toward the outer surface. A preliminary examination of the fracture morphologies of these specimens supports the prediction. Detailed examinations by SEM and TEM will be reported later.

IV. LONG-TERM EMBRITTLEMENT OF CAST DUPLEX STAINLESS STEELS IN LWR SYSTEMS[d]

A program has been initiated to investigate the significance of in-service embrittlement of cast duplex stainless steels under LWR operating conditions. The objectives of the program are to (1) characterize and correlate the microstructure of in-service reactor components and laboratory-aged material with loss of fracture toughness and identify the mechanism of embrittlement, (2) determine the validity of laboratory-induced embrittlement data for predicting the toughness of component materials after long-term aging at reactor operating temperatures, (3) characterize the loss of fracture toughness in terms of fracture mechanics parameters in order to provide the data needed to assess the safety significance of embrittlement, and (4) provide additional understanding of the effects of key compositional and metallurgical variables on the kinetics and degree of embrittlement.

Various experimental and commercial heats of ASTM A351 and A451 grade of CF-8, -8M, and -3 cast stainless steel were procured in different product forms and section thicknesses. The composition of the experimental heats was varied to provide different concentrations of nickel, chromium, carbon, and

---

[d]RSR FIN Budget No. A2243; RSR Contact: J. Muscara.

nitrogen in the material and ferrite contents in the range of 3 to 30 vol. %. Material will be available for Charpy impact tests and microstructural studies over the entire range of compositions. A more restrictive set of compositions will be chosen for J_R curve testing.

The initial effort is focused on microstructural studies on aged cast stainless steels. Material from three heats of cast CF-8 and -8M stainless steel, aged for up to 70,000 h at 300, 350, and 400°C, was obtained from George Fisher, Ltd. of Switzerland. Two single-phase ferritic alloys and a cast duplex stainless steel were used to develop the technique for preparing transmission electron microscope samples. Work on sample preparation has reached a stage where foils from cast duplex material can be produced routinely with a high success rate. Preliminary results indicate that aging of the ferritic alloys and the duplex stainless steel at 475°C for 1000 h produced a mottled structure representative of the α' phase. However, the α' precipitates were not observed in cast stainless steel aged for 10,000 h at 400°C.

I. ENVIRONMENTALLY ASSISTED CRACKING IN LIGHT WATER REACTORS

Principal Investigators:
W. J. Shack, F. F. Kassner, D. S. Kupperman, T. N. Claytor,
J. Y. Park, P. S. Maiya, W. E. Ruther,
and F. A. Nichols

The objective of this program is to develop an independent capability for prediction, detection, and control of intergranular stress corrosion cracking (IGSCC) in light-water reactor (LWR) systems. The program is primarily directed at IGSCC problems in existing plants, but also includes the development of recommendations for plants under construction and future plants. The scope includes the following: (1) development of the means to evaluate acoustic leak detection systems objectively and quantitatively; (2) evaluation of the influence of metallurgical variables, stress, and the environment on IGSCC susceptibility, including the influence of plant operations on these variables; and (3) examination of practical limits for these variables to effectively control IGSCC in LWR systems. The initial experimental work concentrates primarily on problems related to pipe cracking in LWR systems. However, ongoing research work on other environmentally assisted cracking problems involving pressure vessels, nozzles, and turbines will be monitored and assessed, and where unanswered technical questions are identified, experimental programs to obtain the necessary information will be developed to the extent that available resources permit.

The effort is divided into six subtasks: (A) Leak Detection and Nondestructive Evaluation; (B) Analysis of Sensitization; (C) Crack Growth Rate Studies; (D) Evaluation of Nonenvironmental Corrective Actions; (E) Evaluation of Environmental Corrective Actions; and (F) Mechanistic Studies. These subtasks reflect major technical concerns associated with IGSCC in LWR systems, namely: leak and crack detection, the role of materials susceptibility, the role of stress in crack initiation and propagation, and the role of the environment. The program seeks to evaluate potential solutions to IGSCC problems in LWRs, both by direct experimentation (including full-scale welded pipe tests) and through the development of a better basic understanding of the various phenomena.

A. Leak Detection and Nondestructive Evaluation (D. S. Kupperman, T. N. Claytor, R. Groenwald,* and R. N. Lanham)

1. Introduction

a. Leak Detection

Early detection of leaks in nuclear reactors is necessary in order to identify deteriorating or failed components and minimize the release of radioactive materials. Before a nuclear power facility can be placed into operation, the NRC requires that operational leak-detection systems of various kinds be installed. Some allowance is made for leakage from packing, shaft seals, etc., and the flow from these "identified leaks" is monitored during plant operation. Thus, even with the system operating normally, there may be some accumulation of water in the sumps, with a concomitant increase in the level of radioactivity. However, it is expected that these levels of radioactivity and leakage will be reasonably constant with time.

No currently available single leak-detection method combines optimal leakage detection sensitivity, leak-locating ability, and leakage measurement accuracy. For example, although quantitative leakage determination is possible with condensate flow monitors, sump monitors, and primary coolant inventory balance, these methods are not adequate for locating leaks and are not necessarily sensitive enough to meet code requirements. Acoustic methods represent the most promising area for improvement in leak detection. They have the best chance of success when specific welds are monitored, and the least when a few probes are used to monitor many welds. However, the ability to locate leaks and quantify leak rates using acoustic techniques is not well established, especially since virtually no data are available on acoustic signals from field-induced IGSCC.

---

*GARD, Inc., Niles, Illinois.

b. Nondestructive Evaluation

For safety-related as well as practical reasons, it is desirable to detect any cracks in the primary and secondary coolant boundaries of LWRs even before leakage occurs, and to fix them within a reasonable length of time. This is in accord with the NRC "defense-in-depth" philosophy, which requires the consideration of all possible efforts that might prevent a nuclear accident. In recent years, numerous cracks have been discovered in coolant systems of LWRs. Although the main problems have been in BWR primary coolant lines, cracking has occurred in PWR feedwater piping and low-temperature, low-pressure lines near the spent-fuel storage pool. Unfortunately, many of these cracks were missed during ultrasonic ISI and detected only because of leakage, thereby raising doubts concerning the capability of ultrasonic ISI to detect cracks. The present ultrasonic testing procedures for ferritic weldments (ASME Code Sections V and XI) do not appear to be adequate for the detection and evaluation of IGSCC in austenitic stainless steel (SS) piping. Indeed, the detection of IGSCC before the cracks have grown large enough to cause a leak, and the detection, location, and sizing of leaks once they occur, are very difficult technical goals to achieve. IGSCC that can be detected by conventional ultrasonic testing under laboratory conditions may be missed during a field examination by even the most skillful operator.

c. Objectives

The objectives of this subtask are to (1) develop an independent capability to assess the effectiveness of current and proposed techniques for acoustic leak detection (ALD) in reactor coolant systems, (2) develop a strategy for hardware realization, and (3) examine potential improvements in ultrasonic methods for detection of IGSCC and inspection of cast SS. The program will establish whether meaningful quantitative data on leak rates and location can be obtained from acoustic signatures of leaks due to cracks (IGSCC and fatigue) in low- and high-pressure lines, and whether these can be distinguished from other types of leaks. It will also establish calibration procedures for acoustic data acquisition and show whether advanced signal processing can be employed to enhance the adequacy of ALD schemes.

2. Technical Progress

a. Leak Detection

(1) Acoustic Leak Data

The modification of the ALD test facility is continuing. Two fatigue cracks and two thermal-fatigue cracks (TFCs), all laboratory-grown, have now been welded into the pipe run, and tests have begun with these cracks. A second field-induced crack, designated IGSCC #2, has also been welded into the pipe run. In order to produce leakage through IGSCC #2, it was first necessary to remove corrosion products from the crack with DOWCON-1 (Dow Chemical). In addition, the outer surface of the specimen was ground down about 4 mm from the top of the weld crown to increase the exit length of the crack from 4 to 10 mm (the inner-surface length was 13 mm). In spite of these measures, a very low leak rate of ∿0.001 gal/min (3.8 cm^3/min) was observed in initial tests with IGSCC #2. (In contrast, IGSCC #1, with an exit length of only 2 mm, had a leak rate of ∿0.005 gal/min or 19 cm^3/min.) This leakage could barely be detected acoustically with a 375-kHz receiver ∿20 cm from the source. However, at the time of these initial tests, the loading system was inadequate to apply a stress typical of reactor operating conditions to IGSCC #2. Improvements were subsequently made which allowed loading of the pipe to nearly 70 ksi (480 MPa), a level 50% greater than previously attempted. As a result, the leak rate for IGSCC #2 was increased. A comparison of acoustic spectra of the two IGSCC specimens for leak rates of 0.004 gal/min (15 cm^3/min) indicates virtually identical signals in the frequency range from 200 to 400 kHz (Fig. 1). Below 200 kHz, the signal is ∿5 dB lower for IGSCC #2, presumably because of differences in geometry. These data suggest that geometrical effects may be less significant at frequencies above 200 kHz. Therefore, relating leak rate to acoustic signals may be more reliable at higher frequencies.

Acoustic emission noise generated by the smaller of the two TFCs (designated TFC #1) was measured with the NBS transducer and compared with the noise generated by IGSCC #1. The spectrum levels for the two cracks are shown in Fig. 2. The spectra are similar in shape, but at 400 kHz,

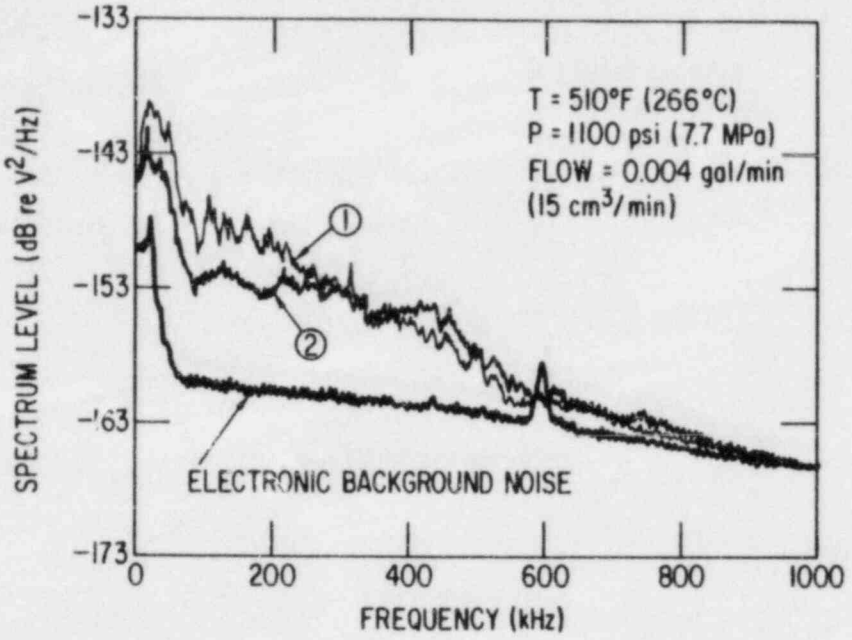

Fig. 1. Comparison of the Acoustic Spectra of Two IGSCC Specimens Tested at the Same Flow Rate, Temperature, and Pressure. Crack lengths at the outer and inner surfaces are 2 and 19 mm, respectively, for IGSCC #1, and 10 and 13 mm, respectively, for IGSCC #2.

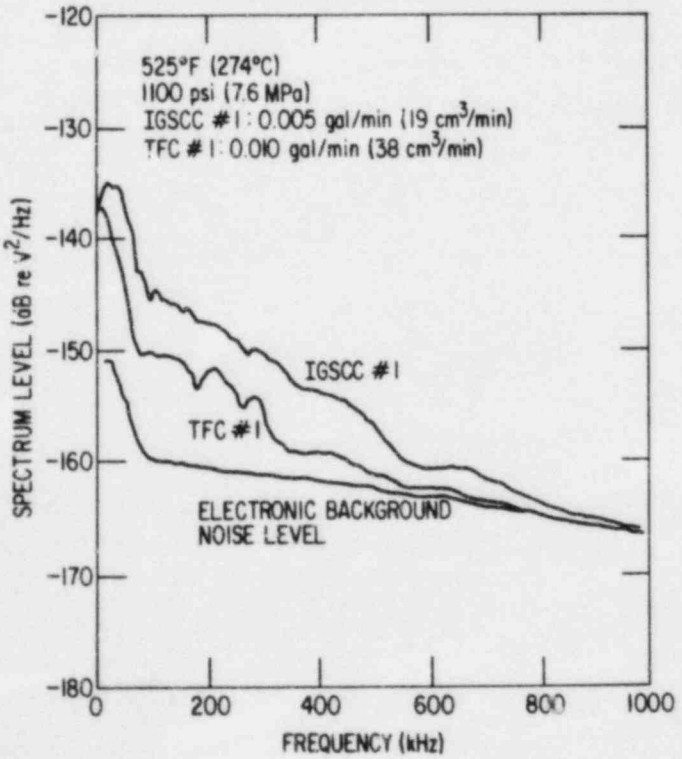

Fig. 2

Comparison of the Acoustic Spectra of an IGSCC and a TFC Specimen.

the noise level from IGSCC #1 is 5 dB or 1.77 times greater than the level produced by TFC #1 even though the leak rate is twice as great for TFC #1. This is consistent with previous observations that IGSCC leaks produce more noise than slit leaks, at equivalent leak rates. The IGSCC exit opening is 2 mm long and 10-20 μm wide, while that of the TFC is ∿26 mm x 100 μm. Consequently, for the same water flow rate, the steam exit velocity for the IGSCC should be a factor of 86 higher than that of the TFC. It is generally accepted[1] that the high-frequency acoustic noise generated by flow through a pipe increases as the third power of the fluid velocity. The present data qualitatively support the dependence of leak noise on leak rate, but owing to the uncertainty of the geometry (crack width vs depth) of the IGSCC and TFC specimens, a quantitative analysis is not possible.

In Fig. 2, two distinct regions in the frequency spectra are evident. There appears to be a transition at 80 kHz in both spectra from a steeply falling $f^{-1.50}$ dependence of noise level on frequency to a more gradual dependence of $f^{-1.30}$ at frequencies greater than 80 kHz. This type of frequency spectrum was seen for almost all the leaks that were tested and could be an identifying feature of the sound-producing mechanisms of the leaks, or it could be due to the acoustic characteristics of the pipe. This effect will be investigated to determine whether it is a characteristic of the leaks themselves.

An important consideration for leak detection is the dependence of the acoustic emission signal on leak rate. This dependence may vary with frequency, depending on the mechanism that produces the sound. To obtain data on acoustic noise output as a function of leak rate and frequency, TFC #1 was stressed from 0 lb to 55 klb (0 to 20,350 kg) and the leak signal was measured in three frequency bands: 30-40, 100-150, and 300-400 kHz. The data obtained (Fig. 3) show that the acoustic signals are correlated with leak rate, but are less dependent on this rate in the highest frequency range examined. Also, the variance in the data decreases at the higher frequencies. The acoustic emission output voltages for the three regions are given by the following expressions:

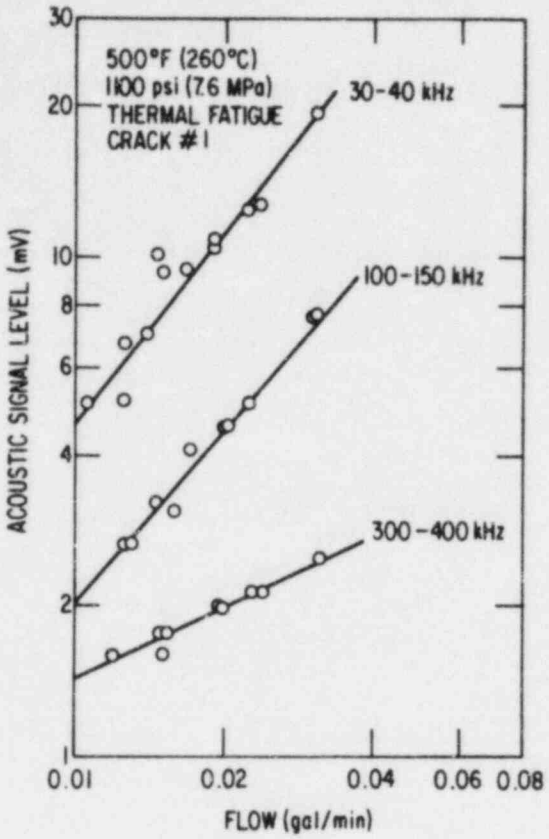

Fig. 3

The Dependence of Acoustic Signal on Leak Rate for a Thermal Fatigue Crack.

$$V = 8.38 \times 10^{-5}\, Q^{1.28} \quad \text{(30-40 kHz)}, \tag{1}$$

$$V = 9.36 \times 10^{-6}\, Q^{1.16} \quad \text{(100-150 kHz)}, \tag{2}$$

$$V = 2.05 \times 10^{-7}\, Q^{0.48} \quad \text{(300-400 kHz)}. \tag{3}$$

In Eqs. (1-3), V is given in terms of spectrum level (V^2/Hz) if Q is in gal/min. The dependence on leak rate in the 300-400 kHz band is the same as that found in a previous study.[2] Because the acoustic output shows different dependences on leak rate at different frequencies, more than one noise-producing mechanism may be involved. At present, it is thought that almost all of the noise from the IGSCC and TFC leaks is due to steam flow. The NBS transducer was found to be sensitive to airborne noise; this could be the cause of some of the signal enhancement at low frequencies. Further tests with the NBS transducer are planned to determine whether the low-frequency sensitivity is a problem.

Attenuation data have also been acquired for water-filled pipes with electronically generated ultrasonic waves in the frequency range from 200 to 400 kHz. The ANL results are consistent with data found in the literature. Figure 4 shows the signal obtained as a function of distance along the pipe run, and the variation in attenuation with azimuthal angle, when a long section of the pipe (indicated in the figure) was filled with water.

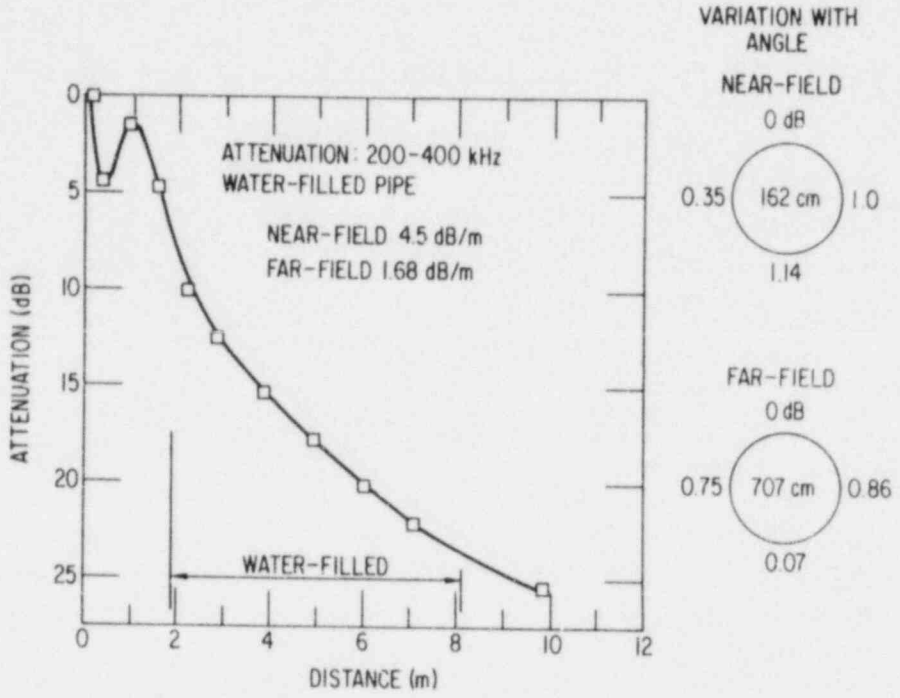

Fig. 4. Attenuation Data for 10-in. Schedule 80 Piping with Water-filled Section. Diagrams at right show variation with azimuthal angle.

(2) Acoustic Background Noise

After ultrasonic testing revealed cracks in the Georgia Power Co. HATCH-1 BWR recirculation header, an ALD system was installed by Georgia Power and Nutech personnel. The transducer and waveguide are similar to those being evaluated at ANL for leak detection. Data from HATCH-1 can give an indication of background noise at the BWR recirculation header sweepolet weld. The HATCH system uses an AET 204A miniature acoustic emission system and an AET AC375L sensor on a 1/2-in.-diam, 10-in.-long threaded stainless steel rod with a flat bottom. The waveguide is threaded through a mounting plate to hold it in direct contact with the pipe.

This system was reproduced and tested at ANL to establish its sensitivity and dynamic range. Figure 5 shows a plot of digital readout (proportional to the rms signal output) vs gain setting for the instrument. In order to approximate the HATCH-1 "B" conditions, ultrasonic waves were generated electronically on the pipe run to simulate background noise. For gains similar to that used in the field, the resulting dotted curve agrees well with the lower HATCH-B curve, which was obtained during reactor operation at 94% full power. At 100% full power, the HATCH-1 "B" readouts increased by about 20%; this is consistent with a model which assumes that the background noise is flow noise and thus increases as the cube of fluid velocity. If one assumes that the reactor power is proportional to fluid velocity and the rms signal is proportional to the acoustic noise level, the data appear reasonable.

The sensitivity of the system is demonstrated by the easily detected increase in signal when a 0.002 gal/min IGSCC leak, at a distance of 50 cm, is added to the simulated background noise (dash-dot line in Fig. 5). These results suggest that at the recirculation header of a BWR at full power, the acoustic background noise in the 200-400 kHz range is only a few dB above the electronic noise.

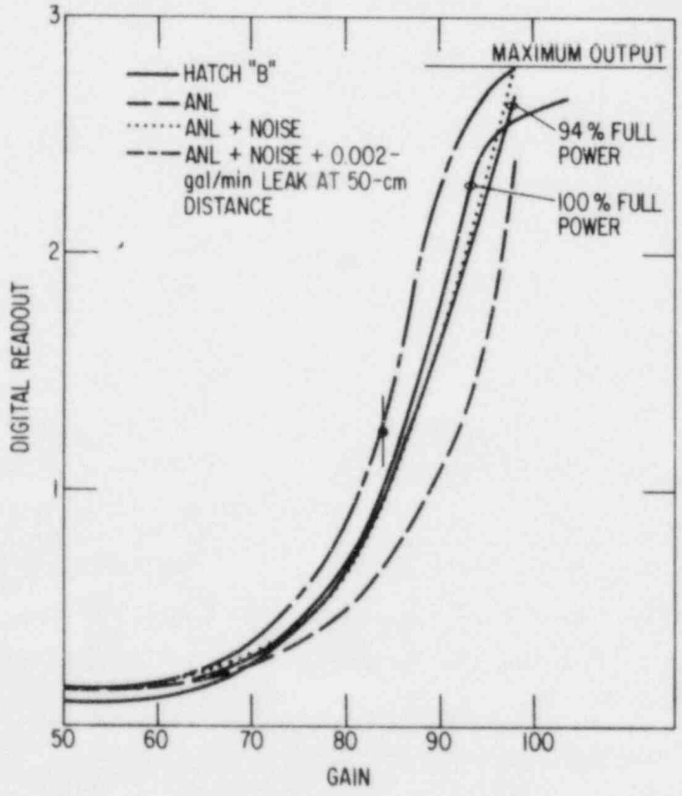

Fig. 5

Digital Readout vs Gain Setting of AET 204A Acoustic Emission System. ANL laboratory results are compared with data from the HATCH BWR monitoring system, with waveguide on header sweepolet. AET 375 transducers were used. The dark circle represents the setting used in the field.

The dynamic range of the system is illustrated in Fig. 6, which shows a strip-chart recording (similar to those made at HATCH) of read-out voltage vs time for leak rates of 0.002 to 0.006 gal/min. Under BWR operating conditions, the ANL system is saturated by the signal from a 0.006-gal/min IGSCC leak at a distance of 50 cm. A broadened dynamic range would clearly be desirable.

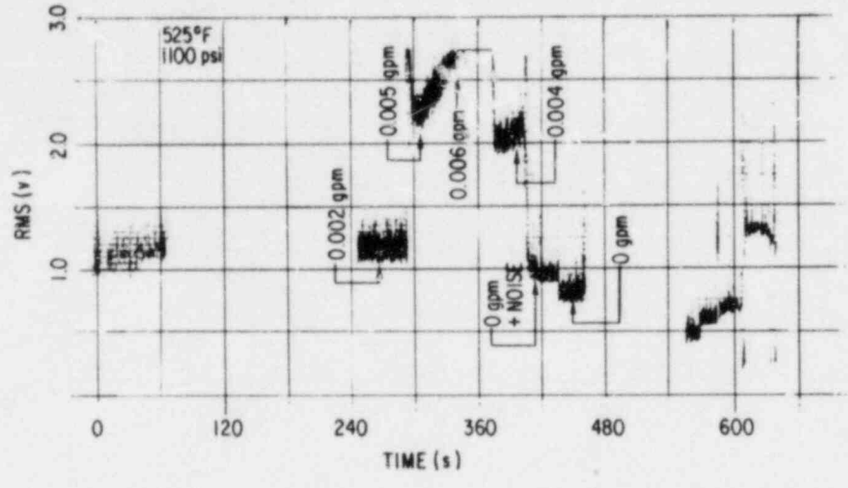

Fig. 6. Dynamic Sensitivity and Range of HATCH System (200-400 kHz).

This example indicates the level of ALD capability that is currently available. There is no source discrimination (a large valve leak can register the same as a small IGSCC leak) and there is no flow rate information. A more sophisticated system is clearly needed to (a) eliminate false calls through improved leak location and characterization data, (b) quantify leak rate through analysis of rms time domain structure and spectral data, and (c) minimize the number of installed transducers in a complete system through reliable design and increased system sensitivity.

(3) Field-implementable Acoustic Waveguide System

Two waveguide systems have been completed. Both designs use a 250-mm-long, 3-mm-diam waveguide rod of Type 304 SS. An AET 375 acoustic emission transducer is attached to the end of the waveguide rod with a spring washer. One system (Fig. 7) is a "quick-connect" type; the waveguide is passed through a plate which is strapped to the outside of the reflective

insulation and the rounded waveguide tip is pressed against the pipe surface with a spring-loading device (10-lb load). Gold foil serves as the couplant. In the other system (Fig. 8), the waveguide tip passes through the insulation and is screwed through a plate that is strapped directly to the pipe outer surface. Silicon grease is used as a couplant. The force applied to the pipe at the waveguide tip is larger than with the spring-loaded system, but not as reliably measured. The analysis of preliminary results indicates that comparable acoustic signal levels can be reached with both designs. The systems are similar in sensitivity to the PNL waveguide and probe (which uses a magnet to hold the waveguide down and is therefore not appropriate for SS piping); an ∿6-dB signal is obtained at a distance of ∿1 m from a 0.005-gal/min leak.

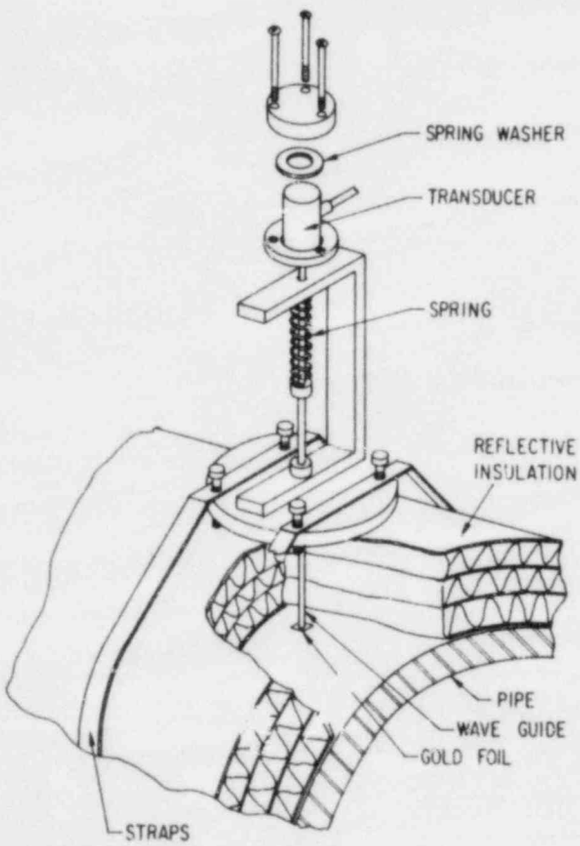

Fig. 7

Schematic of "Quick-Connect" Waveguide Attachment System.

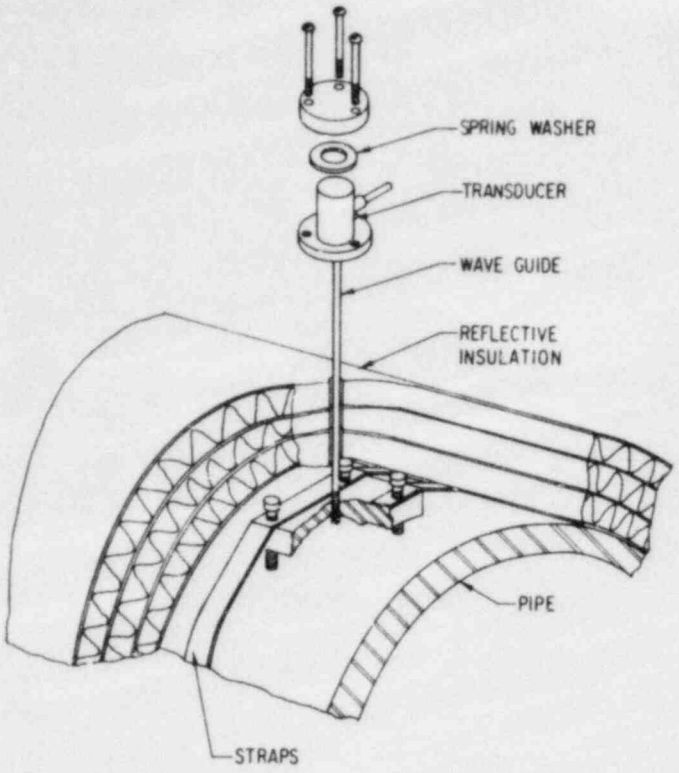

Fig. 8

Schematic of "Screw-In" Waveguide Attachment System.

(4) Development of Breadboard-Type Leak Detector

(a) Coordination of Efforts with PNL. At the NRC's request, a meeting was held with PNL personnel early in the current reporting period to coordinate the current GARD/ANL and PNL efforts on this program. The PNL program is directed at crack growth monitoring in nuclear piping. The PNL system is further along in its development than the GARD/ANL leak detector; a prototype of the PNL system is to be installed on the Watts Bar reactor. Signal bandwidth and amplitude requirements of the two systems, as well as overall system architecture, were discussed. Signal processing is approached differently in the two systems because acoustic emissions from leaks are continuous in nature, whereas burst- or event-type acoustic emission is associated with crack propagation. The benefits of a combined system, however, are significant. An overall reduction in hardware (transducers and preamplifiers) coupled with a corresponding reduction in installation complexity would not only reduce the system cost, but would be looked upon favorably by the nuclear industry. Therefore, the needs of these two systems will be reviewed from time to time to assess whether changes have

occurred that will make the use of common system elements more feasible than it now appears.

PNL personnel plan to modify their system to allow continuous rms data to be taken. At present, there is an overlap in the frequency windows chosen for leak detection and crack growth monitoring. It may be possible to use the same transducer-waveguide system.

(b) Hardware. During the current reporting period, the primary effort was directed to the hardware realization task. The system configuration was first established. The breadboard system, as originally proposed, is shown in Fig. 9. This version utilized a local microcomputer to control data acquisition and to provide operator interface; communication with a minicomputer at GARD was to be accomplished via two modems and a dedicated telephone line. All the data analysis routines would be resident in the minicomputer and would be called remotely from the laboratory satellite system. Similarly, the resultant analyses would be transmitted to the satellite for display and stored in the minicomputer's archives. There might be some latency related to data transmission time, but the on-line data analysis principles would be adequately evaluated with such a breadboard system.

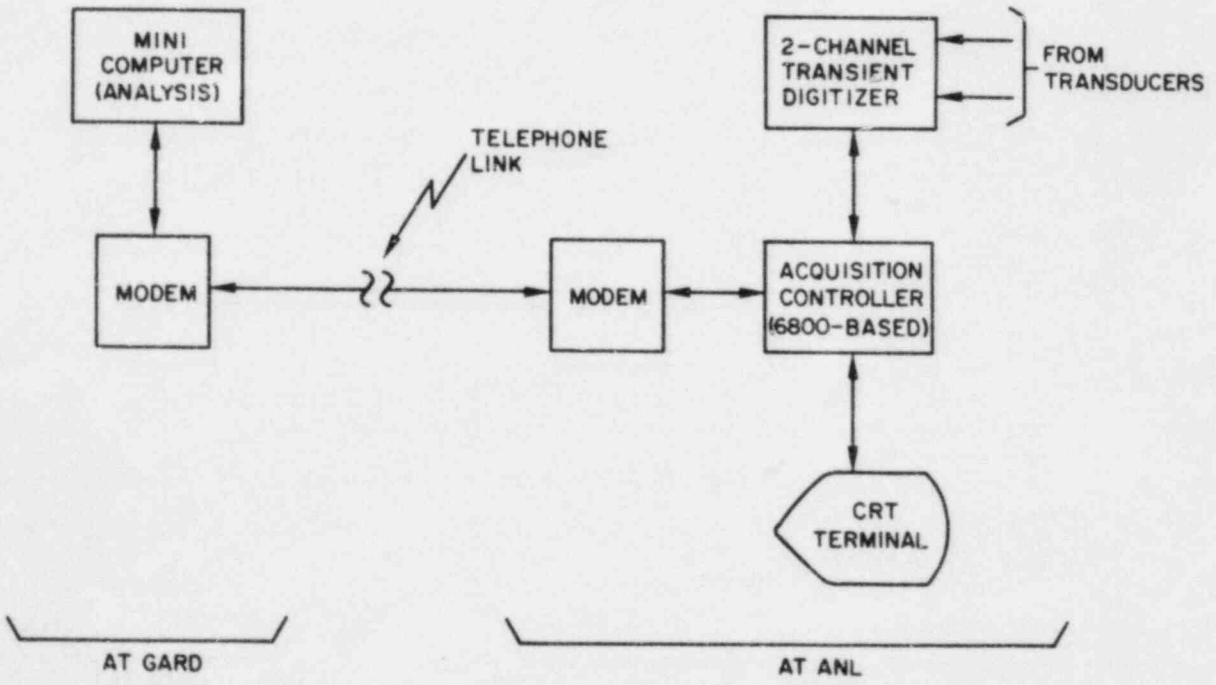

Fig. 9. Proposed Breadboard for Acoustic Emission Leak Detection System.

An alternative that was subsequently considered was the use of a transportable minicomputer with an appropriate front end. This avoids the need for telephone lines and modems and their associated costs along with the efforts associated with establishing a remote inter-computer interface. Currently available at GARD is a Motorola M68000 which was originally thought to be adequate for this application. Such a system would certainly have sufficient computational power to meet the needs of this program; however, software-generating capability is currently limited to a 68000 assembler, which would greatly increase the efforts required to generate the analysis software (i.e., FFT and correlation routines). Fortran could not be made available, owing to licensing restrictions.

An investigation of other available minicomputers narrowed the field to three candidates, which are listed in Table I with pertinent comparison points. They all have comparable hardware capabilities: 256 or 512 kilobytes of RAM and 20-33 megabytes of Winchester disk storage with tape or floppy-disk backup. The Dual and AIM Technology systems utilize the Motorola 68000 CPU, whereas the DEC system has the latest proprietary LSI CPU, which probably has similar or greater capabilities. The Unix operating system used by AIM and Dual is more versatile and "user-friendly" than DEC's RT-11. Both operating systems support the Fortran compilers needed for this project. The greater flexibility of the Unix system, however, provides for easier integration of Fortran-callable routines (not necessarily written in Fortran), which will be helpful in controlling the data acquisition hardware and handling the arrays of data thereby generated. The three Fortran compilers/assemblers were comparable in cost. The DEC system offered an optional Signal Technology package for data analysis at a cost of $6,000. However, public-domain analysis programs are offered by IEEE and others at minimal cost. The Q-bus employed by DEC restricts the user, to some degree, to DEC-supplied hardware, whereas the Multibus and S-100 bus systems are well supported by multiple sources of compatible hardware boards and interfaces. AIM Technology, primarily a board supplier, provides a system which requires customer integration and checkout. The others are supplied ready-to-go with a minimum of inter-chassis cable connection. Although any of these three systems would meet the needs of this project, the attractive cost of the DEC system is outweighed by its unavailability until midyear. The Dual system

was selected because it provides slight advantages in cost and delivery time, and a significant advantage in that customer effort is not required to integrate the system. The system was delivered in February 1983.

TABLE I. Comparison of Minicomputer Capabilities

	Computer System		
	DEC Micro II	AIM Technology	Dual 83/20
CPU	DEC LSI-11 (latest version)	Motorola 68000	Motorola 68000
Operating System	RT-11	UNIX	UNIX
Fortran Software Fee	$1,000	$1,200	$600
External Interface	Q-Bus adapter	Multibus adapter	S-100 interface
RAM (kilobytes)	256	512	512
Mass Storage	20-megabyte Winchester; 1-megabyte floppy disk	33-megabyte Winchester; ½-in. Mag. Tape	20-megabyte Winchester; 1-megabyte floppy disk
Mainframe Bus	DEC Q-Bus	Multibus	S-100 Bus
Approximate Cost	$10,000	$17,000	$13,300
Availability	July-Aug. 1983	30 Days ARO	15 Days ARO
Customer Efforts Needed to Achieve System Operation	None	Customer Responsible for System Integration & Checkout	None

An additional implementation change involved purchasing an off-the-shelf transient digitizer in lieu of fabricating one. The unit that was first considered was the LeCroy TR 8837, a two-channel digitizer that could operate at sampling rates of up to 25 MHz in the dual-channel mode (50-MHz single channel). It was programmable in terms of sampling frequency and pre-trigger mode and had an internal 16 K sample memory. The TR 8837 has since been superseded by a single-channel unit. This has a higher maximum sampling rate (32 MHz), and two or more units can be slaved together in a multiple-channel mode. Interestingly, two of the new units (TR 8837F) are lower in cost than the original dual-channel TR 8837.

All of the LeCroy units are designed for operation in CAMAC enclosures. The use of a crate, crate controller, and S-100 interface will be required. The digitizer and its supporting hardware can be more than adequately covered by the original estimated costs of materials and labor to develop a custom two-channel digitizer. A nine-slot minicrate is proposed, which will provide ample space for all the above-mentioned hardware along with the necessary signal-conditioning hardware (filters, preamps, etc.) to interface transducers with the digitizers. This will result in a neat, workable package for the breadboard system.

(c) Software. The software development for this program is divided into two primary tasks. The first is the evaluation of available data analysis programs to determine their applicability. The available programs are typically in the public domain and are published by IEEE and other sources. The second task is the generation of required analysis routines that are not currently available, along with the mainline programs needed for leak detection. The mainline programs will utilize the analysis routines (both those obtained from other sources and those generated here) as subroutines for flaw detection, location, and characterization. The efforts on this task began when the Dual 83/20 computer system was received. Initial efforts were directed to the evaluation of programs that are currently available from IEEE. Routines were extracted from five source program listings and were modified for this application by (a) restructuring them into subroutine format, (b) redimensioning real and complex arrays to fit the present application, and

(c) manipulating the data arrays to attain compatibility with each author's array format. The subroutines evaluated to date are described in Table II. Included are FFT, correlation, digital filtering, and sample rate conversion routines, all of which may be useful in this project. Also included are some plotting routines which will be of interim value.

(5) Evaluation of Moisture-sensitive Tape

In order to help assess the adequacy of moisture-sensitive tape for comparison with ALD systems, a facility is being assembled to provide simulated leaks to a 2-m-long 304 SS pipe covered with reflective insulation. The pipe will be heated from the inside and steam will be injected under the insulation to simulate a leaking crack. The moisture-sensitive tape will be placed over the insulation; a hole drilled in the insulation will provide a pathway for moisture to reach the tape.

b. Nondestructive Evaluation

(1) Centrifugally Cast Stainless Steel

One major area of difficulty in the ultrasonic inspection of stainless steel (SS) reactor components is the inspection of centrifugally cast stainless steel (CCSS), which is used for piping in pressurized water reactors but is difficult to inspect reliably because of its coarse grains. CCSS samples were examined at frequencies as low as 0.5 MHz to identify optimal ultrasonic testing conditions for this material. Both isotropic and anisotropic samples were tested (the latter are transversely isotropic, owing to the presence of long columnar grains).

Two types of CCSS samples have been evaluated. These samples are both from cast Type 304 SS piping ∿27 in. (∿0.69 m) in diam, but they have different microstructures. Sample A has large grains (1-2 mm in diam) without columnar structure; sample B has large columnar grains (tens of millimeters long and a few millimeters wide). Experiments were performed to determine the degree of texturing in these samples. If the anisotropic CCSS resembled SS weld metal during ultrasonic inspection, then techniques

TABLE II. Summary of Evaluated Software Routines

Main Subroutine	Description
FFT	Implements Jim Cooley's simple decimation-in-time algorithm which computes Fourier coefficients for a complex input sequence. Handles up to 8192 pts. Requires ∿260 words of memory. Performs a 1024-pt. FFT in ∿20 s.
FFT 842	L.R. Rubiner's "fast" FFT algorithm computes Fourier coefficients for a complex input sequence. The summed products required in the calculation are computed iteratively using equations which extend the performance of those used in the above Cooley-Tukey algorithm. Handles up to 8192 pts. Requires ∿1400 words of memory. Performs a 1024-pt. FFT in ∿8 s.
CORR1	Uses classic biased-correlation estimator. Uses most efficient approach in performing the actual correlation; i.e., requires a single call to a complex FFT routine, unlike approaches which require either two calls or a single call of twice the length to a real FFT routine. Does correlation by "sectioning," thus can accommodate any number of input data samples.
FDESIGN	A finite impulse response (FIR) filter design program. Obtains a finite-length impulse response by truncating an infinite-duration impulse response, i.e., by windowing. Allows selection of several window types (Rect., Hamming, ChebyChev). Computes FIR samples for HP, LP, BP, or BS filter types. Handles maximum filter length of 1024. Computes filter characteristics: passband ripple, passband cutoff, and stopband cutoff attenuation.

TABLE II (continued)

Main Subroutine	Description
FCONVERT	Performs sampling-rate conversion (i.e., interpolation or decimation) of a sampled data sequence by the ratio given by L/M. User enters L and M values. Requires FIR filter samples. Accurate and efficient for ratios $\leq$10; higher ratios are better left for programs incorporating several "stages" of conversion.
COPLT	Correlation coefficient Table/Plot routine for line printer.
MAGPR	Fourier magnitude coefficient Table/Plot routine for line printer.

developed for one material would also be applicable to the other. In addition, if the two specimens had different textures, they could be used to determine whether the inspectability of CCSS is related to the degree of anisotropy in the sample.

Angle beam testing in CCSS with columnar grains is often carried out with 1-MHz longitudinal waves propagating at approximately 45° to the long axis of the columnar grains, because a focusing effect occurs at this propagation angle for longitudinal (but not shear) waves. For isotropic CCSS, the problem reduces to one of increasing the ratio of wavelength to grain size. A 65-mm-thick block of isotropic CCSS (grain size of 1-2 mm) containing a 10-mm-deep EDM notch and a 6-mm-diam side-drilled hole was used to compare the effectiveness of shear and longitudinal waves. The sample is shown in Fig. 10. To match the 6-mm wavelength of 1-MHz longitudinal waves, a shear wave frequency of 0.5 MHz was used. Figure 11 shows typical radio frequency signals obtained from the side-drilled hole (upper traces) and notch (lower traces) with normal-incidence shear waves (left) from a Panametrics 1/2-MHz, 1-in.-diam transducer and normal-incidence longitudinal waves (right) from a

Panametrics 1-MHz, 1/2-in.-diam transducer; the transducers were placed on the "slope" of the sample to generate the equivalent of 45°-angle beams. The results indicate that for comparable wavelengths, shear and longitudinal waves generate comparable signals for a side-drilled hole. However, for the notch, the reflection generated by the 0.5-MHz shear waves is much stronger than that for the 1-MHz longitudinal waves. The loss of signal for the longitudinal waves is the result of mode conversion at the notch. These results, although limited, suggest that angle beam testing at 0.5 MHz may be the choice for inspecting isotropic CCSS with grain sizes in the range of 1-2 mm. The sensitivity for these lower frequency shear waves is, of course, lower because of the long wavelengths; therefore, only relatively large flaws will be detectable. Note that the polarization of the shear wave can be varied by rotating the transducer. As one might expect for isotropic CCSS, varying the polarization had relatively little effect on reflected echoes.

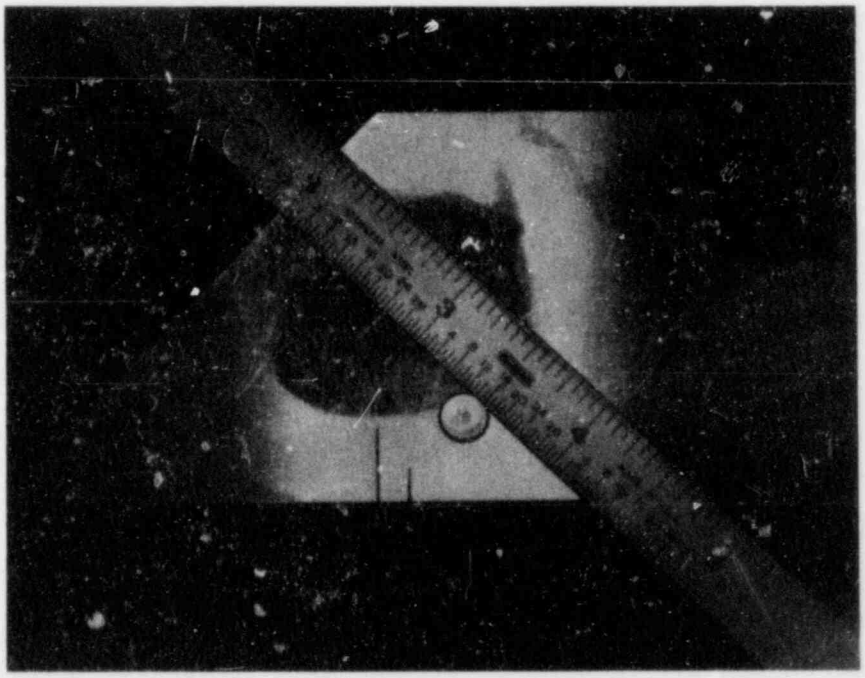

Fig. 10. Photograph of Isotropic CCSS Sample (Grain Diameter of 1-2 mm) Containing EDM Notch and 6-mm-diam Side-drilled Hole.

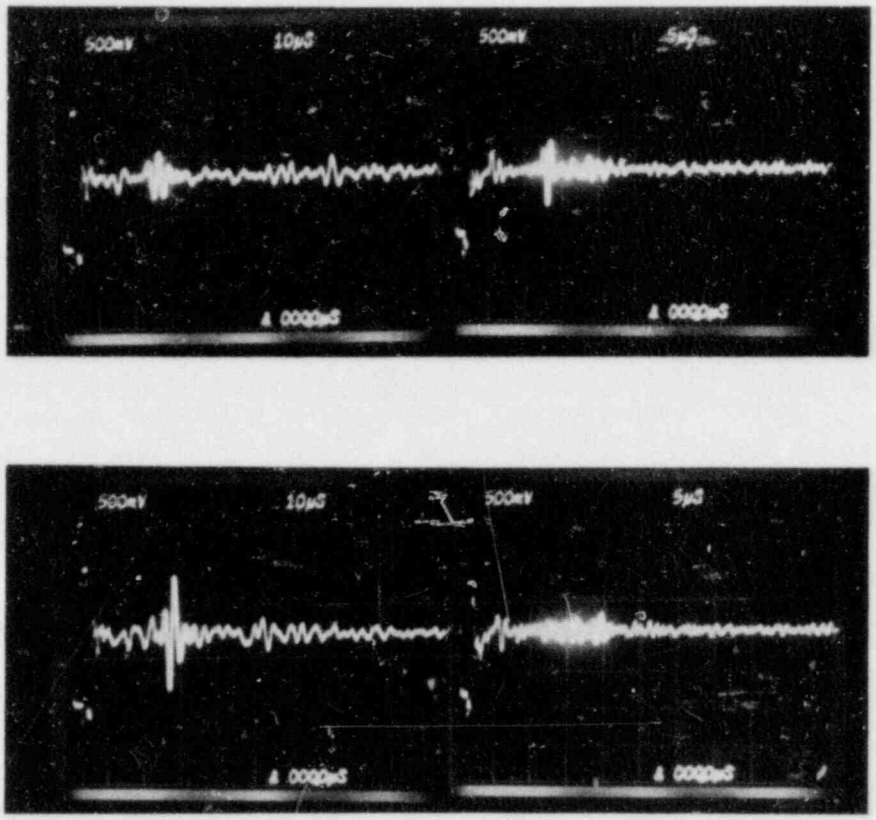

Fig. 11. Radio Frequency Echo Signals from Isotropic CCSS Sample of Fig. 10. Signals from (top) side-drilled hole and (bottom) EDM notch were obtained with (left) 0.5-MHz shear waves and (right) 1.0-MHz longitudinal waves. Transducers were placed on the sloping side of the sample to simulate 45°-angle beams.

The effect of lowering the frequency of the shear waves from 1 to 0.5 MHz can be seen in Fig. 12. Here, 45° shear waves were generated with Panametrics 1-in.-diam transducers on plastic wedges. For a 25-mm-thick wrought plate, comparable signals were obtained from the corner at both frequencies with a 1V acoustic path (top). For the isotropic half of a piece of 27-in.(0.7-m)-diam welded pipe (60 mm thick), insonified along a 1/2V path, a signal was observed at 0.5 MHz (bottom left), whereas none was seen at 1 MHz (bottom right). No signals were seen when the anisotropic half of the specimen was interrogated.

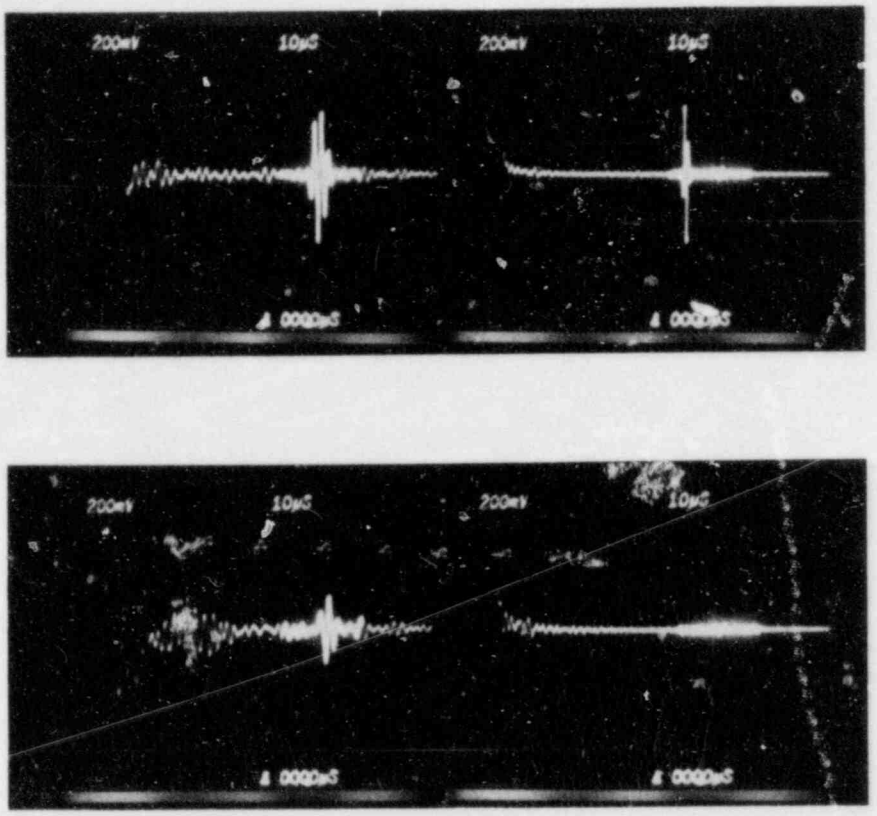

Fig. 12. Radio Frequency Echo Signals from Corner Reflectors in (Top) a 25-mm-thick Plate of Small-grained Wrought SS, Insonified along 1V Path, and (Bottom) a 27-in.-diam. Pipe Section of Isotropic CCSS, Insonified along 1/2V Path. Signals were obtained with (left) 0.5-MHz and (right) 1.0-MHz shear waves.

The present results show that the attenuation of ultrasonic waves is not necessarily lower in isotropic CCSS than in anisotropic CCSS; this is because anisotropic material provides a "window" of low attenuation for longitudinal waves propagating at about 45^{o} to the columnar grains, whereas isotropic material does not. If isotropic CCSS (with grains of the order of 1-2 mm) is to be inspected, the results of this study suggest that 0.5-MHz shear waves would provide the best combination of penetration and sensitivity for manual-type inspection; they would give a high ratio (3-6) of wavelength to grain size, and would produce minimal mode conversion problems compared with longitudinal waves. For anisotropic material, 1-MHz longitudinal waves appear to be optimum.

(2) Intergranular Stress Corrosion Cracking

Efforts are continuing on the fabrication of a probe that will rapidly distinguish IGSCC from geometrical reflectors by providing data on skew angle vs amplitude. Magnaflux Corporation is under contract to produce the multielement probe designed at ANL. Two more curves of amplitude vs skew angle (Fig. 13) have been generated from graphite-wool-grown IGSCC specimens in a 12-in. pipe section (sample M3) supplied by the EPRI Nondestructive Evaluation Center. These curves were generated by hand with a 2.25-MHz, 1/4-in., 45° shear beam. The curves are similar to those reported earlier.[3] All IGSCC specimens examined to date, including the present two, have had FW3/4M values of >50°; all geometrical reflectors examined to date have had FW3/4M values of <40°.

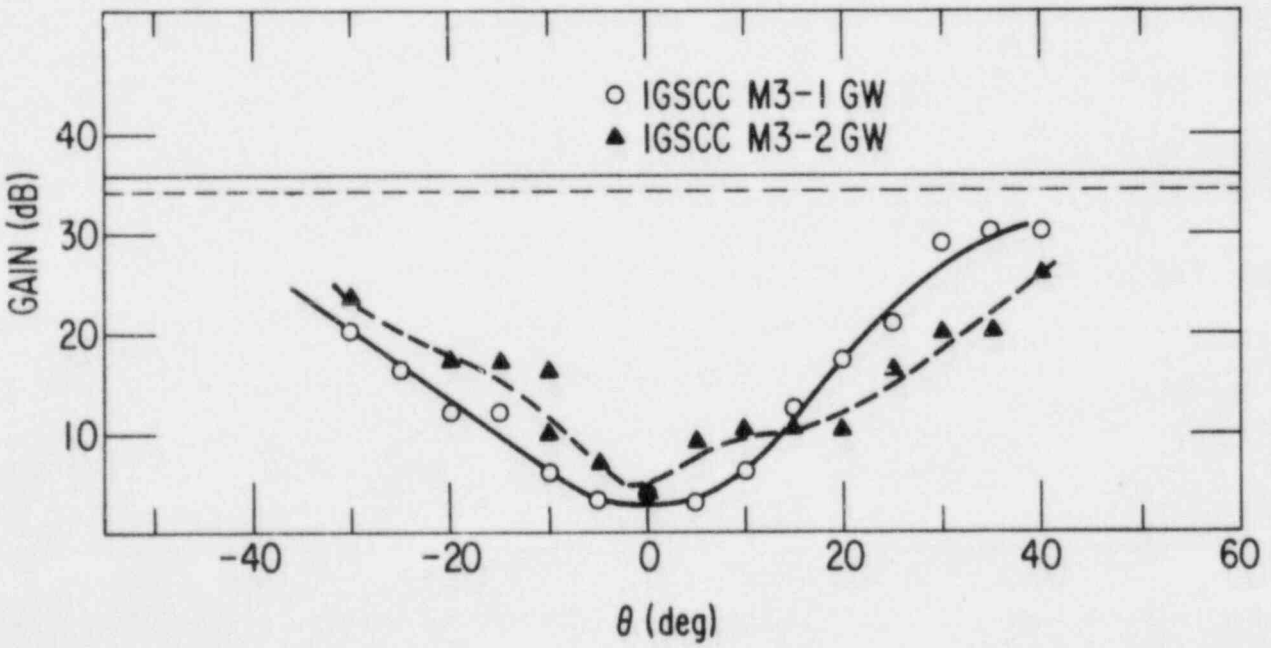

Fig. 13. Amplitude vs Skew Angle for Two Graphite-Wool-Grown IGSCC Specimens in 12-in.-diam Pipe Section M3 (Supplied by EPRI Nondestructive Evaluation Center).

B. Analysis of Sensitization (J. Y. Park)

1. Introduction

The microstructural changes resulting from thermal exposure, which produce susceptibility to intergranular corrosion, are collectively known as sensitization. It is one of the major causative factors in the IGSCC of austenitic stainless steels in LWR environments. Under normal isothermal heat treatments, sensitization of austenitic stainless steels such as Types 304 and 316 occurs in the temperature range of about 500 to 850°C. However, Type 304 SS may be sensitized at temperatures below this range if carbide nuclei are present at grain boundaries. This low-temperature sensitization (LTS) phenomenon in Type 304 SS has been demonstrated in laboratory experiments in the temperature range from 350 to 500°C. Extrapolations of this behavior to plant operating temperatures (288°C) yield estimated times ranging from 10 to 1000 years for significant LTS to occur. These wide variations have been attributed to differences in the amounts of strain, dislocation densities, and/or impurity element contents of the materials, but with the current level of understanding, the susceptibility to LTS of arbitrary heats of material cannot be assessed.

It is also not clear that the susceptibility to IGSCC produced by long, relatively low-temperature thermal aging can be adequately assessed by conventional measures of the degree of sensitization (DOS), such as the electrochemical potentiokinetic reactivation (EPR) technique or ASTM A262 Practices A through E. These tests have been developed and qualified primarily on the basis of the IGSCC susceptibility produced by high-temperature furnace sensitization or welding.

The objectives of this subtask are to establish the importance of LTS of materials under long-term reactor operating conditions, and to evaluate the effect of thermomechanical history on the correlation of IGSCC susceptibility with tests such as the EPR technique and ASTM A262 Practices A through E.

2. Technical Progress

Additional EPR measurements have been performed on Type 304 SS (Heat Nos. 10285, 30956, and 53319) specimens that were furnace heat treated at 450-750°C for 0.17-1000 h, in order to examine general high-temperature sensitization behavior. Time-temperature-EPR curves were constructed from the EPR measurements for a range of 600-700°C and 2-40 C/cm^2 (Fig. 14). The increase in EPR value due to aging is fastest for Heat No. 10285. Although the carbon concentration is the same (0.06%) for the three heats, the concentrations of the other alloy elements vary. Cihal[4] has proposed a model for the effect of such variations on relative resistance to intergranular corrosion, in which the relative resistance K is calculated from the effective chromium and carbon concentrations as follows:

$$Cr(\%)_{eff} = Cr(\%) + 1.7\ Mo(\%) \quad (4)$$

$$C(\%)_{eff} = C(\%) + 0.002[Ni(\%) - 7.9] \quad (5)$$

$$K = Cr(\%)_{eff} - 100\ C(\%)_{eff} \quad (6)$$

The K values calculated for Heats 10285, 30956, and 53319 are 12.9, 13.7, and 12.4, respectively. The ranking of the relative resistance to intergranular corrosion is consistent with the EPR measurements. However, one cannot state conclusively that the minor differences in Cr, Ni, and Mo concentration account for all of the observed heat-to-heat variations in sensitization behavior. Faster LTS kinetics have been reported for mill-annealed Type 304 SS compared to solution-treated material, and the role of grain-boundary impurity segregation and other metallurgical features has been discussed previously.[5,6]

Construction of two CERT test facilities has been completed. The test facilities can perform simple-tension or cyclic-loading CERT tests, and specimens are electrically isolated to permit better control of electrochemical tests and use of the electric potential drop method for in-situ crack length measurements. Preliminary CERT tests were performed for Type 304 SS (furnace heat-treated Heat No. 10285 and a weldment of Heat No. 53319) in high-purity water with 8 ppm oxygen at nominal strain rates of 5×10^{-7} and 2×10^{-6} s^{-1}, in order to examine

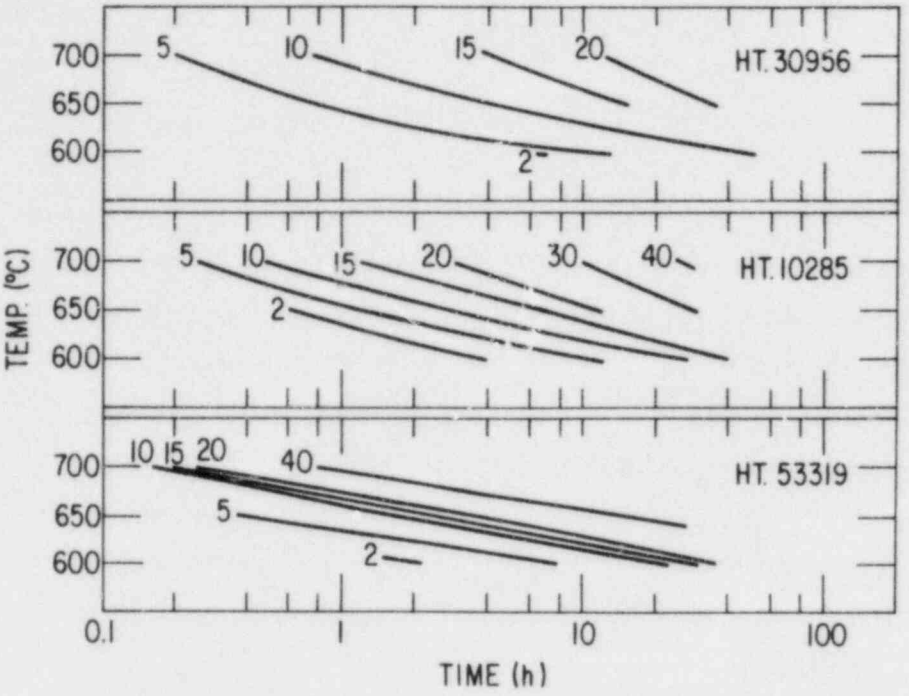

Fig. 14. Time-Temperature-EPR Curves for Type 304 SS.

the correlation between DOS (EPR) and IGSCC susceptibility. The results are summarized in Table III. Specimen 1 from Heat No. 10285, which was furnace heat treated (700°C/10 min + 500°C/24 h, EPR = 1 C/cm^2) and tested at 2×10^{-6} s^{-1}, did not show IGSCC (Fig. 15a). This is consistent with the proposed threshold EPR value (2 C/cm^2) for IGSCC.[7] However, specimen 2 from the same heat, which was furnace heat treated (700°C/10 min plus 450°C/257 h, EPR = 1 C/cm^2) and tested at 5×10^{-7} s^{-1}, failed in a predominantly transgranular mode with a minor extent of intergranular separation (Fig. 15b). This result suggests that the threshold EPR value may depend on strain rate, or that the current EPR method may underestimate sensitization produced by low-temperature aging. Further investigation of these possibilities is needed. Specimens 3 and 4, heat treated at higher temperatures (600-700°C), achieved higher EPR values (10-12 C/cm^2) and showed IGSCC. Weld specimen 5 from Heat No. 53319 (Fig. 15c) showed IGSCC failure at a uniform elongation of 19%, and a postweld heat treatment of 500°C/24 h (Specimen 6, Fig. 15d) further increased the IGSCC susceptibility, with failure observed at a uniform elongation of 12%.

TABLE III. CERT Test Results for Type 304 SS in High-Purity Water with 8 ppm Oxygen at 289°C

Specimen	Heat No.	Heat Treatment	EPR, C/cm^2	Uniform Elong., %	Strain Rate, s^{-1}	Failure Mode[a]
1	10285	700°C/10 min + 500°C/24 h	1	32	2×10^{-6}	T
2	10285	700°C/10 min + 450°C/257 h	1	25	5×10^{-7}	T + I
3	10285	600°C/30 h	12	10	2×10^{-6}	I
4	10285	700°C/0.5 h	10	17	2×10^{-6}	I
5	53319	Weld	-	19	2×10^{-6}	I
6	53319	Weld + 500°C/24 h	-	12	2×10^{-6}	I

[a] T = transgranular, I = intergranular.

Fabrication of 4-in.-diameter Type 304 SS (Heat No. 53319) pipe weldments with four different remedy treatments (IHSI, HSW, LPSW and CRC) was completed. The specimens were subjected to ASTM A262-A (oxalic acid etch) tests in the as-welded condition before low-temperature aging was initiated. All the weldments were sensitized in the HAZ, where ditch structures were evident (Fig. 16). These weldments may be close to the maximum level of IGSCC susceptibility that can be induced by sensitization per se; if this is the case, the effect of further LTS may not be fully revealed. An alternative heat of Type 304 SS with a moderate carbon concentration (0.05%) is being considered for this study.

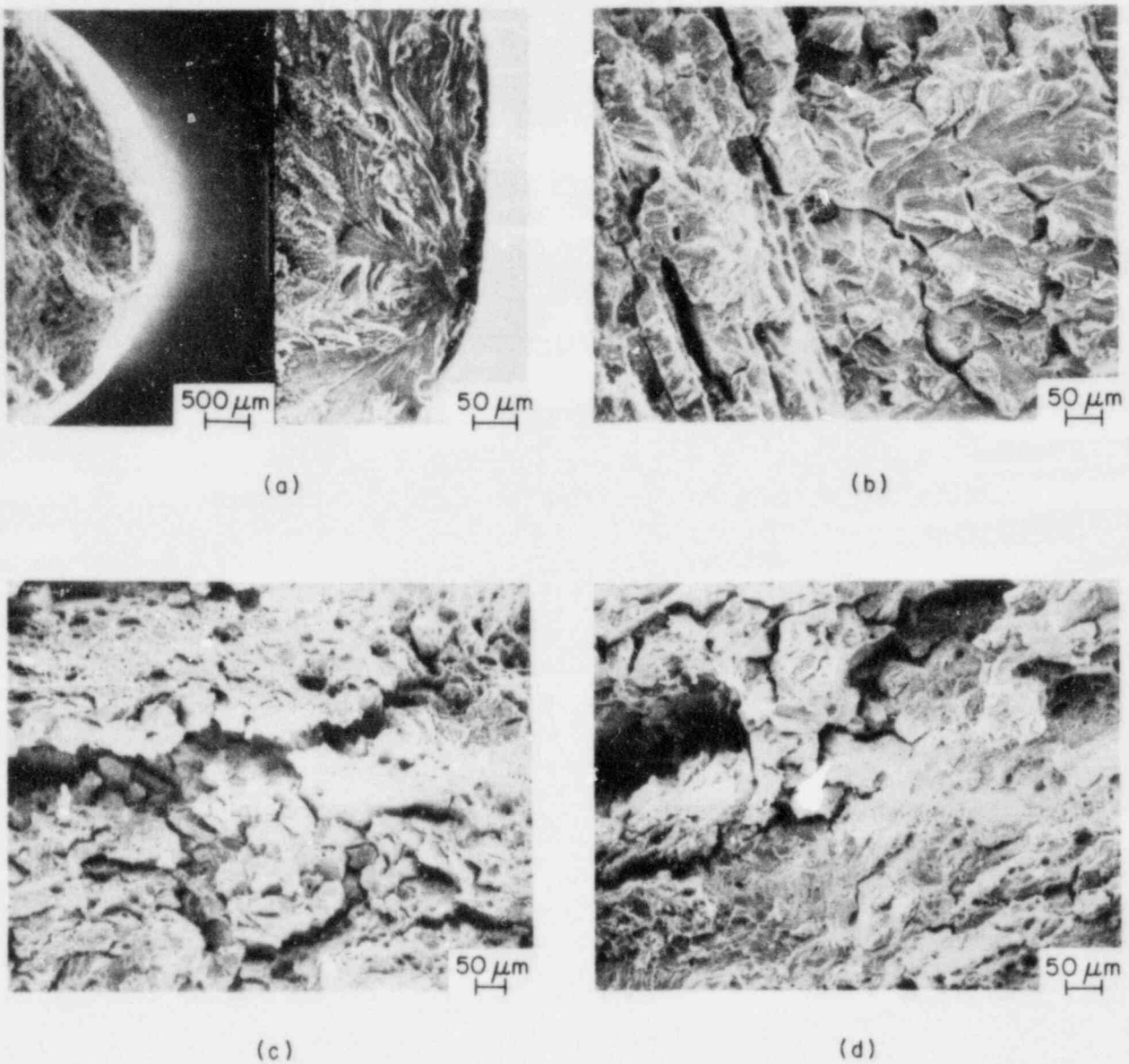

Fig. 15. Fracture Surface of Type 304 SS CERT Specimens (a) 1, (b) 2, (c) 5, and (d) 6. Heat treatments and test conditions are given in Table III.

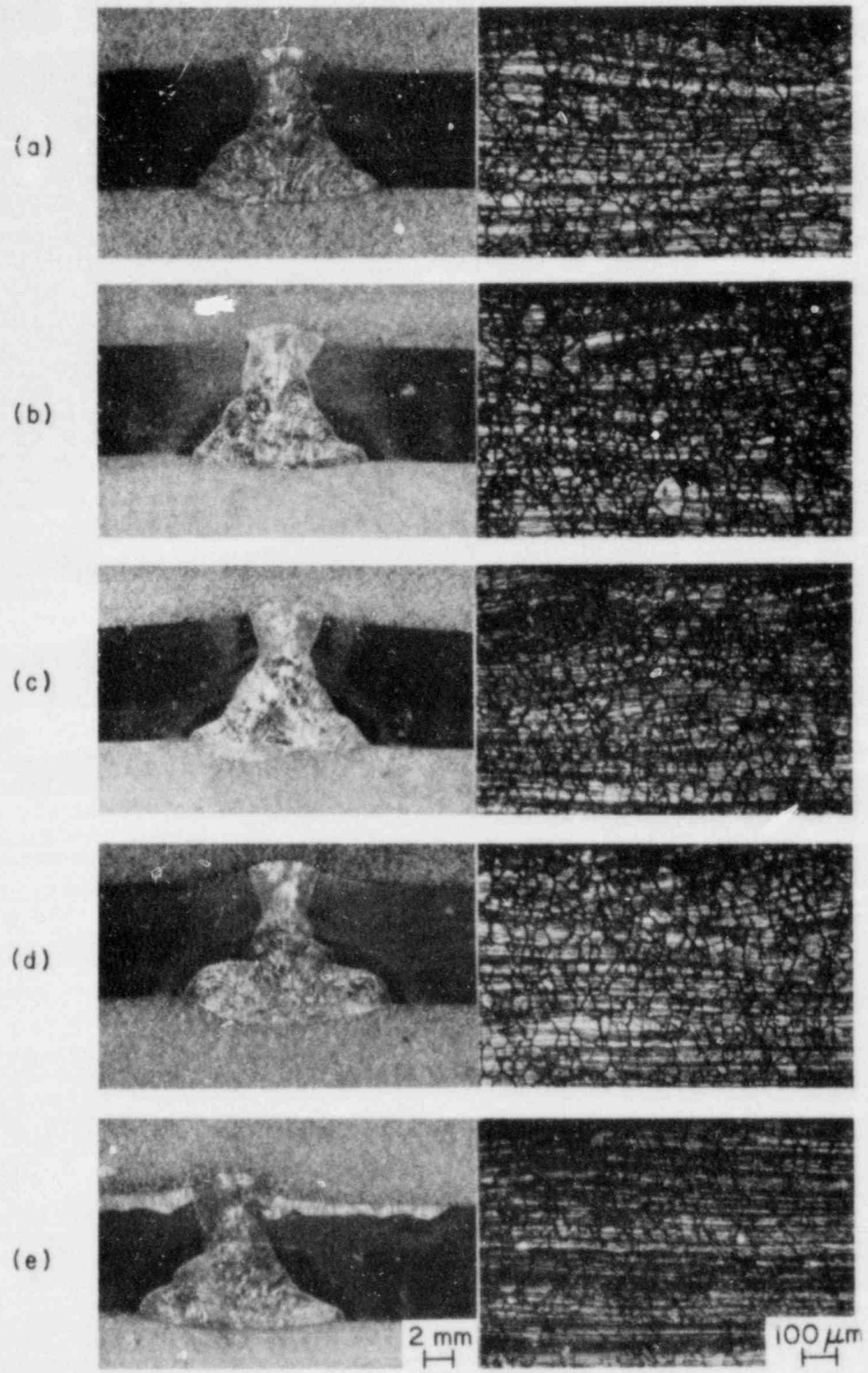

Fig. 16. ASTM A262-A Test Results for 4-in.-diam Type 304 SS Pipe Weldments: (a) Conventional Weld, (b) IHSI, (c) HSW, (d) LPHSW, and (e) CRC.

C. Crack Growth Rate Studies (J. Y. Park and W. J. Shack)

1. Introduction

The early instances of IGSCC in operating BWRs generally occurred in small pipes, and the response to the detection of IGSCC was generally to repair or replace the cracked piping immediately. It is now clear that for reactors with standard Type 304 SS piping material, cracking can occur anywhere in the recirculation system, including the main recirculation line. Because of the severe economic consequences of long forced outages for repair or replacement, the utilities will consider other approaches for dealing with cracked pipe. The possibilities include continued operation and monitoring for any subsequent growth for an indefinite period, continued operation and monitoring until a repair can be scheduled to minimize outage, and immediate repair and replacement.

Understanding crack growth behavior is, of course, important for other reasons besides assessing the safety implications of flawed piping. A better understanding would permit a more rational extrapolation of laboratory test results to the prediction of behavior in operating plants. Current work on the measurement of crack growth rates seeks to characterize these rates in terms of the linear elastic fracture mechanics (LEFM) stress intensity as well as the level of sensitization and the amount of oxygen present in the coolant. The work in this subtask is aimed at a systematic evaluation of the validity of the use of LEFM to predict IGSCC growth. The capability of data obtained under one type of loading history to predict crack growth under a different loading history will be investigated. The effect of flaw geometry on crack propagation rates will also be considered.

2. Technical Progress

Crack growth rate tests have been continued for Type 304 SS (Heat No. 10285) 1TCT specimens in water with 8 ppm oxygen at 289°C and 8.3 MPa (1200 psi). The specimens had been furnace heat treated for 700°C/10 min, with a subsequent additional treatment of 450°C/146 h, 450°C/250 h, or 500°C/24 h. The EPR values of companion test coupons were 8, 15, and

4 C/cm^2 for SPC C-09, -17, and -11, respectively. Growth rates at maximum stress intensities (K_{max}) ranging from 30 to 34 MPa·m$^{\frac{1}{2}}$, load ratios (R) of 0.5, 0.94, and 1, and frequencies (f) of 0, 2 x 10^{-3}, and 1 x 10^{-1} Hz have been reported previously.[8] The cyclic-loading tests have been performed using sawtooth waveforms with an unloading time of 5 sec. The current series of tests will establish (at a fixed K) the effect of R ratio and frequency on the growth rate, and whether these effects can be understood in terms of the crack-tip strain rate. A new set of crack growth rate tests has been carried out at R = 0.5, 0.7, 0.8 and 0.94, f = 1 x 10^{-3} and 2 x 10^{-3} Hz, and K_{max} = 30-33 MPa·m$^{\frac{1}{2}}$. The crack length was continuously monitored by the compliance method, using an in-situ clip gage. Figure 17 shows crack length vs test time for three 1TCT specimens. Interruptions or changes in the test conditions (R, f or K value) occurred at points I through XII. Average crack propagation rates were obtained by least-squares linear regression analysis for each test condition, and the results, along with those reported previously,[8] are summarized in Table IV. The calculated crack propagation rates for specimens C-09 and C-17 do not include data obtained beyond point IX, as the crack lengths for those specimens appeared to decrease at later times (Fig. 17); this suggested that the clip gages had begun to malfunction.

Ford[9] has proposed that the crack growth rate is proportional to the square root of the crack-tip strain rate, i.e.,

$$\dot{a}_{IGSCC} = A\,\dot{\varepsilon}_T^{\,n} \,. \qquad (7)$$

As discussed in Section I.D below, this relation is consistent with data obtained from CERT tests at different strain rates. Analysis of the fracture mechanics crack growth tests requires an expression for the crack-tip strain rate. Under constant applied loads, the crack-tip strain rate is determined by the time-dependent plastic deformation, i.e., creep, near the crack tip. For cyclic applied loads of sufficiently high frequency (and sufficiently low R values), the strains are imposed by the external loading mechanism. Estimates of the crack-tip strain rates in this case can be obtained from LEFM. Scott and Truswell[10] have suggested a relation of the form

TABLE IV. Crack Propagation Rates in Type 304 SS Specimens (Heat No. 10285) Sensitized to Two Different Levels and Tested in 289°C Water with 8 ppm O_2

f, Hz	R	$\dot{\varepsilon}_T$, s^{-1}(a)	K_{max}, MPa·$m^{1/2}$	ȧ, m/s
		EPR = 4 C/cm^2		
0	1	-	33-34	1.2×10^{-10}
2×10^{-3}	0.5	2.7×10^{-4}	30-33	3.4×10^{-9}
2×10^{-3}	0.8	4.1×10^{-5}	29-32	7.4×10^{-10}
2×10^{-3}	0.6	1.7×10^{-4}	32-33	6.6×10^{-10}
2×10^{-3}	0.7	9.3×10^{-5}	30-31	3.4×10^{-10}
2×10^{-3}	0.7	9.3×10^{-5}	32-33	5.9×10^{-10}
2×10^{-3}	0.5	2.7×10^{-4}	30-31	8.9×10^{-10}
1×10^{-1}	0.94	1.8×10^{-4}	30-31	3.1×10^{-10}
1×10^{-1}	0.94	1.8×10^{-4}	31-32	1.9×10^{-10}
		EPR = 15 C/cm^2		
0	1	-	32-33	2.2×10^{-10}
2×10^{-3}	0.5	2.7×10^{-4}	30-32	2.8×10^{-9}
2×10^{-3}	0.6	1.7×10^{-4}	28-29	5.6×10^{-10}
1×10^{-1}	0.94	1.8×10^{-4}	30	2.1×10^{-10}

[a] $\dot{\varepsilon}_T = -1/T \ln [1 - (1 - R)^2/2]$.

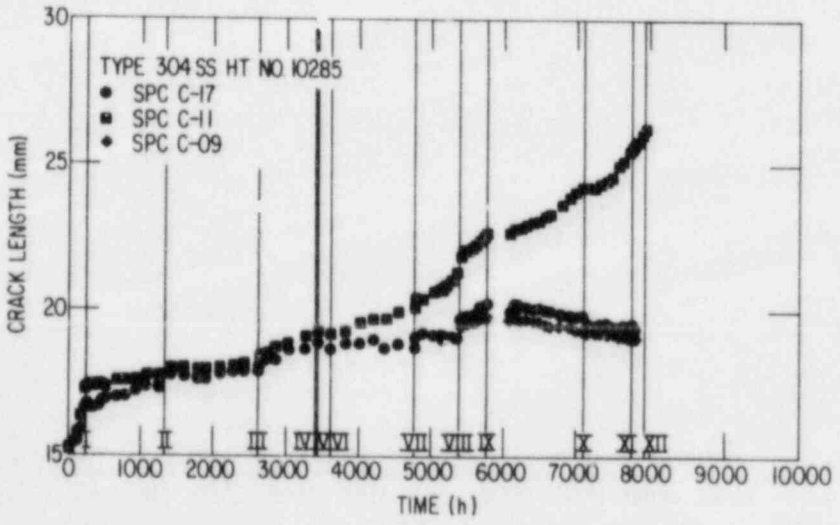

Fig. 17. Plots of Crack Length vs Time for Heat No. 10285 Specimens.

$$\dot{\epsilon}_T = - 1/T \ln [1 - (1 - R)^2/2], \quad (8)$$

where T is the rise time for the tensile portion of the load cycle. Related expressions for crack-tip strains in fatigue have been proposed by Rice[11] and others. Equation (8), since it neglects constant-load creep, predicts $\dot{\epsilon}_T = 0$ for the constant-load case. It also predicts that the crack-tip strain rate is independent of the value K and hence, together with Eq. (7), predicts that the crack growth rate is independent of K. This prediction is contradicted by many experimental observations. For a fixed K, the dependence of the crack growth rate on f observed in the tests on Heat 30956 in Subtask E (see below) is roughly consistent with Eqs. (7) and (8). However, for the tests performed on Heat 10285 where both R and f are varied, the data differ by an order of magnitude from predictions based on Eqs. (7) and (8), as shown in Fig. 18. Tests are currently in progress to explore additional R values and frequencies, and alternative formulations for the crack-tip strain rates are being explored.

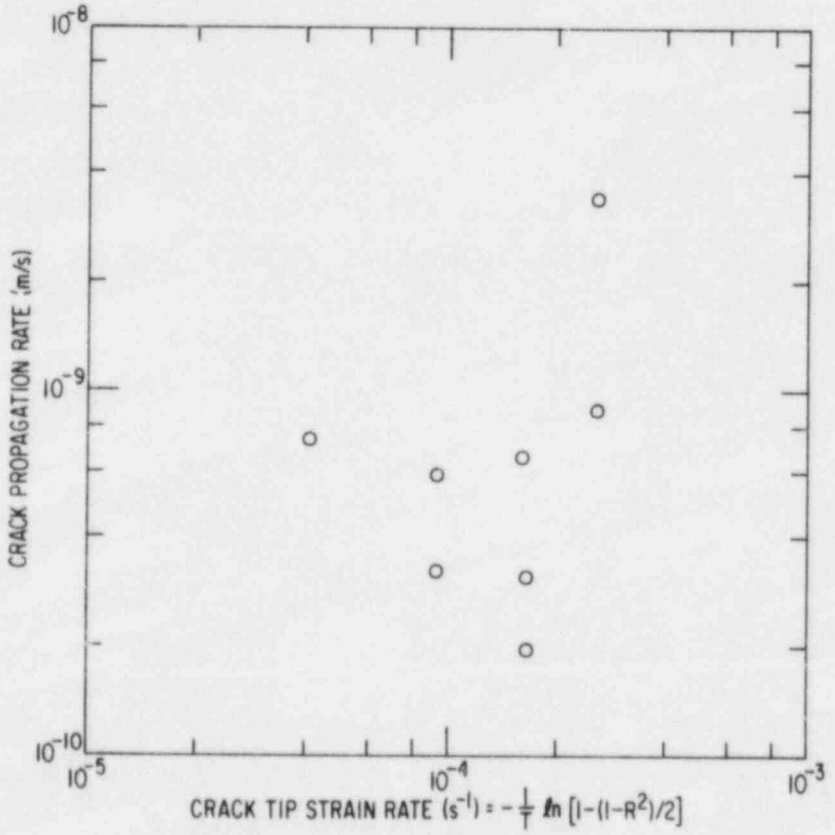

Fig. 18. Crack Propagation Rate vs Crack Tip Strain Rate for Type 304 SS (Heat No. 10285).

D. Evaluation of Nonenvironmental Corrective Actions (P. S. Maiya and W. J. Shack)

1. Introduction

The fundamental premises of the current efforts to prevent IGSCC in BWR piping are (1) that IGSCC involves a complex interaction among susceptibility of a material to damaging conditions over time (sensitization), the stresses acting on the material, and the nature of the environment, and (2) that suitable alteration or variation of these parameters can prevent IGSCC in materials of interest. Nonenvironmental corrective actions involve mitigation of either the material's susceptibility to sensitizing conditions or the state of stress on the inside surface of the weldment. Such actions include the use of fabrication or treatment techniques that improve the IGSCC resistance of susceptible materials (e.g., Type 304 SS) and the identification of alternative materials that are inherently more resistant to IGSCC.

The objective of the current work is an independent assessment of the proposed remedies developed by the utilities and the vendors. Additional testing and research will be done to eliminate gaps in the existing data base on alternative materials and fabrication methods, and to develop a better understanding of the relation between the existing laboratory results and satisfactory in-reactor operating performance. Current efforts in this task include additional screening tests for alternative materials, environmental pipe tests under alternate loading conditions, and the study of stress redistribution near weldments to determine the effect of in-service loading conditions on techniques for reducing residual stress loads.

2. Technical Progress

a. Impurity and Strain Rate Effects

CERT experiments to evaluate the relative SCC susceptibility of Types 316NG, 304, and 316 SS in oxygenated water (0.2 ppm O_2) containing

chloride or sulfate impurities are continuing. In oxygenated water (0.2 ppm O_2) with 0.2 ppm Cl^- (added as acid), 316NG/308L weldments with an additional LTS treatment (500°C/24 h) did not exhibit SCC at strain rates $\dot{\epsilon} \geq 2 \times 10^{-7}$ s^{-1}; at a strain rate of 2×10^{-7} s^{-1}, the failure strain ϵ_f is 31.9%. However, a similar test at a slower strain rate of 4×10^{-8} s^{-1} produced a lower ϵ_f of 18.3%. A cursory examination of the fractured surface by scanning electron microscopy indicated that fracture had occurred partly in the base metal and partly in the weld. The fracture of the base metal was ductile, but the weld metal showed transgranular SCC (TGSCC) in addition to some ductile regions. While these observations are consistent with the reduced ϵ_f, the TGSCC observed for this case in the weld metal is rather unexpected and needs further study. A similar test at the same strain rate ($\dot{\epsilon} = 4 \times 10^{-8}$ s^{-1}) in oxygenated water (0.2 ppm O_2) with 0.1 ppm SO_4^{2-} is currently in progress.

Studies concerning the effects of impurity environments on the cracking susceptibility of conventional Types 304 and 316 SS are also in progress. Specimens of Type 304 SS (Heat No. 53319) sensitized at 600°C/24 h (EPR = 24 C/cm^2) did not become susceptible to IGSCC in oxygenated water (0.2 ppm O_2) with 0.1 ppm Cl^- (added as acid) at $\dot{\epsilon} = 1 \times 10^{-6}$ s^{-1}. However, when the impurity level was increased to 0.2 ppm Cl^-, IGSCC occurred with an average crack velocity $\dot{a}_{av} = 4.9 \times 10^{-7}$ cm/s. IGSCC also occurred in an environment containing 0.1 ppm SO_4^{2-} (added as H_2SO_4) with $\dot{a}_{av} = 7.4 \times 10^{-7}$ cm/s. Thus, at $\dot{\epsilon} = 1 \times 10^{-6}$ s^{-1}, additions of SO_4^{2-} (as acid) to oxygenated water with 0.2 ppm O_2 are more aggressive than additions of identical concentrations of Cl^-, which give approximately the same conductivity. However, as reported earlier,[12] Cl^- is more aggressive than SO_4^{2-} in water with 8 ppm O_2. Hence, the relative aggressiveness of the impurity species depends on the oxygen content of the water.

In contrast to the results obtained in Subtask C from crack growth rate tests on fracture-mechanics-type specimens in high-purity environments, the DOS in impurity environments appears to have a significant effect on the crack growth rates in CERT tests. For example, the average intergranular crack growth rate observed for the material

sensitized at 600°C/24 h (EPR = 24 C/cm^2) is approximately twice that observed for the material sensitized at 600°C/2 h (EPR = 11 C/cm^2) at the same strain rate.

No significant difference in IGSCC susceptibility is observed when SO_4^{2-} is added as Na_2SO_4 instead of as acid. For example, a test in oxygenated water (0.2 ppm O_2) with 0.1 ppm SO_4^{2-} (added as Na_2SO_4) resulted in an average crack growth rate of 5.9×10^{-7} cm/s for sensitized Type 304 SS compared with $\dot{a}_{av} = 7.4 \times 10^{-7}$ cm/s observed in the environment containing 0.1 ppm SO_4^{2-} (added as acid). Hence the solution pH appears to be of secondary importance compared to the concentration of critical anions such as SO_4^{2-}.

Despite the widespread recognition of the importance of the imposed $\dot{\varepsilon}$ in CERT tests[13-16], the majority of studies, especially on austenitic SS/water systems, have been limited to one strain rate, typically of $\sim 1 \times 10^{-6}$ s^{-1}. A better understanding of the effect of strain rate is important in understanding IGSCC susceptibility as well as in providing a rational basis when extrapolating the laboratory results to those encountered under reactor operating conditions. An analysis of the effects of strain rate in the CERT test has been carried out and used to deduce correlations between strain rate and other quantifiable IGSCC susceptibility parameters (e.g., average crack growth rate $\dot{a}$ and time to failure t_f). Good agreement is obtained between the results of the analysis and CERT tests over a fairly wide range of strain rates; thus, the analysis represents an important step in developing a better understanding of the effect of loading history on IGSCC susceptibility.

The test results presented here were on Type 316 SS sensitized at 600°C/24 h in oxygenated water with 0.5 ppm Cl^- (added as acid) over a range of $\dot{\varepsilon}$ from 1×10^{-5} to 2×10^{-7} s^{-1} at 289°C. The description of $\dot{\varepsilon}$ effects on IGSCC susceptibility is equally applicable to impurity-free environments and is expected to be valid for the range of water chemistries encompassed by the Nuclear Regulatory Guide 1.56 limits. As discussed previously,[17] IGSCC was observed for the material in the chloride environment at all strain rates used in the experiments. The estimated $\dot{a}_{av}$ was

found to decrease with a decrease in strain rate $\dot{\varepsilon}$ from 1×10^{-5} to 2×10^{-7} s^{-1}. The results also suggested that the extent of cracking increased with a decrease in $\dot{\varepsilon}$. Specifically, a least-squares fit of the data to the relation $a_f = At_f^n$ (where a_f is the maximum crack length at failure) yielded an exponent $n = \frac{1}{2}$ (see Fig. 19) and thus a_f and t_f for tests at different strain rate are related by

$$a_f = At_f^{\frac{1}{2}} \tag{9}$$

where A is a constant, assumed to be a function of the microstructural state of the material (for example, DOS) and the environment but independent of $\dot{\varepsilon}$. Equation (9) is also found to be consistent with the relation between $\dot{a}_{av}$ and the average crack-tip strain rate $\dot{\varepsilon}_T$, which is obtained[12] from

$$\dot{\varepsilon}_T = \frac{1}{t_f - t_o} \ln \frac{\varepsilon_f}{\varepsilon_o} + \ln \frac{a_f}{a_o} \tag{10}$$

where t_o, ε_o and a_o are the time, strain, and crack length at the initiation of the crack. For Type 316 SS in the chloride environment, $\dot{a}_{av}$ and $\dot{\varepsilon}_T$ are related by[12]

$$\dot{a}_{av} = A_T(\dot{\varepsilon}_T)^{0.5} \tag{11}$$

(where A_T is a constant) for the initiation parameter $a_o = 1$ μm and $\varepsilon_o = 0.3\%$; the crack-tip strain rate exponent is shown to be fairly insensitive to the choice of initiation parameters.[12] Equation (11) is also consistent with a model proposed by Ford[9,18] which assumes that the current decay after film rupture follows parabolic kinetics. His assumption is based on measurements of anodic current decay transients at freshly created metal surfaces in passive steels in dilute solutions, which often show a $t^{\frac{1}{2}}$ decay law. Such a law has been tentatively interpreted as suggesting that the rate-controlling process step in the dissolution-repassivation is the diffusion of aqueous ions away from the crack tip. Rewriting Eq. (11) in incremental form in terms of the current crack propagation rate and crack-tip strain rate rather than average values, we obtain

$$\dot{a} = A_T \left(\frac{\dot{a}}{a} + \frac{\dot{\varepsilon}}{\varepsilon} \right)^{0.5} \tag{12}$$

where a and $\dot{a}$ are the crack length and velocity at time t. Equation (12) is based on the definition of crack-tip strain rate in terms of the crack-tip opening displacement and displacement rate and on the use of a J-integral approach similar to that used, for example, by Mowbray.[19] For CERT tests, $\dot{\varepsilon}/\varepsilon = 1/t$ and therefore

$$\dot{a} = A_T \left(\frac{\dot{a}}{a} + \frac{1}{t} \right)^{0.5}; \tag{13}$$

thus, $\dot{a}$ is independent of $\dot{\varepsilon}$ and depends only on time. The exact analytical solution of Eq. (13) is

$$a = A_T \sqrt{6t}, \tag{14}$$

which is consistent with a diffusion-controlled crack propagation process; defining $a = a_f$ and $t = t_f$ at failure, we obtain

$$a_f = A_T \sqrt{6t_f}. \tag{15}$$

Equation (15) is identical to Eq. (9) with $A = \sqrt{6}\, A_T$. Equation (9) is a useful relation but is not sufficient to predict t_f; in addition to a description of crack growth, a final fracture criterion is required. A possible fracture criterion is based on a J-integral approach,

$$J = C_o \varepsilon^{n+1} f(n) a \tag{16a}$$

$$\simeq C \varepsilon^{n+1} a \tag{16b}$$

where C_o = material parameter, n = strain-hardening exponent, f(n) = function of n, $C \simeq C_o f(n)$, and failure occurs when $J = J_C$; J_C is a constant which depends on the material, geometry, and possibly the environment, but

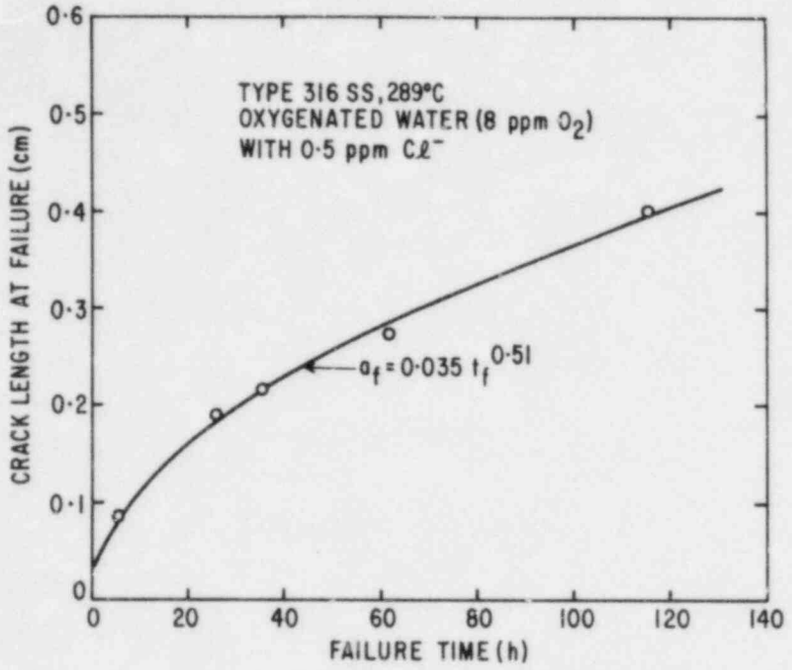

Fig. 19. Variation of Crack Length at Failure (a_f) with Time to Failure (t_f) in Tests Conducted at Different Strain Rates.

which is assumed to be independent of strain rate. (For a more detailed discussion of the significance of J, see, for example, Ref. 19). The validity of the fracture criterion represented by Eq. (16b) is illustrated by a log-log plot of a_f vs ε_f (Fig. 20), which, within the limits of experimental scatter, yields a straight line. From the slope of this line, the value of n is found to be about 0.16, which is not an unreasonable value for an austenitic SS at the strains of interest. Since n is fairly small, Eq. (16b) can be simplified to

$$J_C = C\varepsilon_f a_f \ . \tag{17}$$

Equations (9) and (17) can be combined to derive the following correlations between the IGSCC susceptibility parameters and the strain rate:

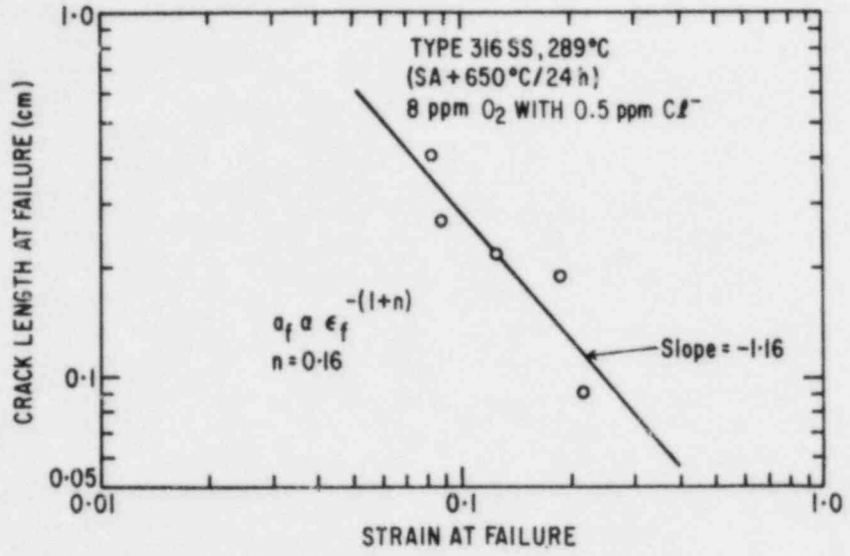

Fig. 20. Log-Log Plot of Crack Length at Failure (a_f) Versus Strain at Failure (ϵ_f).

$$\dot{a}_{av} = A(AC/J_c)^{1/3}\dot{\epsilon}^{1/3}, \tag{18}$$

$$t_f = (J_c/AC)^{2/3}\dot{\epsilon}^{-2/3}, \tag{19}$$

$$\epsilon_f = (J_c/AC)^{2/3}\dot{\epsilon}^{1/3}, \tag{20}$$

and

$$a_f = A(J_c/AC)^{1/3}\dot{\epsilon}^{-1/3}. \tag{21}$$

The above correlations are observed to be in good agreement with the experimental data. For example, log-log plots of $\dot{a}_{av}$, t_f, ϵ_f, and a_f vs $\dot{\epsilon}$ yield straight lines with slopes that are in good agreement with the predicted strain rate exponents, as shown in Figs. 21-24. These values are also consistent with the limited experimental results reported in the literature.[15,20] For example, Ford[20] has observed the relationship $\dot{a}_{av} \propto \dot{\epsilon}^{0.35}$ for Type 304 SS in high- purity water containing 0.2 ppm O_2 and in water with 0.01M Na_2SO_4 at a temperature of ~100°C. Also, from the published[15] strain rate effects on uniform elongation for Type 304 SS (sensitized at

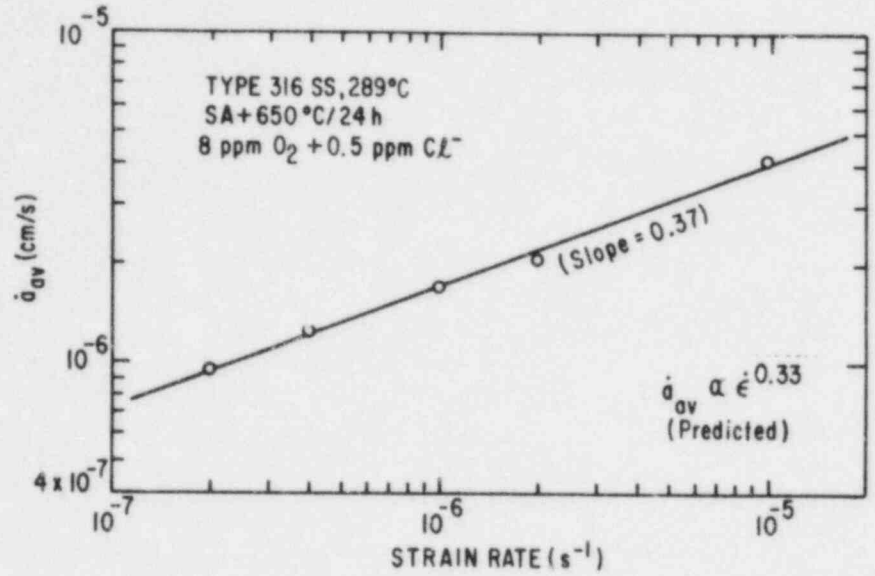

Fig. 21. Log-Log Plot of Average Intergranular Crack Growth Rate ($\dot{a}_{av}$) Versus Strain Rate ($\dot{\epsilon}$).

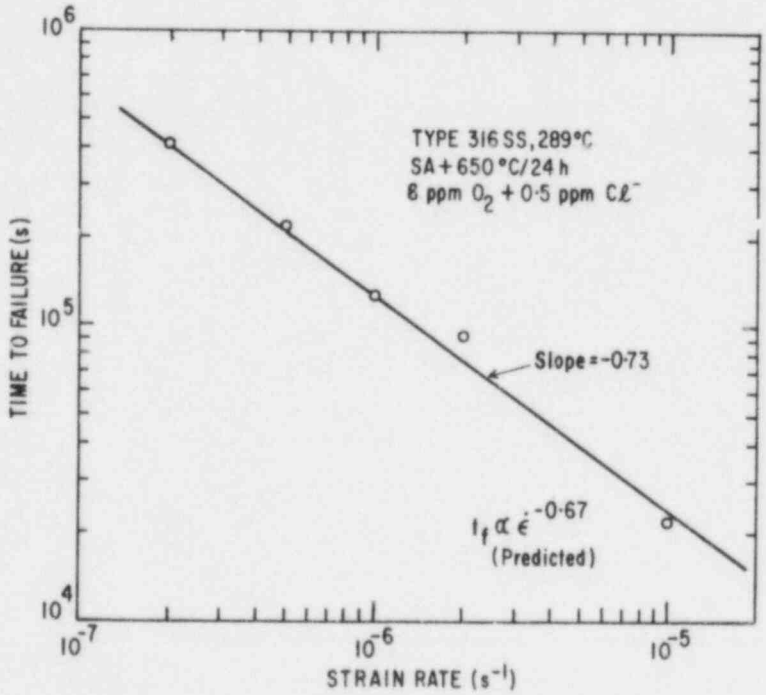

Fig. 22. Log-Log Plot of Time to Failure (t_f) Versus Strain Rate ($\dot{\epsilon}$).

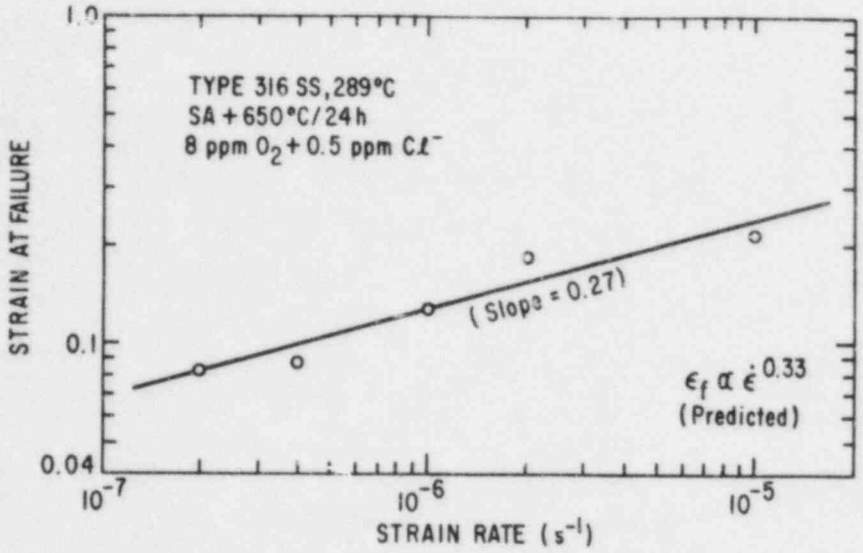

Fig. 23. Log-Log Plot of Strain at Failure (ε_f) Versus Strain Rate ($\dot{\varepsilon}$).

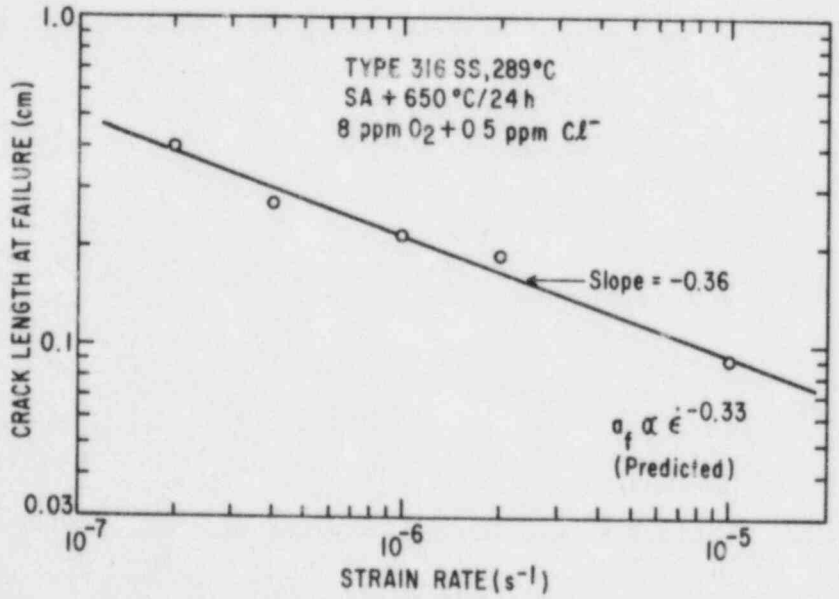

Fig. 24. Log-Log Plot of Crack Length at Failure (a_f) Versus Strain Rate ($\dot{\varepsilon}$).

600°C/24 h) tested in oxygenated water (8 ppm O_2) at 290°C, it can be shown that uniform strain is proportional to $\dot{\varepsilon}^{0.37}$. The potential usefulness of Eqs. (18)-(21) can be demonstrated by using one or two sets of CERT results obtained at higher strain rates to predict the IGSCC susceptibility without resorting to a back-fit of the data. As can be seen in Table V, the IGSCC susceptibility at strain rates of 1×10^{-6}, 4×10^{-7} and 2×10^{-7} s^{-1} can be realistically predicted from the experimental data obtained at higher strain rates (1×10^{-5} and 2×10^{-6} s^{-1}) and the agreement between the predicted and experimental values is very satisfactory. These results are important, considering that the strain rates encountered in a reactor are generally slower than normally used in the laboratory and experiments at slower strain rates are time-consuming and are often limited by experimental capabilities.

b. Stress/Strain/Strain-Rate Relations for Sensitized Materials

Stress relaxation experiments are being performed to determine the stress/strain/strain-rate relations of Types 316 and 304 SS for different material conditions (e.g., sensitized, solution-annealed, pre-strained). These constitutive relations are required to determine the strain rates associated with different loading histories. As discussed above, strain rate is one of the major parameters affecting IGSCC. The existing experimental facility permits stress/strain/strain-rate measurements at 28°C over a wide range of $\dot{\varepsilon}$ from $\sim 10^{-4}$ to 10^{-10} s^{-1}; plans are currently being made to modify the system to permit measurements at temperatures of up to 300°C. Analysis of data and the form of constitutive relations remain the same over the temperature range from 28 to 300°C. As discussed earlier,[12] the state variable approach of Hart[21] and a slightly modified version of the constitutive equations proposed by Miller and Tanaka[22] were used to analyze the data obtained with initial stresses of 1.1 σ_y to 1.5 σ_y (where σ_y = 255 MPa) for sensitized Type 316 SS at 28°C. Both sets of constitutive relations described the stress relaxation data fairly well, but the state variable approach gave better agreement. One of the significant differences between the two approaches lies in the choice of structure parameter; the state variable approach uses the hardness parameter

TABLE V. Comparison of Predicted and Experimental CERT Properties for Type 316 SS in Oxygenated Water (8 ppm O_2) with 0.5 ppm Cl^-

IGSCC Susceptibility Parameter	Strain Rate, s^{-1}					
	1×10^{-6}		4×10^{-7}		2×10^{-7}	
	Pr[a]	Exp	Pr[a]	Exp	Pr[a]	Exp
a_f, cm	0.22	0.22	0.30	0.27	0.38	0.40
ε_f, %	13.4	12.9	9.9	8.8	7.8	8.3
$\dot{a}_{av}$, cm/s	1.66×10^{-6}	1.68×10^{-6}	1.21×10^{-6}	1.24×10^{-6}	9.72×10^{-7}	9.98×10^{-7}
t_f, h	37.2	35.7	68.4	61.4	108.7	115.5

[a]Predictions based on experimental data at two higher strain rates (2×10^{-6} and 1×10^{-5} s^{-1}).

σ^* and the creep law of Miller uses the non-elastic strain ε_n as the structure variable. This is simply illustrated as follows: Miller's method (based on a creep law) predicts the non-elastic strain rate $\dot{\varepsilon}_n$ as a function of temperature T, applied stress σ, and the current level of non-elastic strain itself, i.e.,

$$\dot{\varepsilon}_n = f(T)g(\sigma, \varepsilon_n). \tag{22}$$

On the other hand, the state variable approach describes

$$\dot{\varepsilon}_n = h(\sigma, \sigma^*, \dot{a}^*) \tag{23}$$

where $\dot{a}^*$ is the friction rate parameter, which is temperature dependent. In Eqs. (22) and (23), g and h are functions of the indicated variables. Although σ^* is, conceptually, a better parameter for describing the loading-history effects than ε_n, it is not always easy to determine σ^* in practical situations. Furthermore, the literature contains more extensive discussion concerning the application of Miller's equation to determine $\dot{\varepsilon}$ from loading histories of interest to BWR applications. Therefore, we propose to rewrite Hart's equation in a form that contains the essential ingredients of Miller's creep law in the following manner. Equation (23) can be rewritten as

$$\dot{\varepsilon}_n = h(\sigma, \varepsilon_n, \dot{a}^*) \tag{24}$$

where σ^* has been replaced by ε_n. If the temperature dependence is contained in $\dot{a}^*$ (for example, $\dot{a}^* = \dot{a}_o^* \exp(-\Delta H/RT)$ where ΔH is an activation energy whose physical significance remains to be identified), the constitutive Eq. (24) in essence contains the ingredients of Miller's equation. Specifically, using the data obtained for Type 316 stainless steel at 28°C, we have shown that the constitutive equation

$$\dot{\varepsilon} = \dot{a}^* \left(\frac{\sigma - \sigma^*}{G}\right)^M \tag{25}$$

describes the data fairly well. Using the data previously discussed, it is observed that σ^* and ϵ_n are related by a power law,

$$\sigma^* = B(\epsilon_n)^{\beta}, \tag{26}$$

as shown in Fig. 25 with B = 714 MPa and β = 0.3. Thus, Eq. (25) becomes

$$\dot{\epsilon} = \dot{a}^* (T) \left[\frac{\sigma - B(\epsilon_n)^{\beta}}{G}\right]^M, \tag{27}$$

in which M is shown to be equal to 14. If the strain rate effects on work hardening can be ignored at temperatures ranging from 28 to 300°C, Eq. (27) [which is interchangeable with Eq. (25)] represents a useful constitutive equation for investigating the effects of loading history on IGSCC.

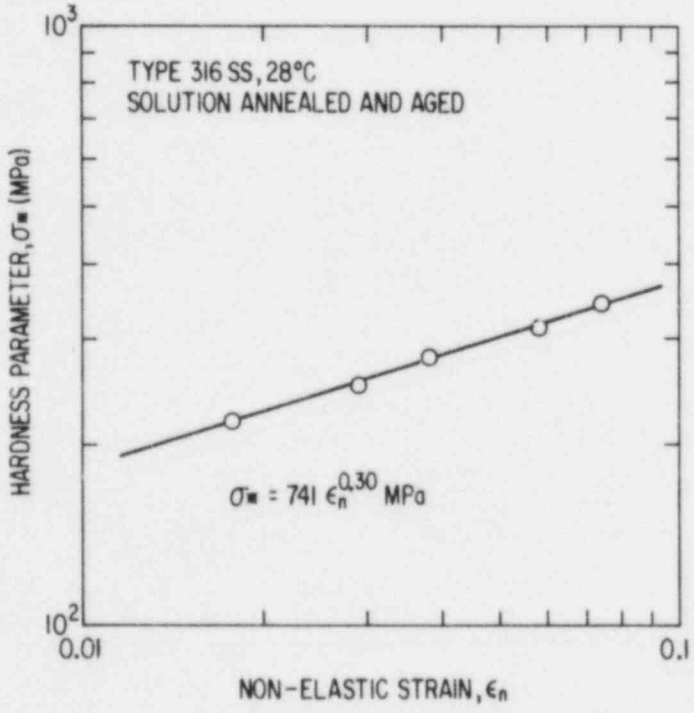

Fig. 25. Relationship between Hardness Parameter (σ^*) and Non-elastic Strain (ϵ_n).

E. Evaluation of Environmental Corrective Actions (W. E. Ruther, W. K. Soppet, and T. F. Kassner)

1. Introduction

The objective of this subtask is to evaluate the potential effectiveness of proposed actions to solve or mitigate the problem of IGSCC in BWR piping and safe ends through modifications of the water chemistry. Although the reactor coolant environment has a profound influence on the performance and reliability of nuclear power-plant components, the synergistic effects of oxygen (produced by radiolytic decomposition of the water) and impurities (e.g., H_2SO_4 from decomposition of ion exchange resins during periodic intrusions into the primary system) on the IGSCC susceptibility and cyclic crack growth properties of sensitized Type 304 SS have not been investigated adequately. Also, it is not clear whether the potential benefits associated with small additions of hydrogen to the coolant can be realized in the presence of impurities within the normal operating limits on pH (5.6 to 8.6 at 25°C) and specific conductance ($\leq$1.0 μS/cm at 25°C) of the reactor coolant water.

During this reporting period, additional results have been obtained from CERT tests on a reference heat of Type 304 SS, with two levels of sensitization, in 289°C water containing 0.5 and 2 ppm dissolved hydrogen, 0.03 to 0.2 ppm oxygen, and 0 to 10.0 ppm sulfate (as H_2SO_4). The extent to which the SCC susceptibility is reflected in the cyclic crack growth behavior of the steel under low-frequency, moderate-stress-intensity, and high-R loading is also being evaluated in high-purity water with 8 ppm oxygen, and in water containing 0.1 ppm sulfate and 0.2 ppm oxygen at 289°C.

2. Technical Progress

a. Results of CERT Experiments on Sensitized Type 304 SS

Additional information has been obtained from CERT experiments on the effect of dissolved oxygen, hydrogen, and sulfate (as H_2SO_4) on the SCC susceptibility of sensitized Type 304 SS in 289°C water. The specimens were sensitized to EPR values of 2 and 20 C/cm^2 during heat treatments at 700°C for

0.25 h plus 500°C for 24 h and 700°C for 12 h, respectively. Most of the results, which were not reported previously, were obtained in water containing 10 ppm sulfate (as H_2SO_4) and 0.03 and 0.2 ppm dissolved oxygen with 0.5 ppm hydrogen, and 0.02 ppm oxygen with 2.0 ppm hydrogen.

Results of CERT experiments on the steel with both levels of sensitization in high-purity water at 289°C and a strain rate of 1×10^{-6} s^{-1} are summarized in Table VI. As the dissolved oxygen concentration decreased to $\lesssim$0.1 ppm, a transition in the fracture mode from ductile-plus-intergranular to ductile-plus-transgranular occurred for the moderately sensitized material (EPR = 20 C/cm^2). The transition occurred in the lightly sensitized steel (EPR = 2 C/cm^2) at a somewhat higher oxygen concentration ($\sim$0.3 ppm).

Results from the series of CERT experiments on the reference heat of Type 304 SS in 289°C water containing 0.03 to 8.6 ppm oxygen and 0.01 to 10 ppm sulfate as H_2SO_4 are given in Table VII. The influence of sulfate concentration on the time to failure and maximum stress for lightly (EPR = 2 C/cm^2) and moderately (EPR = 20 C/cm^2) sensitized steel in water containing $\sim$0.03, 0.2, and 8 ppm dissolved oxygen is shown in Figs. 26 and 27, respectively. Even at the lowest dissolved oxygen concentrations (viz., 0.03 ppm), the fracture mode was primarily intergranular for sulfate concentrations $\gtrsim$0.1 ppm. For an oxygen concentration of $\sim$0.2 ppm, the time to failure increased as the sulfate concentration decreased for both levels of sensitization of the material. This also occurred in the lightly sensitized material at a higher oxygen concentration (viz., 8 ppm); however, the CERT parameters of the moderately sensitized steel were not dependent on sulfate concentrations in oxygenated water (Fig. 27).

The results in Table VIII and Figs. 28 and 29 confirm our preliminary conclusion[23] that $\sim$0.5 ppm of dissolved hydrogen per se in the feedwater has only a small beneficial effect on the CERT parameters (viz., the time to failure and total elongation) at low dissolved oxygen concentrations ($\lesssim$0.03 ppm) and almost no effect at an oxygen concentration of $\sim$0.2 ppm for sulfate concentrations between $\sim$0.01 and 1 ppm. The effect of increasing the dissolved hydrogen concentration to 2 ppm on the SCC susceptibility of the steel in 289°C water with 0.03 ppm oxygen and 1 and 10 ppm sulfate (as H_2SO_4)

TABLE VI. Results of CERT Tests on Sensitized Type 304 SS Specimens[a] (Heat No. 30956) in High-Purity Water at 289°C and $\dot{\varepsilon} = 1 \times 10^{-6}$ s^{-1}

Test[b] No.	EPR, C/cm^2	Feedwater Chemistry				Failure Time, h	Maximum Stress, MPa	Total Elong., %	Reduction in Area, %	Fracture Morphology[c]
		Oxygen, ppm	Hydrogen, ppm	Cond., µS/cm	pH at 25°C					
1	2	7.3	0	0.3	6.8	117	472	36	34	0.63D, 0.37I
71	2	0.87	0	0.08	6.3	69	393	25	37	0.40D, 0.60G_3
2	2	0.25	0	0.2	6.8	143	492	50	52	0.69D, 0.31T
31	2	0.13	0.5	0.2	6.4	103	490	37	61	0.36D, 0.56T, 0.08I
4	2	0.05	0	0.1	6.8	141	492	50	54	0.49D, 0.51T
45	2	0.06	0.5	0.1	6.1	120	512	42	41	0.76D, 0.24T
33	2	0.03	0.3	0.1	6.6	127	507	45	43	0.69D, 0.31T
9	20	8.0	0	0.2	6.1	62	346	23	24	0.12D, 0.88I
70	20	0.92	0	0.07	6.4	84	447	30	34	0.71D, 0.29I
8	20	0.20	0	0.2	6.8	119	512	42	45	0.32D, 0.68G_1
32	20	0.18	0.4	0.2	6.6	127	494	45	49	0.58D, 0.35T, 0.07I
74	20	0.08	2.0	0.1	6.3	129	520	46	44	0.73D, 0.27T
46	20	0.07	0.5	0.1	6.3	127	486	46	46	0.74D, 0.26T
24	20	0.03	0	0.1	6.3	119	516	42	40	0.69D, 0.31T
34	20	0.03	0.1	0.1	6.5	122	494	43	42	0.69D, 0.31T

[a]Specimens were exposed to the environment for ~20 h at 289°C before straining.

[b]For solution-annealed material in helium at 289°C and a strain rate of 2.6×10^{-6} s^{-1}, the maximum stress was 552 MPa. The uniform and total elongations were 46.8 and 54.7%, respectively, and the reduction in area was 75%. The corresponding values for sensitized material (700°C for 12 h, EPR = 20 C/cm^2) were 525 MPa; 43.1 and 51.5% for the uniform and total elongations, respectively; and a reduction in area of 67%.

[c]Ductile (D), transgranular (T), granulated (G), intergranular (I), in terms of the fraction of the reduced cross-sectional area. Characterization of the fracture surface morphologies is in accordance with the illustrations and definitions provided in Alternate Alloys for BWR Pipe Applications: Sixth Semiannual Progress Report, April-September 1980, General Electric Company Report NEDC-23750-8, pp. 5-70 to 5-81.

TABLE VII. Results of CERT Tests on Type 304 SS Specimens[a] (Heat No. 30956) in Water with Different Oxygen and Sulfate (H_2SO_4) Concentrations at 289°C and $\dot{\varepsilon} = 1 \times 10^{-6}$ s^{-1}

Test No.	EPR, C/cm^2	Feedwater Chemistry				Failure Time, h	Maximum Stress, MPa	Total Elong., %	Reduction in Area, %	Fracture Morphology[b]
		Oxygen, ppm	Sulfate, ppm	Cond., µS/cm	pH at 25°C					
30	2	8.0	10.0	80.0	3.8	52	339	19	16	0.10D, 0.90I
28	2	8.6	1.0	9.0	4.8	37	289	10	11	0.16D, 0.84I
22	2	7.0	0.1	0.9	5.8	32	263	11	8	0.18D, 0.82I
56	2	0.21	10.0	71.0	3.8	46	313	17	29	0.15D, 0.85G_3
19	2	0.20	1.0	8.0	4.8	40	277	14	11	0.06D, 0.94I
16	2	0.18	0.1	0.9	5.8	39	290	14	14	0.12D, 0.88I
17	2	0.18	0.1	0.9	5.8	49	315	18	10	0.08D, 0.06G_1, 0.86I
18	2	0.19	0.01	0.2	6.2	82	432	29	20	0.29D, 0.71(T+G_3)
25	2	0.08	0.1	0.8	5.8	45	330	16	12	0.18D, 0.82G_3
53	2	0.03	10.0	71.0	3.8	65	384	24	23	0.25D, 0.75I
10	2	0.03	1.0	8.0	4.7	116	489	41	40	0.43D, 0.57G_3
20	2	0.03	0.1	0.8	5.8	121	521	43	38	0.72D, 0.28T
29	20	8.0	10.0	80.0	3.8	60	363	21	17	0.13D, 0.87I
27	20	7.0	1.0	9.0	4.8	57	373	20	18	0.22D, 0.78I
23	20	7.0	0.1	0.9	5.8	69	375	24	11	0.08D, 0.92I
55	20	0.20	10.0	71.0	3.8	55	342	20	17	0.21D, 0.79I
21	20	0.21	1.0	9.0	4.8	56	383	20	25	0.36D, 0.64(I+T)
13	20	0.22	0.1	0.9	5.8	78	439	27	37	0.38D, 0.43T, 0.19I
14	20	0.20	0.1	0.8	5.3	78	461	28	23	0.51D, 0.27T, 0.22I
26	20	0.08	0.1	0.8	5.8	77	438	27	46	0.36D, 0.37T, 0.27I
54	20	0.02	10.0	71.0	3.8	74	353	27	23	0.15D, 0.85I
11	20	0.05	1.0	8.0	4.7	104	492	37	27	0.45D, 0.55G_3
15	20	0.03	0.1	0.9	5.8	109	516	39	32	0.43D, 0.57(G_1+T)

[a]Specimens were exposed to the environment for ~20 h at 289°C before straining.

[b]Ductile (D), transgranular (T), granulated (G), intergranular (I), in terms of the fraction of the reduced cross-sectional area. Characterization of the fracture surface morphologies is in accordance with the illustrations and definitions provided in Alternate Alloys for BWR Pipe Applications: Sixth Semiannual Progress Report, April-September 1980, General Electric Company Report NEDC-23750-8, pp. 5-70 to 5-81.

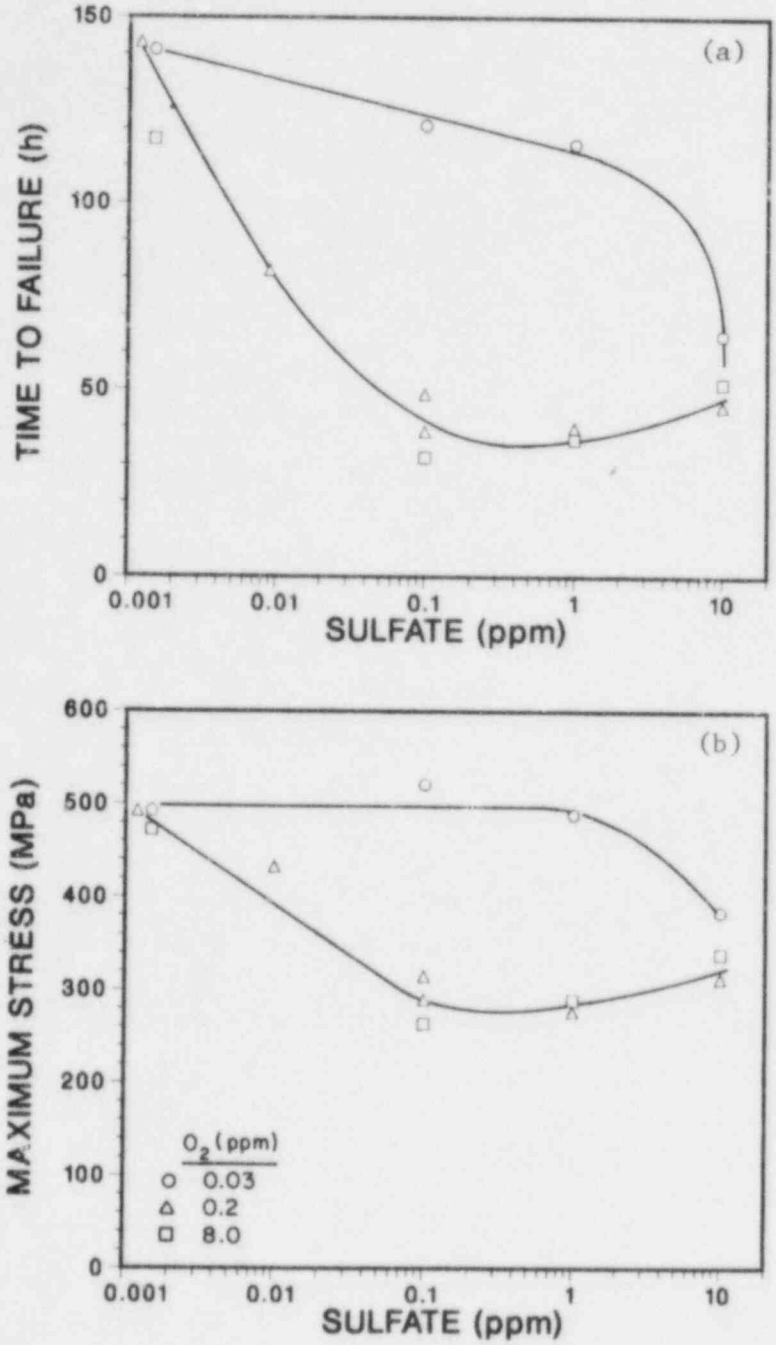

Fig. 26. Influence of Sulfate Concentration (as H_2SO_4) on (a) Time to Failure and (b) Maximum Stress of Lightly Sensitized (EPR = 2 C/cm^2) Type 304 SS in CERT Experiments at a Strain Rate of 1 x 10^{-6} s^{-1} in 289°C Water with ~0.03, 0.2, and 8 ppm Oxygen. Data points at a sulfate concentration of 0.001 ppm represent experiments in high-purity water in which no sulfate was added to the feedwater.

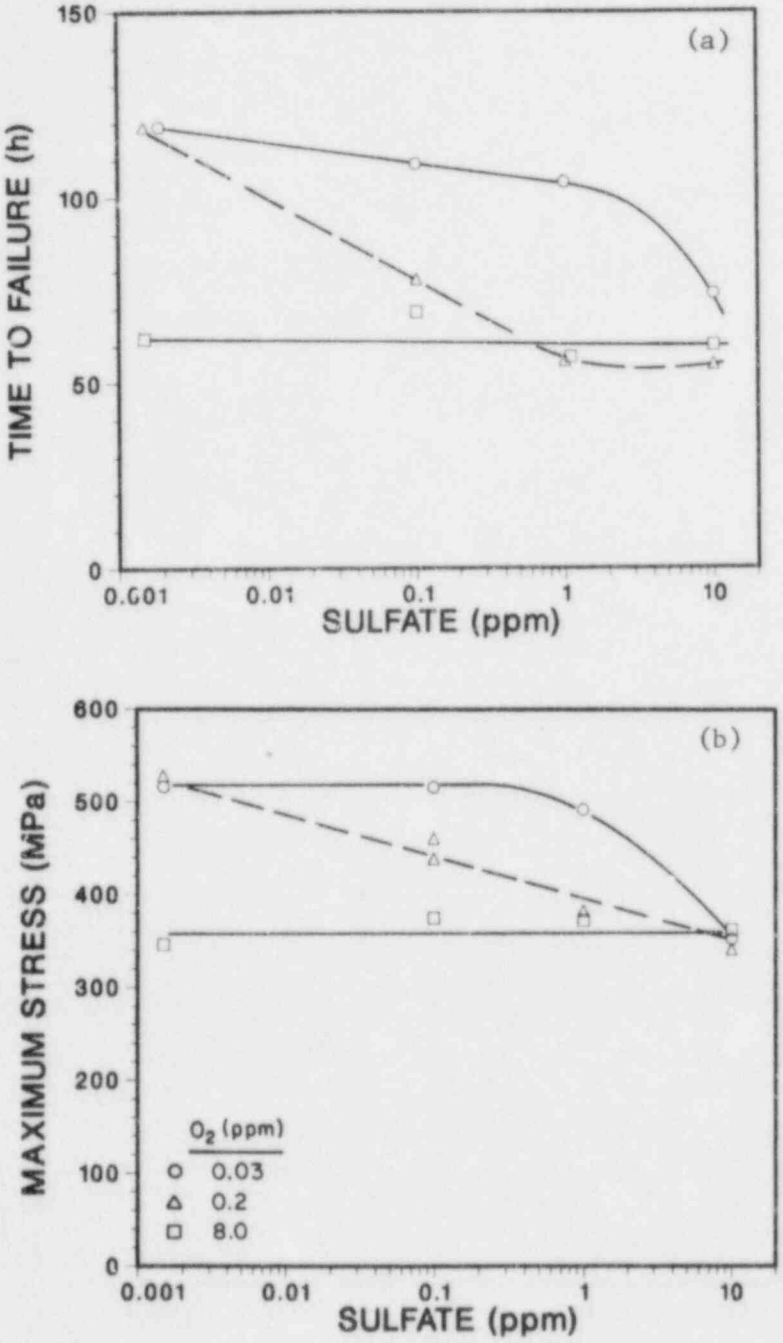

Fig. 27. Influence of Sulfate Concentration (as H_2SO_4) on (a) Time to Failure and (b) Maximum Stress of Moderately Sensitized (EPR = 20 C/cm^2) Type 304 SS in CERT Experiments at a Strain Rate of 1 x 10^{-6} s^{-1} in 289°C Water with ~0.03, 0.2, and 8 ppm Oxygen. Data points at a sulfate concentration of 0.001 ppm represent experiments in high-purity water in which no sulfate was added to the feedwater.

TABLE VIII. Results of CERT Tests on Sensitized Type 304 SS Specimens[a] (Heat No. 30956) in Water with Different Oxygen, Hydrogen, and Sulfate (H_2SO_4) Concentrations at 289°C and $\dot{\varepsilon} = 1 \times 10^{-6}$ s^{-1}

Test No.	EPR, C/cm^2	Feedwater Chemistry					Failure Time, h	Maximum Stress, MPa	Total Elong., %	Reduction in Area, %	Fracture Morphology[b]
		Oxygen, ppm	Hydrogen, ppm	Sulfate, ppm	Cond., µS/cm	pH at 25°C					
57	2	0.25	0.5	10.0	71.0	3.8	64	364	23	27	0.21D, $0.79G_3$
39	2	0.20	0.5	1.0	8.0	4.8	45	291	16	15	0.19D, 0.81I
35	2	0.18	0.6	0.1	0.8	5.8	74	413	26	27	0.49D, 0.51I
41	2	0.20	0.5	0.01	0.2	6.1	81	493	29	29	0.58D, 0.42I
47	2	0.07	0.5	0.1	0.9	5.8	133	500	48	48	0.57D, 0.43T
51	2	0.03	0.5	10.0	71.0	3.8	67	383	24	25	0.30D, $0.70G_3$
49	2	0.03	0.5	1.0	8.0	4.8	119	495	43	40	0.45D, $0.55G_2$
37	2	0.05	0.5	0.1	0.8	5.8	129	510	46	46	0.43D, 0.57T
59	2	0.03	0.5	0.1	0.8	5.8	118	504	43	48	0.63D, 0.37T
43	2	0.03	0.5	0.01	0.2	6.1	128	514	45	46	0.67D, 0.33T
58	20	0.23	0.5	10.0	71.0	3.8	66	349	24	23	0.34D, $0.66G_3$
40	20	0.20	0.5	1.0	8.0	4.8	51	261	18	21	0.35D, 0.65I
36	20	0.20	0.5	0.1	0.9	5.8	80	425	38	38	0.46D, 0.32T, 0.22I
52	20	0.03	0.5	10.0	69.0	3.8	72	356	26	27	0.28D, 0.72I
50	20	0.03	0.5	1.0	8.0	4.8	115	502	42	34	0.70D, $0.30G_2$
38	20	0.05	0.5	0.1	0.8	5.8	124	499	44	44	0.68D, 0.32T
44	20	0.02	0.5	0.01	0.2	6.1	125	513	44	45	0.70D, 0.30T

[a]Specimens were exposed to the environment for ~20 h at 289°C before straining.

[b]Ductile (D), transgranular (T), granulated (G), intergranular (I), in terms of the fraction of the reduced cross-sectional area. Characterization of the fracture surface morphologies is in accordance with the illustrations and definitions provided in Alternate Alloys for BWR Pipe Applications: Sixth Semiannual Progress Report, April-September 1980, General Electric Company Report NEDC-23750-8, pp. 5-70 to 5-81.

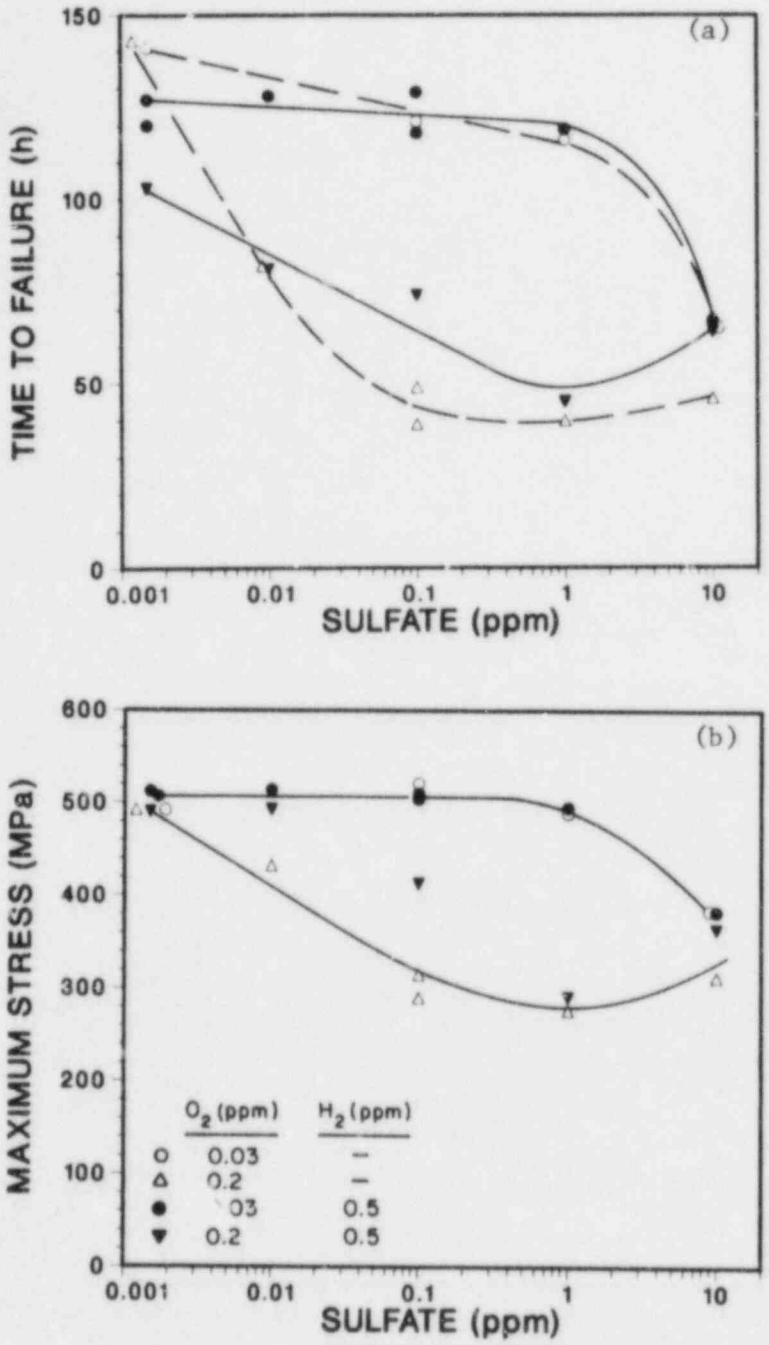

Fig. 28. Influence of ~0.5 ppm Hydrogen (Solid Symbols) at Several Sulfate Concentrations on (a) Time to Failure and (b) Maximum Stress of Lightly Sensitized (EPR = 2 C/cm^2) Type 304 SS Specimens in CERT Experiments at a Strain Rate of 1 x 10^{-6} s^{-1} in 289°C Water with 0.03 or 0.2 ppm Oxygen. Data points at a sulfate concentration of 0.001 ppm represent high-purity water in which no sulfate was added to the feedwater.

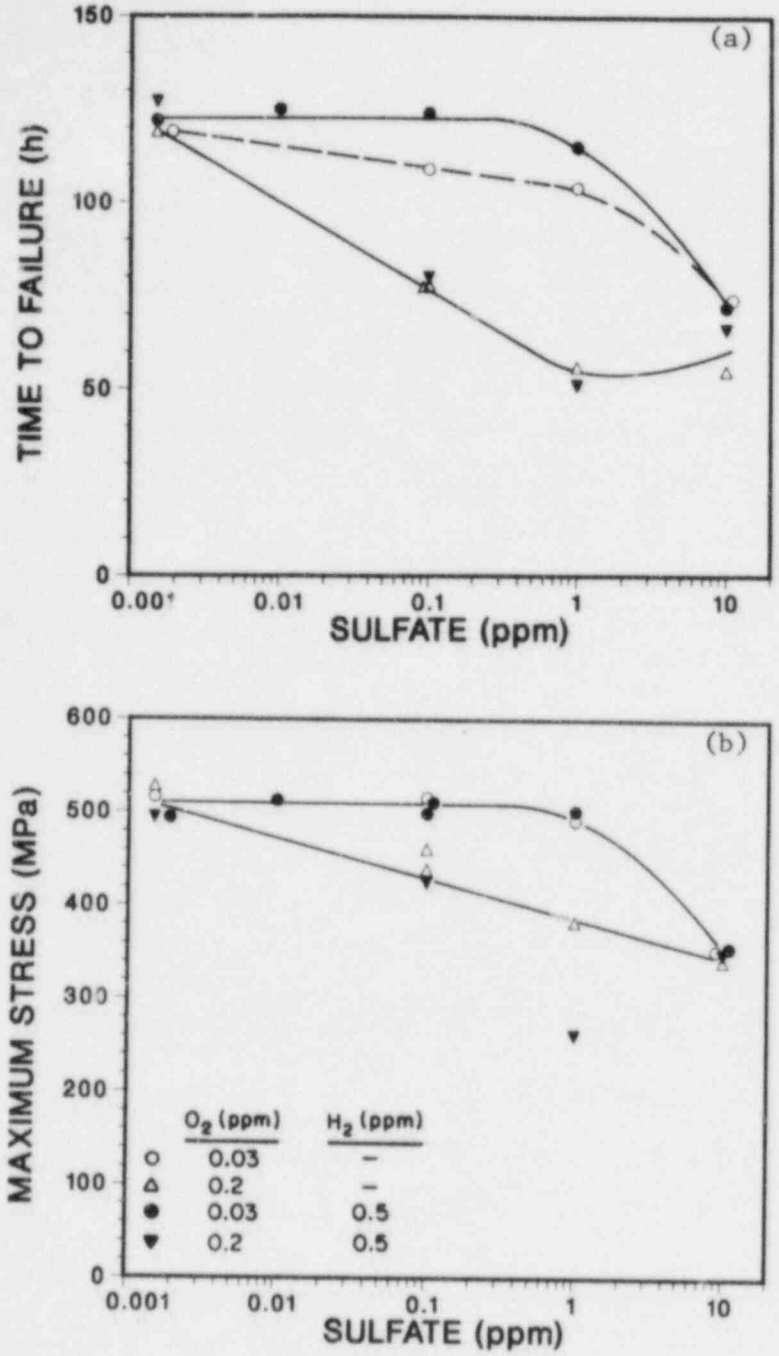

Fig. 29. Influence of ~0.5 ppm Hydrogen (Solid Symbols) at Several Sulfate Concentrations on (a) Time to Failure and (b) Maximum Stress of Moderately Sensitized (EPR = 20 C/cm^2) Type 304 SS Specimens in CERT Experiments at a Strain Rate of 1 x 10^{-6} s^{-1} in 289°C Water with 0.03 or 0.2 ppm Oxygen. Data points at a sulfate concentration of 0.001 ppm represent high-purity water in which no sulfate was added to the feedwater.

is summarized in Table IX. The results show that a factor-of-four increase in the dissolved hydrogen concentration, at a constant impurity level, had a relatively small effect on the CERT parameters. The fracture mode, although primarily intergranular, revealed a perceptible trend toward a more ductile failure in terms of the fraction of the reduced cross-sectional area as the hydrogen concentration increased from 0 to 2 ppm. As indicated in Tables VIII and IX, a ductile-plus-transgranular failure mode was observed for sulfate concentrations of $\lesssim$0.1 ppm at a dissolved oxygen concentration of ~0.03 ppm. These results clearly indicate that continuous additions of hydrogen to the feedwater of a BWR, which suppress the dissolved oxygen concentration of the coolant entering the recirculation piping to a very low level, will decrease the IGSCC susceptibility of the steel by a considerable margin provided impurities are also maintained at very low levels.

b. Crack Growth Results on Type 304 SS in Simulated BWR-Quality Water at 289°C

Fracture-mechanics-type crack growth tests are in progress on the same heat of material as in the CERT experiments. Three 1TCT specimens of Type 304 SS in the solution-annealed and sensitized conditions (EPR = 0, 2, and 20 C/cm^2) were stressed in series at an R value of 0.95; K_{max} values ranging from 28 to 72 MPa$\cdot$m$^{1/2}$ were used for the specimens with the highest level of sensitization. The cyclic frequencies, based on the slow rising-load periods (unloading occurred within ~1 s and was therefore neglected), were 8×10^{-2}, 8×10^{-3}, and 8×10^{-4} Hz for different phases of the experiment in 289°C high-purity water with 8 ppm dissolved oxygen. The crack growth rate data were reported in Table VIII of the previous report.[24]

The actual crack lengths in the specimens, measured after separation of the uncracked ligament, were in excellent agreement with values determined by compliance measurements during the test. As shown in Fig. 30, the crack fronts were uniform across the specimen thickness. The compliance measurements and the fractograph in Fig. 30c indicate that no crack growth occurred in the solution-annealed (EPR = 0) specimen during the test. The greater crack depth (Fig. 30a) and higher crack growth rate for the moderately sensitized material are consistent with the relative IGSCC susceptibility of

TABLE IX. Effect of Hydrogen Concentration in the Feedwater on the SCC Susceptibility of Sensitized Type 304 SS in CERT Experiments[a] at 289°C in Water with ~0.03 ppm Dissolved Oxygen and 0, 1, and 10 ppm Sulfate as H_2SO_4

Test No.	EPR, C/cm^2	Feedwater Chemistry					Failure Time, h	Maximum Stress, MPa	Total Elong., %	Reduction in Area, %	Fracture Morphology[b]
		Oxygen, ppm	Hydrogen, ppm	Sulfate, ppm	Cond., µS/cm	pH at 25°C					
62	2	0.03	2.0	10.0	71.5	3.8	72	373	26	31	0.21D, $0.79G_3$
51	2	0.03	0.5	10.0	71.0	3.8	67	383	24	25	0.30D, $0.70G_3$
53	2	0.03	0	10.0	71.0	3.8	65	384	24	23	0.25D, 0.75I
60	2	0.01	2.0	1.0	8.3	4.8	103	478	37	35	0.56D, $0.44G_2$
49	2	0.03	0.5	1.0	8.0	4.8	119	495	43	40	0.45D, $0.55G_2$
10	2	0.03	0	1.0	8.0	4.8	116	489	41	40	0.43D, $0.57G_3$
33	2	0.03	0.3	0	0.1	6.1	120	512	42	41	0.76D, 0.24T
4	2	0.05	0	0	0.1	6.8	141	492	50	54	0.49D, 0.51T
63	20	0.03	2.0	10.0	71.5	3.8	79	388	29	22	0.24D, 0.76I
52	20	0.03	0.5	10.0	69.0	3.8	72	356	26	27	0.28D, 0.72I
54	20	0.02	0	10.0	71.0	3.8	74	353	27	23	0.15D, 0.85I
61	20	0.02	2.0	1.0	8.3	4.8	121	510	44	42	0.68D, $0.32G_2$
50	20	0.03	0.5	1.0	8.0	4.8	115	502	42	34	0.70D, $0.30G_2$
11	20	0.05	0	1.0	8.0	4.8	104	492	37	27	0.45D, $0.55G_3$
34	20	0.03	0.1	0	0.1	6.5	122	494	43	42	0.69D, 0.31T
24	20	0.03	0	0	0.1	6.3	119	516	42	40	0.69D, 0.31T

[a]Specimens were exposed to the environment for ~20 h at 289°C before straining.
[b]Ductile (D), transgranular (T), granulated (G), intergranular (I), in terms of the fraction of the reduced cross-sectional area. Characterization of the fracture surface morphologies is in accordance with the illustrations and definitions provided in Alternate Alloys for BWR Pipe Applications: Sixtn Semiannual Progress Report, April-September 1980, General Electric Company Report NEDC-23750-8, pp. 5-70 to 5-81.

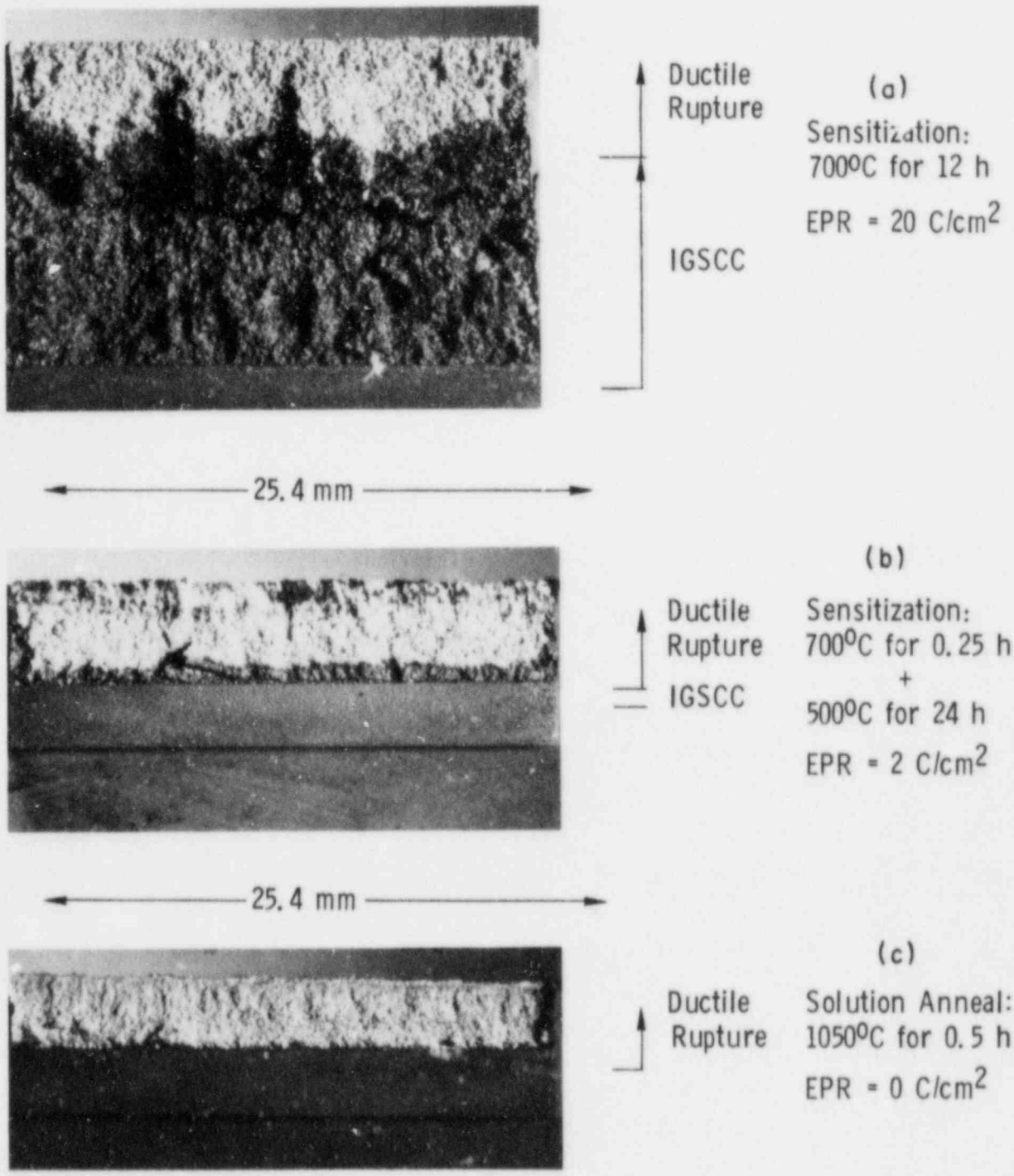

Fig. 30. Fracture Surfaces of Type 304 SS 1TCT Specimens (Heat 30956) from a Cyclic Crack Growth Experiment under High-R (0.95) Loading in High-Purity Water with 8 ppm Dissolved Oxygen at 289°C.

the material in CERT experiments at 289°C in oxygenated high-purity water at a strain rate of 1×10^{-6} s^{-1}.

Another crack growth experiment in high-purity water with 8 ppm dissolved oxygen is in progress to provide additional information on the effect of frequency and K_{max} on the crack growth rate at 289°C and an R value of 0.95. Two 1TCT specimens of the same heat of Type 304 SS were sensitized to an EPR value of 20 C/cm^2, fatigue precracked in air at 289°C (to minimize the long period for crack initiation noted in the previous experiment), and stressed in the environment at an initial K_{max} and frequency of 43 $MPa \cdot m^{1/2}$ and 8×10^{-2} Hz, respectively. The initial crack growth rates appear to be somewhat lower than those from the previous experiment in this environment.

A crack growth experiment in an identical MTS-autoclave system is in progress to investigate the effect of impurities, viz., H_2SO_4 from decomposition of ion exchange resins, on the cyclic crack growth properties of the steel at 289°C. Instrumented 1TCT specimens with EPR values of 0, 2, and 20 C/cm^2 were fatigue precracked in air at 289°C to provide 3-mm-deep starter cracks, and are being tested in water containing 0.2 ppm dissolved oxygen and 0.1 ppm sulfate (as H_2SO_4), which is within Nuclear Regulatory Guide 1.56 limits on pH and specific conductance for BWR operation at >1% power. The initial results obtained under cyclic loading with a positive sawtooth waveform, high R (0.95), K_{max} of 28 $MPa \cdot m^{1/2}$, and frequency of 8×10^{-2} Hz indicate that the lightly sensitized specimen (EPR = 2 C/cm^2) exhibits the highest crack growth rate in the impurity environment, which again is consistent with the relative susceptibility of the materials with the two levels of sensitization in the CERT experiments. In contrast to the experiment in 289°C water with 8 ppm dissolved oxygen, the condition for steady-state crack growth is closely related to our ability to maintain the dissolved oxygen concentration in the water at ~0.2 to 0.3 ppm. A somewhat higher oxygen level in the feedwater is required to compensate for loss of oxygen due to corrosion of the autoclave system at the low flow rate of ~0.6 ℓ/h. The dissolved oxygen in the effluent stream is monitored and the partial pressure of oxygen over the feedwater is adjusted to maintain the desired value in the experiment. The crack growth rate results will be used in various analyses to establish the optimum inspection levels and the useful service life of components containing flaws of known dimensions.

II. TRANSIENT FUEL RESPONSE AND FISSION PRODUCT RELEASE

Principal Investigator:
J. Rest

A. Introduction

A physically realistic description of fuel swelling and fission gas release is needed to aid the prediction of the behavior of fuel rods and fission gases under certain hypothetical LWR accident conditions. To satisfy this need, a comprehensive computer-based model (the Steady-State and Transient Gas-Release and Swelling Subroutine, or GRASS-SST) and its faster-running versions (FASTGRASS and PARAGRASS) are being developed at ANL. These models are being incorporated into the Transient Fuel-Rod Analysis Program (FRAP-T) and the Severe Core Accident Damage Analysis Program (SCDAP) being developed by EG&G Idaho, Inc. at the Idaho National Engineering Laboratory (INEL), and into the FRAPCON code under development at PNL.

The analytical effort is supported by a data base and correlations developed from characterization of irradiated LWR fuel and from out-of-reactor transient heating tests of irradiated commercial and experimental LWR fuel under a range of thermal conditions (performed at ANL and ORNL) and from the results of the structural damage program at EG&G Idaho.

B. PARAGRASS, A Quick-running, Comprehensive Steady-State and Transient Fission Product Release and Swelling Model for Water-Reactor Fuel: Model Description and User's Guide (J. Rest and S. A. Zawadzki)

1. Description of PARAGRASS

PARAGRASS is an extremely efficient, mechanistic computer code with the capability of modeling steady-state and transient fission-product behavior. The models of PARAGRASS are based on the more detailed ones in FASTGRASS.[25,26] As there are no significant differences in the methodologies of the two codes, PARAGRASS is sufficient to provide a comprehensive treatment of fission product behavior. The major differences between PARAGRASS and FASTGRASS are in the treatment of volatile fission products (VFPs) and in models for the migration of fission products up the temperature gradient.

PARAGRASS is ideally suited for incorporation into a whole-core accident analysis code which has the capability of providing PARAGRASS with the relevant fuel operating conditions (e.g., fuel temperatures). PARAGRASS includes a driver which accepts fuel operating conditions; it can be directly interfaced with a thermal-mechanical code with a minimum of difficulty by invoking an appropriate udpate. PARAGRASS has undergone verification with available steady-state and transient experimental data on fission gas behavior.

2. Theory

a. Overview

PARAGRASS treats gas release from the fuel matrix to the plenum and other free volumes (e.g., pellet-pellet interfaces) as a three-step process: (1) release of gas from within the fuel grains to the grain faces, (2) transport along the faces to grain edges, and (3) release along extensively interconnected edge pores to the fuel exterior. It models fission gas present in the fuel either as single gas atoms or as gas bubbles. For simplicity, PARAGRASS models the evolution of an average-sized bubble (representative of the entire size distribution that would occur in reality) for each fuel region of interest (i.e., one for the lattice population, another for the grain face population, and a third for the edge population). In addition to the three-step gas release process described above, PARAGRASS has the capability of modeling "microcracking" or grain boundary separation, a phenomenon that is driven by the overpressurization of fission gas bubbles (residing on grain boundaries) in a thermal transient. Microcracking has been experimentally observed[25,27] and is thought to enhance transient fission-gas release by providing short-circuiting pathways along grain faces to grain edges as well as to the fuel exterior. In addition, microcracking can severely degrade the thermal conductivity of the nuclear fuel. The DiMelfi-Deitrich grain boundary separation model[28] has been incorporated into PARAGRASS.

b. Sequence of Events in Gas Release

(1) Intragranular Phenomena

Fission-generated atoms of noble gas reside within grains of nuclear fuel. These noble gas atoms, which are insoluble in the fuel matrix, nucleate into bubbles in the lattice. At any instant, however, reactor fuel will contain fission gas in bubbles as well as in the atomic form. Re-solution of bubbles due to collision with energetic fission fragments as well as fission-induced generation of gas atoms will ensure that there is gas present in the atomic form. Any realistic fission-gas model must thus consider the transport of both gas atoms and bubbles. PARAGRASS has models for bubble nucleation due to collisions of gas atoms and for bubble re-solution. It considers the random (concentration-gradient driven) and biased (temperature-gradient driven) migration of gas atoms and bubbles from the lattice to the grain faces.

(2) Diffusive Flow

In modeling the behavior of fission gas in nuclear fuel, it is necessary to calculate the loss of gas to the grain boundaries by diffusion of single gas atoms and gas bubbles. To simplify the problem, grains within the fuel are assumed to be spherical. If the only sink for gas atoms is the boundary itself, the concentration of gas atoms, C_g, within the spherical grain satisfies the equation

$$\frac{\partial C_g}{\partial t} = \frac{1}{r^2} \frac{\partial}{\partial r} \left(D_g r^2 \frac{\partial C_g}{\partial r} \right) + K_g, \tag{28a}$$

where D_g is the gas atom diffusion coefficient and K_g the rate of generation of gas atoms. In general, Eq. (28a) is solved with the boundary conditions

$$C_g = 0 \text{ at } t = 0 \text{ for } 0 \leq r \leq d_g/2, \tag{28b}$$

$$C_g = 0 \text{ at } r = d_g/2 \text{ for } t_o \leq t \leq t_o + h, \tag{28c}$$

$$\frac{\partial C_g}{\partial r} = 0 \text{ at } r = 0 \text{ for } t_o \leq t \leq t_o + h, \tag{28d}$$

where d_g is the grain diameter. An analogous equation describing the intragranular diffusion of gas bubbles to the grain boundaries can also be defined. However, the problem of calculating the diffusive flow of gas atoms and bubbles to a spherical boundary is not so straightforward if real irradiation histories are to be followed, with changing gas generation rates and temperatures: In this case, no general analytical solution is possible. Additional complications are provided by the processes of gas atom re-solution, gas atom trapping by gas bubbles, gas bubble nucleation, and bubble coalescence.

The problem of calculating diffusive flow of fission gas to the grain boundaries for the case of changing gas generation rates and temperatures has previously been handled by obtaining the general solution of Eq. (28a) as the sum of the solutions to two separate problems:

Problem 1

Equation 28a is solved with the boundary conditions

$$C = 0 \text{ at } t = t_o \text{ for } 0 \leq r \leq d_g/2, \tag{28e}$$

$$C = 0 \text{ at } r = d_g/2 \text{ for } t_o \leq t \leq t_o + h, \tag{28f}$$

$$\frac{\partial C}{\partial t} = 0 \text{ at } r = 0 \text{ for } t_o \leq t \leq t_o + h, \tag{28g}$$

to give

$$C(r,t) = -\sum_m (-1)^m \frac{2K_g a^3}{D_g \pi^3 m^3} \frac{\sin(m\pi r/a)}{r}\left[1 - \exp\left(-D_g m^2 \pi^2 t/a^2\right)\right], \tag{29}$$

where $a = d_g/2$.

The flux of gas atoms to the grain boundary is given by

$$J = -\frac{3D_g}{a}\left(\frac{\partial C}{\partial r}\right)_{r=a}. \tag{30}$$

From Eqs. (29) and (30), the gas-atom flux to the grain boundaries for Problem 1 is

$$J_1 = \frac{6K_g}{\pi^2} \sum_{m=1}^{\infty} \frac{1}{m^2} \left[1 - \exp\left(-D_g m^2 \pi^2 t/a^2\right)\right] . \tag{31}$$

Problem 2

The equation

$$\frac{\partial C}{\partial t} = \frac{D_g}{r^2} \frac{\partial}{\partial r} \left(r^2 \frac{\partial C}{\partial r}\right) \tag{32a}$$

is solved with the boundary conditions

$$C(r,t_o) = \bar{C}(t_o) \text{ at } t = t_o \text{ for } 0 \leq r \leq d_g/2, \tag{32b}$$

where $\bar{C}(t_o)$ is the average concentration within the grain at $t = t_o$,

$$C(r,t_o) = 0 \text{ at } r = d_g/2 \text{ for } t_o < t \leq t_o + h, \tag{32c}$$

$$\frac{\partial C(r,t)}{\partial t} = 0 \text{ at } r = 0 \text{ for } t_o \leq t \leq t_o + h, \tag{32d}$$

to give

$$C(r,t) = \frac{-2\bar{C}}{\pi} \sum_{m=1}^{\infty} \frac{(-1)^m}{m} a \sin(m\pi r/a) r \exp\left(-m^2\pi^2 D_g t/a^2\right) . \tag{33}$$

From Eq. (30), the gas atom flux to the grain boundaries for Problem 2 is

$$J_2 = \frac{6D_g}{a^2} \bar{C} \sum_{m=1}^{\infty} \exp\left(-m^2\pi^2 D_g t/a^2\right). \tag{34}$$

Physically, Problem 1 describes the behavior of the gas generated after the change of irradiation conditions, at t_o, and Problem 2 deals with the behavior, after t_o, of the gas generated prior to the change of conditions. The general solution to Eq. (28a) for changing gas generation rates and temperatures is the sum of Eq. (31) and Eq. (34).

An efficient, accurate numerical algorithm was used for evaluating the infinite series in Eqs. (31) and (34). Direct evaluation of the infinite series was determined to be necessary after the results of analyses indicated that the constraints on t imposed by the "usual" approximations to the infinite series were being violated for a significant range of operating conditions.

The diffusive flow of fission gas bubbles to the grain boundaries is also considered. For this case, if it is assumed that gas bubbles are not being nucleated and are essentially non-interacting from $t = t_o$ to $t = t_o + h$, then the solution for the flux of bubbles to the grain boundary is given by Eq. (34), where D_g becomes the gas bubble diffusivity and $\overline{C}$ is the average concentration of the average-sized gas bubbles within the grain at $t = t_o$.

The coupling of the diffusive flow problem to other processes affecting fission gas behavior (e.g., gas atom re-solution, gas atom trapping by gas bubbles, and gas bubble nucleation and coalescence) is accomplished by solving for the intragranular densities of gas atoms and average-sized gas bubbles, by use of equations of the following form:

$$\frac{dY_i}{dt} = -a_i Y_i^2 - b_i Y_i + c_i. \qquad (35)$$

The meanings of the variables used in Eq. (35) are described in Table X.

TABLE X. Definition of Variables in Eq. (35), $\frac{dY_i}{dt} = -a_i Y_i^2 - b_i Y_i + c_i$

Y_i	$a_i Y_i^2$	$b_i Y_i$	c_i
Density of intragranular gas atoms	Rate at which gas atoms are lost owing to gas bubble nucleation	Rate at which gas atoms are lost owing to diffusive flow to the grain boundaries and diffusion into gas bubbles	Rate at which gas atoms are gained owing to gas atom re-solution and fission of uranium nuclei
Density of intragranular gas bubbles	Rate at which gas bubbles are lost owing to bubble coalescence	Rate at which gas bubbles are lost owing to diffusive flow to the grain boundaries and gas atom re-solution	Rate at which gas bubbles are gained owing to bubble nucleation and diffusion of gas atoms into bubbles

An analogous set of equations is used to characterize the average-sized bubbles on the grain faces and along the grain edges. The full set of coupled equations is solved incrementally as a function of time.

M. H. Wood and J. R. Matthews[29] have identified inaccuracies in the above approach for calculating the diffusive flow of gas atoms to a spherical boundary, i.e., Eqs. (28a,e,f,g) and (32a-d). Furthermore, the calculated release is heavily dependent on the number of time steps taken during a given irradiation period and is always above the true release. The inaccuracies found were identified with the assumption $C(r,t_o) = \overline{C}(t_o)$ (i.e., Eq. 32b) in the derivation of Eq. (34). The assumption that the gas is uniformly distributed throughout the grain at the beginning of each time step results in an artificial surge of gas to the grain boundaries at that time.

Matthews and Wood[30] have suggested an approach to solving the problem of diffusive flow to a spherical boundary which uses an approximation describing the intragranular concentrations of the diffusing gas atoms and bubbles in terms of quadratic functions in two concentric regions. A variational principle is used to calculate the radial distribution of the concentration. Note that this approach is in sharp contrast to the approach described above, which assumes a uniform concentration of the diffusing gas forms within the grain.

The concentration of gas atoms in a spherical grain described by Eq. (28a) is written as $C_g^o(r)$ at a time t. After a small time interval δt the concentration becomes $C_g(r)$. Using the backward Euler approximation, for small δt, Eq. (28a) may be replaced by

$$\frac{1}{r^2}\frac{d}{dr}\left(D_g r^2 \frac{dC_g}{dr}\right) - \frac{C_g}{\delta t} + \frac{C_g^0}{\delta t} + K_g = 0. \tag{36}$$

Euler's theorem may now be used to obtain a variational principle equivalent to Eq. (36):

$$\delta \int_0^{\frac{1}{2}} d_g \; 4\pi \left[\frac{D_g}{2}\left(\frac{dC_g}{dr}\right)^2 + \frac{C_g^2}{2\,\delta t} - \left(\frac{C_g^o}{\delta t} + K_g\right) C_g\right] r^2 dr = 0, \tag{37}$$

which assumes that Dirichlet boundary conditions are to be applied. Matthews and Wood showed that an approximate solution to the problem may now be obtained by choosing a trial function that satisfies the boundary conditions and minimizes the integral in Eq. (37) in terms of free parameters in the function. Many types of trial function could be chosen, but Matthews and Wood claim that piece-wise functions are easier to handle than global functions. Quadratic functions are attractive as they allow an exact representation of Eq. (28a) for long times. To meet their objectives of a realistic level of accuracy with a minimum of computer storage and running time, Matthews and Wood split the spherical grain into two concentric regions of approximately equal volume. In each region, the gas concentration is represented by a quadratic function. In the central region I (see Fig. 31), the concentration function is constrained to have $dC_g/dr = 0$ at $r = 0$. In the outer region II, the concentration function is constrained to a value of $C_g = 0$ at $r = d_g/2$. The two functions are also constrained to be continuous at the common boundary of the two regions. This leaves three free parameters. Matthews and Wood choose these to be the concentrations C_1, C_2, and C_3 given respectively by the radius ratios $\rho_1 = 0.4$, $\rho_2 = 0.8$ and $\rho_3 = 0.9$ where $\rho \equiv 2r/d_g$. These positions are the midpoint radius of region I, the boundary between the regions, and the midpoint radius of region II, respectively. Thus, the trial functions are as follows:

$$C_g = C_1(0.64 - \rho^2)/0.48 + C_2(\rho^2 - 0.16)/0.48 \text{ (region I)}; \tag{38}$$

$$C_g = C_2 5(10\rho^2 - 19\rho + 9) + C_3 10(18\rho - 10\rho^2 - 8) \text{ (region II)}. \tag{39}$$

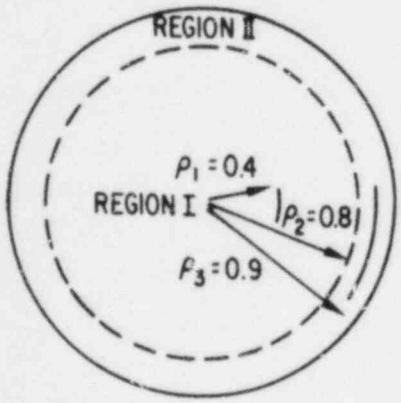

Fig. 31

Configuration of the Two-Zone Model Used in Ref. 30.

Equations (38) and (39) are substituted for C_g in Eq. (37) and an extremum found by differentiating with respect to C_1, C_2, and C_3 in turn. A set of three linear equations is thus obtained:

$$
\begin{aligned}
&(q_1 D_g/d_g^2 + q_2/\delta t)C_1 + (q_3 D_g/d_g^2 + q_4/\delta t)C_2 \\
&\quad = K_g q_5 + (C_1^0 q_2 + C_2^0 q_4)/\delta t, \\
&(q_3 D_g/d_g^2 + q_4/\delta t)C_1 + (q_6 D_g/d_g^2 + q_7/\delta t)C_2 + (q_8 D_g/d_g^2 + q_9/\delta t)C_3 \\
&\quad = K_g q_{10} + (C_1^0 q_4 + C_2^0 q_7 + C_3^0 q_9)/\delta t, \qquad (40) \\
&(q_8 D_g/d_g^2 + q_9/\delta t)C_2 + (q_{11} D_g/d_g^2 + q_{12}/\delta t)C_3 \\
&\quad = K_g q_{13} + (C_2^0 q_9 + C_3^0 q_{12})/\delta t,
\end{aligned}
$$

where C_1^0, C_2^0, C_3^0 are values of the concentrations at the evaluation points at the start of the time increment. The various q coefficients are integrals which when directly evaluated are, to 4 figures,

$$
\begin{aligned}
&q_1 = 4.552, && q_2 = 0.06935, && q_3 = -4.552, \\
&q_4 = 0.02167, && q_5 = 0.09102, && q_6 = 37.78, \\
&q_7 = 0.07614, && q_8 = -38.72, && q_9 = 0.008456, \\
&q_{10} = 0.01008, && q_{11} = 87.04, && q_{12} = 0.08656, \\
&q_{13} = 0.1083.
\end{aligned}
$$

The set of Eqs. (40) can be directly solved to obtain the concentrations C_1, C_2, and C_3:

$$
\begin{aligned}
C_1 &= \frac{X_1 - F_2 C_2}{F_1}, \\
C_2 &= \frac{\frac{F_2}{F_1} X_1 + \frac{F_5}{F_7} X_3 - X_2}{\frac{F_2}{F_1} F_2 + \frac{F_5}{F_7} F_5 - F_4}, \qquad (41) \\
C_3 &= \frac{X_3 - F_5 C_2}{F_7},
\end{aligned}
$$

where $F_1 = q_1 D_g/dg^2 + q_2/\delta t$, $F_2 = q_3 D_g/dg^2 + q_4/\delta t$,

$X_1 = K_g q_5 + (C_1^0 q_2 + C_2^0 q_4)/\delta t$,

$F_4 = q_6 D_g/dg^2 + q_7/\delta t$, $F_5 = q_8 D_g/dg^2 + q_9/\delta t$,

$X_2 = K_g q_{10} + (C_1^0 q_4 + C_2^0 q_7 + C_3^0 q_9)/\delta t$,

$F_7 = q_{11} D_g/dg^2 + q_{12}/\delta t$, and

$X_3 = K_g q_{13} + (C_2^0 q_9 + C_3^0 q_{12})/\delta t$.

From Eqs. (30) and (39), the gas atom flux to the grain boundaries is

$$J = \frac{D_g}{dg^2} (-60C_2 + 240C_3). \tag{42}$$

Equations (38-42) are coupled to Eq. (35) for the assessment of fission gas behavior within the grains and for the determination of the fission gas atom and gas bubble flux to the grain boundaries. For proper coupling of the diffusive flow problem to the problems of determining the gas atom densities and the gas bubble sizes and densities, information is required on the average concentration of fission gas within the grains.

Matthews and Wood[30] determined that the best expression for the average concentration within the grains, $\overline{C}_g$, is given by

$$\overline{C}_g = 0.2876C_1 + 0.2176C_2 + 0.4216C_3. \tag{43}$$

At the end of the time increment, the concentrations C_1, C_2, C_3 in Eq. (43) are scaled by imposing the condition that the average concentration calculated by use of Eq. (43) is equal to the average concentration calculated by use of Eq. (35), i.e., that

$$\overline{C}_g = Y_1.$$

The modified C_1, C_2, C_3 then become the initial values of these concentrations (i.e., C_1^0, C_2^0, C_3^0) to be used for the next time increment. The diffusive flow of fission gas bubbles is treated analogously to that for fission gas atoms, but with $K_g = 0$ in Eq. (28a).

This method of coupling diffusive flow to other processes affecting fission gas behavior (e.g., gas atom re-solution, gas atom trapping by gas bubbles, bubble nucleation) is computationally efficient and has been benchmarked against various analytical solutions.

The results of analyses performed with the theoretical FASTGRASS model[31] demonstrate that the calculations are remarkably stable with respect to time-step changes when the Matthews-Wood diffusive-flow model is used. A maximum deviation of ~2.5% obtained with the new diffusive-flow model for time steps that differ by a factor of 500 is in sharp contrast to an ~80% maximum deviation obtained by use of Eqs. (28a, e, f, g) and (29a-d). In addition, as the time step is decreased, the new theoretical results approach a constant limiting value much faster than the results obtained with the previous theory.

As discussed above, the use of Eqs. (28a, e, f, g) and (29a-d) leads to calculated intragranular releases that are always higher than the true release. In order to maintain reasonable agreement between theory and experiment, the gas atom re-solution rate used in the theory was increased from 2×10^{-5} s^{-1} (at a fission rate $\dot{f} = 4 \times 10^{12}$ $cm^{-3}s^{-1}$) to 8×10^{-5} s^{-1}. This value of gas atom re-solution rate is more consistent with the value that appears to be the most reliable experimental estimate,[32] i.e., $\sim 2.7 \times 10^{-4}$ s^{-1} for $\dot{f} = 4 \times 10^{12}$ $cm^{-3}s^{-1}$.

(3) Intergranular Phenomena at the Grain Faces

SEM examination of fuel samples subjected to direct electrical heating (DEH) tests has revealed the development of sinuous channels on grain faces after a saturation density of grain boundary fission

gas has been reached. These channels link up and extend to grain-edge tunnels, thus enhancing gas release along the faces to the edges. Channel formation on the faces is a function of the areal coverage of the face by the fission gas. A realistic approach for calculating grain-face saturation by fission gas is to deal directly with the calculated fission-gas bubble distributions. Previous analyses[25,26] have been based on the swelling of spherical bubbles. However, because experimentally, $\cos \theta = \gamma_{gb}/2\gamma \neq 0$ (γ = UO_2 surface energy, γ_{gb} = grain boundary energy), it is more reasonable to assume that the bubbles are lenticular-shaped pores, containing m gas atoms and having radius or curvature ρ, which are joined in the plane of the boundary with dihedral angles $2\theta = 100°$. The fractional swelling due to these bubbles is given by the expression

$$\frac{\Delta V}{V} = 4\pi\rho^3 f(\theta)/3Y, \tag{44}$$

where $f(\theta) = 1 - 3/2 \cos \theta + 1/2 \cos^3 \theta$,

$$\rho = \left(\frac{3mKT}{4\pi f(\theta)\gamma}\right)^{1/2}, \tag{45}$$

and Y is the number of bubbles on the grain face per unit volume. Equation (29) was derived by assuming equilibrium and using the ideal gas law. The projected areal coverage of the grain face by these bubbles per unit volume is given by

$$A = \pi(\rho \sin \theta)^2 Y. \tag{46}$$

For fixed values of m and Y, Eqs. (44-46) result in values of $\frac{\Delta V}{V}$ and A which are ~0.86 smaller and ~1.74 larger, respectively, than those calculated assuming spherical bubbles.

Grain face saturation (i.e., the initiation of gas channel formation) occurs when

$$A > A^* S_v^{\alpha\alpha}, \tag{47}$$

where $S_v^{\alpha\alpha}$ is the grain face area per unit volume and A* is the maximum areal coverage per unit area of grain face. Equations (46) and (47) do not account for local variations in the fuel microstructure. To include these effects in the calculation of grain-face channel formation, it is assumed that the local variations in fuel microstructure can be represented by the width σ_b of a distribution of A such that the probability of enhanced gas release from the grain faces to the grain edges due to formation of grain face channels is given by

$$P_A = \frac{1}{\sigma_b\sqrt{2\pi}} \int_{x = A^* S_v^{\alpha\alpha}} \exp[-(x - A)^2/2\sigma_b^2]dx. \qquad (48)$$

The width σ_b of the distribution in Eq. (48) is a function of erratic structural parameters that depend on the local fuel condition and heterogeneity, and can, in principle, be determined experimentally.

PARAGRASS treats the biased diffusion of gas atoms, as well as grain boundary bubbles, along the faces to the edges. Also included in PARAGRASS is a model for grain boundary separation driven by fission gas bubble overpressurization in a thermal transient. This model, described in more detail in Section (d) below, predicts the mode of transient mechanical response of the fuel ("ductile" or "brittle") and calculates the amount of separated grain boundary area per unit volume as well as the enhancement of gas release due to the availability of new pathways to the grain edges and the fuel exterior.

(4) Intergranular Phenomena on the Grain Edges

Once gas bubbles reach the grain edges, they can link up to form long-range interconnected tunnels that communicate with the fuel exterior. Experimental evidence[33] suggests that such tunnels stabilize under normal operating conditions above a certain critical edge swelling. Below this value, they sinter shut into isolated segments. The PARAGRASS approach is based on this evidence, with the difference that instead of having a threshold value of edge swelling, the probability of grain edge interconnection is modeled as a statistical function about this critical (experimentally determined) value of grain-edge swelling. The grain-edge-porosity

interlinkage fraction F is given by

$$F = \frac{1}{\sigma_E \sqrt{2\pi}} \int_{x=Bv_{crit}}^{\infty} \exp[-(x - Bv_{edge} - Bv_{por})^2 / 2\sigma_E^2]dx, \quad (49)$$

where σ_E = distribution width (a function of variations in structural parameters that depend on local fuel conditions and homogeneity),

Bv_{crit} = 0.05 (the value of grain edge swelling at which long-range interconnection would take place if the fuel microstructure and gas bubble morphology were homogeneous), and

Bv_{por} = 0.0 for $\rho \geq$ 92% theoretical density (TD)

= (92 - ρ)/100 for $\rho <$ 92% TD.

(5) PARAGRASS Model for Migration of Fission Products Up the Temperature Gradient

Based on FASTGRASS analysis, it has been concluded that the long-range migration of fission products up the temperature gradient provides a minor contribution to the overall behavior of the fission products in LWR fuel under most conditions of interest. By eliminating these models in PARAGRASS, it has been possible to decouple the calculation radially as well as axially. This feature provides for faster execution times for cases where more than one radial node is modeled.

c. Effect of Transient Heating on the Mobility of Fission Gas Bubbles

Analyses with the GRASS-SST code[34,35] for steady-state conditions, coupled with experimentally determined fission gas release during DEH tests, indicated that large quantities of gas are transported out of the UO_2 grains during transient heating. This release of fission gas from the grains is much greater than can be explained by empirical steady-state diffusivities measured under isothermal annealing conditions. Steady-state, in-reactor calculations are complicated by the interplay of bubble diffusivities and re-solution rate. The validity of using empirical steady-state diffusivities with much lower values than those predicted by a surface-diffusion mechanism is dependent on the validity of the re-solution parameter used in the calculations. The value of the re-solution parameter used in the

GRASS calculations yields a re-solution rate of ~5 x 10^{-5}/s for a fission rate of 10^{13} F/cm^{3}s^{-1}. This value is larger than that used in some models but still somewhat less than experimentally deduced values. In addition, analyses for transient-heating conditions indicate that GRASS-SST can account for the rapid diffusion of fission gas out of the UO_2 grains during DEH tests if the high-temperature bubble mobilities are enhanced as a result of an increased rate of atom attachment to and detachment from the bubble surface.

The physical basis behind this approach is as follows. During equilibrium conditions, the bubbles may be faceted, and the rate of motion of a faceted bubble is determined by the frequency of nucleation of steps instead of the time required for atoms to move from a step on one side of a bubble to a step on the other side. (That is, the atom attachment and detachment rates are slower than predicted by surface diffusion.) However, if the atom attachment and detachment rates increase during transient conditions, higher bubble diffusivities will result.

Since plastic deformation of UO_2 due to an overpressurized bubble is expected to result in a high density of dislocations around the bubble surface, the diffusivity of such a bubble would be expected to increase rapidly. In effect, bubble diffusion would depend more on the time required for atoms to move from a step on one side of a bubble to a step on the other side (i.e., surface diffusion) than on the frequency of nucleation of steps.

The PARAGRASS model for the diffusion of overpressurized fission-gas bubbles is characterized by the equation

$$D_i = \frac{8.1266 \times 10^{-10} \exp[(-108{,}000)/RT]}{(6784.74 r_i)(2.09 + 1.91\alpha_i)}, \tag{50}$$

where D_i = diffusivity of a bubble of radius r_i,

R = gas constant,

T = absolute temperature, and

$\alpha_i (\alpha_i \leq 1)$ = degree-of-one equilibrium in the lattice surrounding a bubble of radius r_i.

The larger α_i becomes, the farther the system departs from an equilibrium configuration. The expression used for α_i is given by

$$\alpha_i = 1.0 - \exp(-\tau_i^B/\tau_i^v) \quad . \tag{51}$$

In Eq. (51),

$$\tau_i^y = \frac{\sigma_y r_i T_1}{[3\gamma dT/dt]} \quad , \tag{52}$$

where τ_i^y = time required for a bubble with radius r_i to develop an excess pressure sufficient to generate an equivalent stress equal to the yield stress σ_y of the surrounding matrix,

T_1 = temperature at the beginning of the time interval,

γ = surface tension, and

dT/dt = heating rate.

The bubble relaxation time τ_i^B in Eq. (51) is given by

$$\tau_i^B(t) = \frac{r_i^2}{c_v^e D_v} \quad , \tag{53}$$

where c_v^e is the fractional equilibrium vacancy concentration, given by

$$C_v^e = \exp(-E_v^f/kT), \tag{54}$$

and D_v is the vacancy diffusion coefficient, given by

$$D_v = D_v^o \exp(-E_v^m/kT) \quad , \tag{55}$$

where E_v^f and E_v^m are the vacancy formation and migration energies, respectively, and D_v^o is a pre-exponential factor.

When $\alpha_i \to 0$, Eq. (50) approaches the expression[25] for bubble diffusivities based on isothermal measurements. When $\alpha_i \to 1$, Eq. (50) approaches the expression for bubble diffusivities based on the theory of surface diffusion. For intermediate values of α_i, Eq. (50) lies between those values given by the empirical expression (as a lower limit) and those

obtained from the theory of surface diffusion (as an upper limit). Equation (50) is unique in the sense that it relates the bubble diffusivities to the fuel yield stress, heating rate, and vacancy mobility, as well as to fuel temperature and bubble radius.

d. PARAGRASS Model for Determining Ductile/Brittle Fuel Response

The ability to determine whether microcracking will occur during a given thermal transient is an important element in the prediction of fuel temperatures and fission gas release. In principle, a "classical" mechanical treatment, involving the high-temperature stress/strain relationships of UO_2, could be used to study microcracking. However, this approach is very complex, and would require knowledge of the mechanical properties of UO_2, including strain rate effects, at high temperatures. Data in this area are sparse, and are almost nonexistent for temperatures in excess of 2400 K.

As a first approach to modeling ductile/brittle behavior of oxide fuels, the DiMelfi-Deitrich model[25,28] has been used in the PARAGRASS code. This model estimates the growth rate of a grain boundary bubble under the driving force of internal pressurization. The volume growth rates due to crack propagation and to diffusional processes are compared to determine the dominant mode of volume swelling. Knowledge of the mechanical properties of UO_2 is not required.

The underlying structure of the model can be summarized as follows: A fission gas bubble on a grain boundary can be viewed as a crack nucleus. It can be shown that such a crack will propagate unstably if the internal bubble pressure exceeds that required for bubble equilibrium, i.e., if

$$p > \frac{\gamma_s}{\rho} - \sigma \ , \tag{56}$$

where p = internal bubble pressure,

γ_s = fuel-gas surface energy,

ρ = bubble radius of curvature, and

σ = tensile stress normal to the boundary.

Furthermore, if a bubble, initially at equlibrium, is subjected to transient heating, the internal pressure will increase above the equilibrium value. Under these conditions, crack propagation will occur unless diffusional growth of the bubble occurs rapidly enough to maintain equilibrium conditions.

During most thermal transients, the initial mode of bubble growth will be crack propagation. The "crack-like" bubble may be able to retain its equilibrium shape by diffusional transport of material along the grain boundary. However, if the heating rate is sufficiently high, repressurization can take place. Thus, the competition between diffusional growth and crack growth determines whether bubbles tend to remain isolated or rapidly become part of an interconnected network of microcracks.

In the DiMelfi-Deitrich analysis, an attempt is made to predict the dominant mode of bubble growth by comparing the rates of volume swelling due to crack propagation and diffusional growth. In practice, this is done by comparing the instantaneous value of the grain boundary diffusion coefficient, D_i, with the minimum value needed to maintain the equilibrium bubble volume, D_g^{min}. (The calculation of D_g^{min} is discussed in detail in Ref. 28.)
If $D_i < D_g^{min}$, cracking dominates, and this behavior is termed "brittle".
If $D_i > D_g^{min}$, diffusional growth or "ductile" behavior dominates.

The minimum diffusion coefficient D_g^{min} is given by

$$wD_g^{min} = \frac{m(kT)^2}{\gamma_s} \frac{k\lambda A}{4HL\Omega(\Delta p)} , \qquad (57)$$

where w = grain boundary width,
m = average number of atoms per bubble arriving at the grain boundary,
k = Boltzmann's constant,
γ_s = surface energy of UO_2,
λ = average bubble spacing in the grain boundary,
A = instantaneous heating rate,
T = temperature,
H = geometric factor,
L = bubble length,

Ω = molecular volume of UO_2, and

Δp = pressure in excess of that for an equilibrium grain-boundary bubble.

In deriving Eq. (57), the ideal gas law and zero normal stresses on the grain boundary were assumed. (A conditional equation for D_g^{min} can be derived for the case of nonzero normal stresses on the grain boundary, e.g., see Ref. 28.)

The PARAGRASS code provides the gas-bubble input to Eq. (57) as a function of time (i.e., λ, L, m, Δp). We have some reservations about the quantitative aspects of DiMelfi-Deitrich analysis but use it here as an interim model since it does seem to address the real physical phenomena of importance.

3. PARAGRASS Model for Volatile Fission Product Release

a. FASTGRASS Models for VFP Release

As the noble gases play a major role in establishing the interconnection of escape routes from the interior to the exterior of the fuel, a realistic description of VFP release must a priori include a realistic description of fission gas release and swelling. The steady-state and transient gas release and swelling subroutine, FASTGRASS, has been modified[26] to include a mechanistic description of VFP behavior (I, Cs, CsI, Cs_2MoO_4, Cs_2UO_4). Phenomena modeled are the chemical reactions between the VFPs, VFP migration through the fuel, and VFP interaction with the noble gases. Calculations performed with FASTGRASS for the release of I, Cs, and CsI from LWR fuel during steady-state and severe-core-accident conditions are described in Ref. 26.

b. PARAGRASS Models for VFP Release

PARAGRASS contains a simple model of VFP release. This model is based on the more detailed VFP models contained in FASTGRASS. Sensitivity studies were carried out with the more elaborate FASTGRASS code, and estimates made regarding the correlation between the behavior of VFPs and noble gases.

For the purposes of PARAGRASS, the release of CsI and I were assumed to be summed together to yield an effective iodine release rate. PARAGRASS thus predicts releases of Cs and I. It is further assumed that the VFPs follow the pathways created by the noble gases to the fuel exterior. Hence, it is not unreasonable to expect correlation between noble gas release (which is calculated in great detail in PARAGRASS) and VFP release. The present PARAGRASS model for the release of I and Cs (irrespective of chemical form) assumes that the fractional release of the volatile species is the same as for the noble gases. The molar releases of the I and Cs are determined by incorporation of the effective I and Cs fission product yields. At present, this model is intended to be primarily qualitative. As more experience is gathered with the full-scale FASTGRASS-VFP analysis, the model will be refined.

4. PARAGRASS I/O Description

a. Organization of COMMON

Labeled COMMON consists of the following blocks:

/GRAS/	Contains all variably dimensioned arrays that depend on the values of MK, the number of radial rings, and MJ, the number of axial sections.
/IPNT/	Contains pointers to the latter arrays.
/PROG/	Contains constants that can be varied on data input.
/PARG/	Contains computed and input constants.
/INDX/	Contains integer constants and variables.
/WRKSPC/	Contains scratch memory that may be overwritten upon exit from the routine.

b. General Description of Routines

The PARAGRASS package consists of the following five routines:

FBC	Defines MK, the maximum number of radial rings, and MJ, the maximum number of axial sections to be used in a particular run; then calls DFDIM and GDRIVE.

DFDIM — Computes the pointers for the arrays in /GRAS/, then checks that sufficient memory has been allocated to this block.

GDRIVE — Serves as driver routine; reads in and prints the input data, defines various arrays from these data, and calls ZRDWR and GRASF. A flow chart for GDRIVE is shown in Fig. 32, and a description of the driver input is given in Table XI.

ZRDWR — Takes action as follows, depending on the value of IRSTAR, an argument in the calling list:*

IRSTAR < 0	Write restart dump on unit NTAP.
IRSTAR = 0	Initialize COMMON/GRAS/, /PROG/. Read in card set #3 to make changes in /PROG/ (the variables in /PROG/ are listed in Table XII). Compute program constants in COMMON/PARG/, /INDX/.
IRSTAR = 1	Read in restart dump from unit NTAP.
IRSTAR > 2	Read in card set #3 to make changes in /PROG/. Compute program constants in COMMON/PARG/, /INDX/.

GRASF — Serves as the main control program for the package and performs the basic model calculations (internal time steps, fuel swelling, gas release, etc.). The following input must be provided to GRASF:

For each annular region (K,J)

RS	Inner radius of region (cm)
TS	Temperature at RS (°C or K)
TK	Average temperature in region (K)
PRSO	Hydrostatic pressure in region (psi)
POROS	Fractional porosity in region
GRSIZ	Grain diameter in region (cm)
VLM	Volume of region
TGR	Temperature gradient
TFP	Flux depression/area
ALP	Fraction of grain boundary area per unit volume separated by microcracks

*Note: GDRIVE reads in IRSTAR; if IRSTAR is greater than zero, then the code first calls ZRDWR with IRSTAR=1, then calls it a second time with IRSTAR=2.

For each axial section (J)

POW Linear power (kW/ft)

Remaining parameters

DELT Time increment (s)

ITRAN Flag specifying either steady-state or transient mode

NPRINT Print control

MCRK Microcracking flag

NOPT Grain growth/grain boundary sweeping flag

NCRK Flag to signal user input of ALP

For each value of (K,J), GRASF first calculates the bubble radii by use of Harrison's extrapolated equation of state. It then computes the bubble diffusion coefficients, migration velocities, coalescence probabilities, gas-atom re-solution rates, and the diffusion rates of fission gas from the grain lattice to the grain faces, and from the grain faces to the grain edges. It also calculates the maximum size for bubbles pinned to structural defects. Further, GRASF calculates the coefficients YB(I) and YC(I) from the equation for the bubble-size density, Y(I), as a function of time. The remainder of the routine consists of a modified version of ANL-D2525-DDFSUB, a routine that solves the set of regular, linear, first-order differential equations for the bubble size distribution by Neville's method of extrapolation with polynomials.

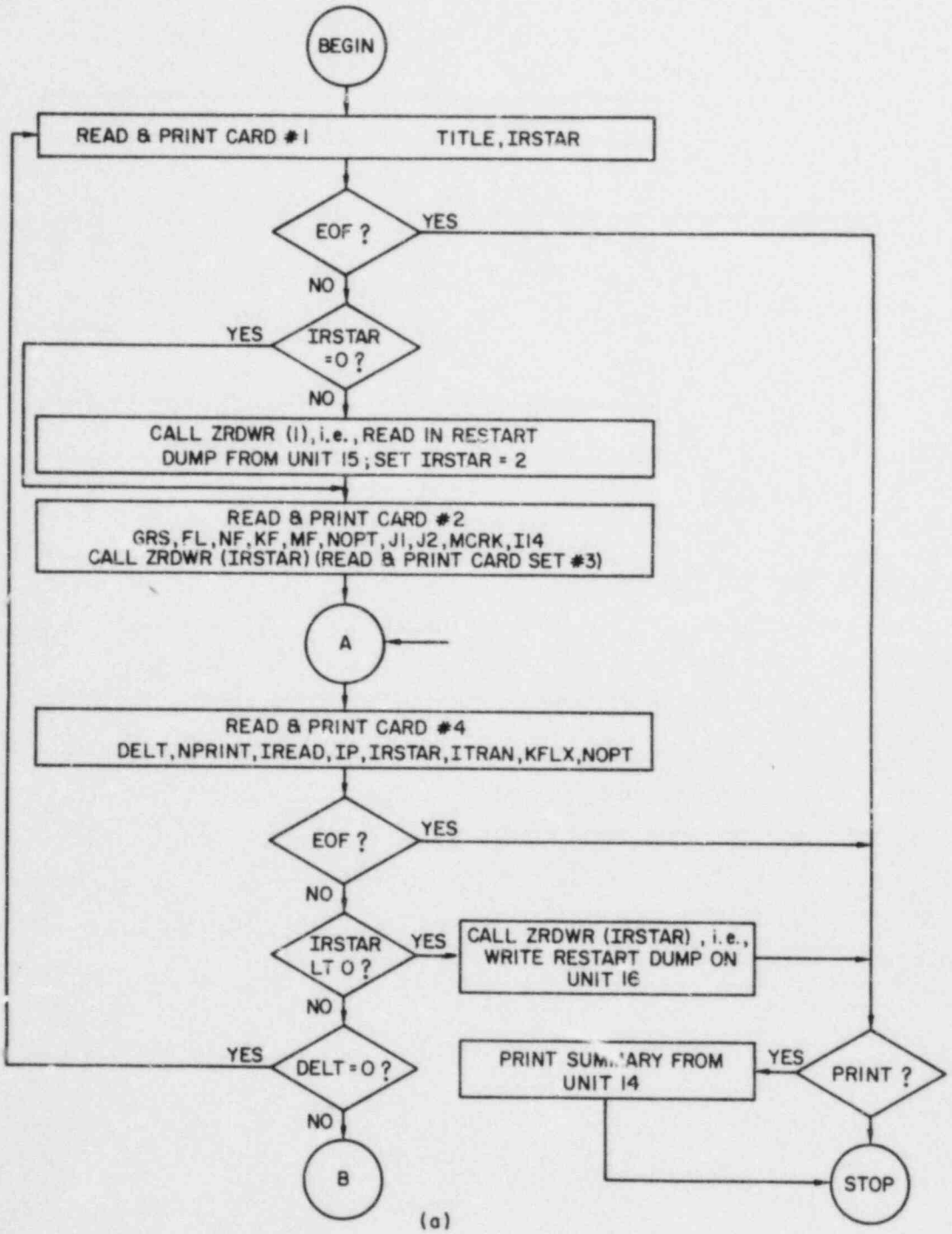

Fig. 32. GDRIVE Flow Chart. (a) Begin Through Step B; (b) Step B Through Step C; (c) Step C to End.

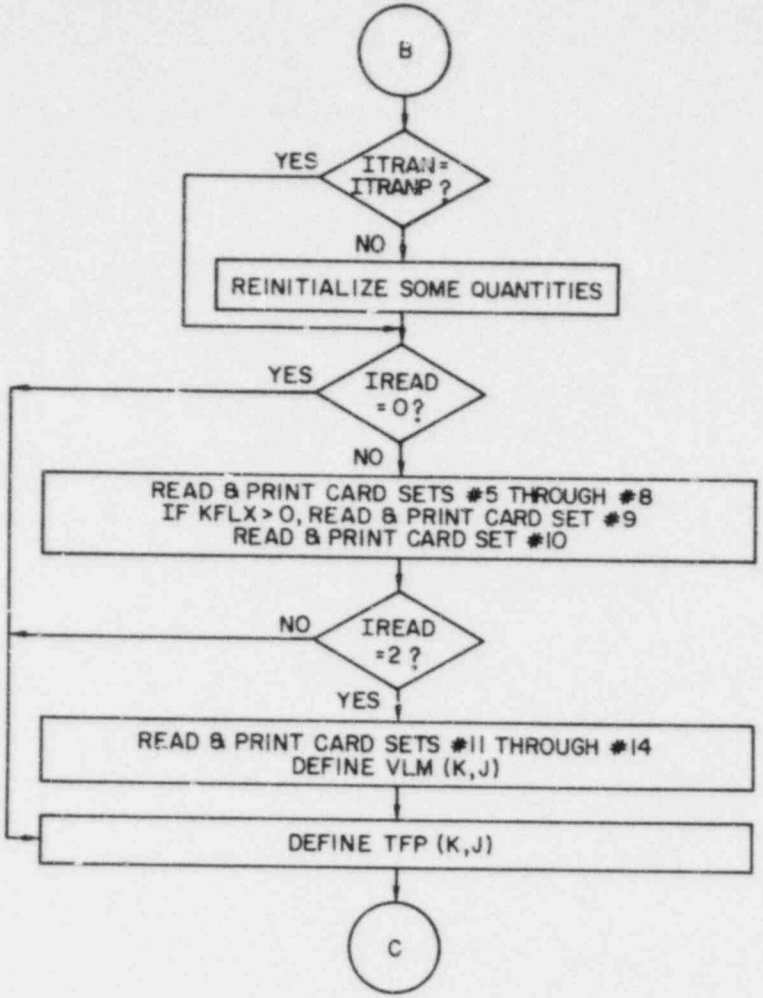

(b)

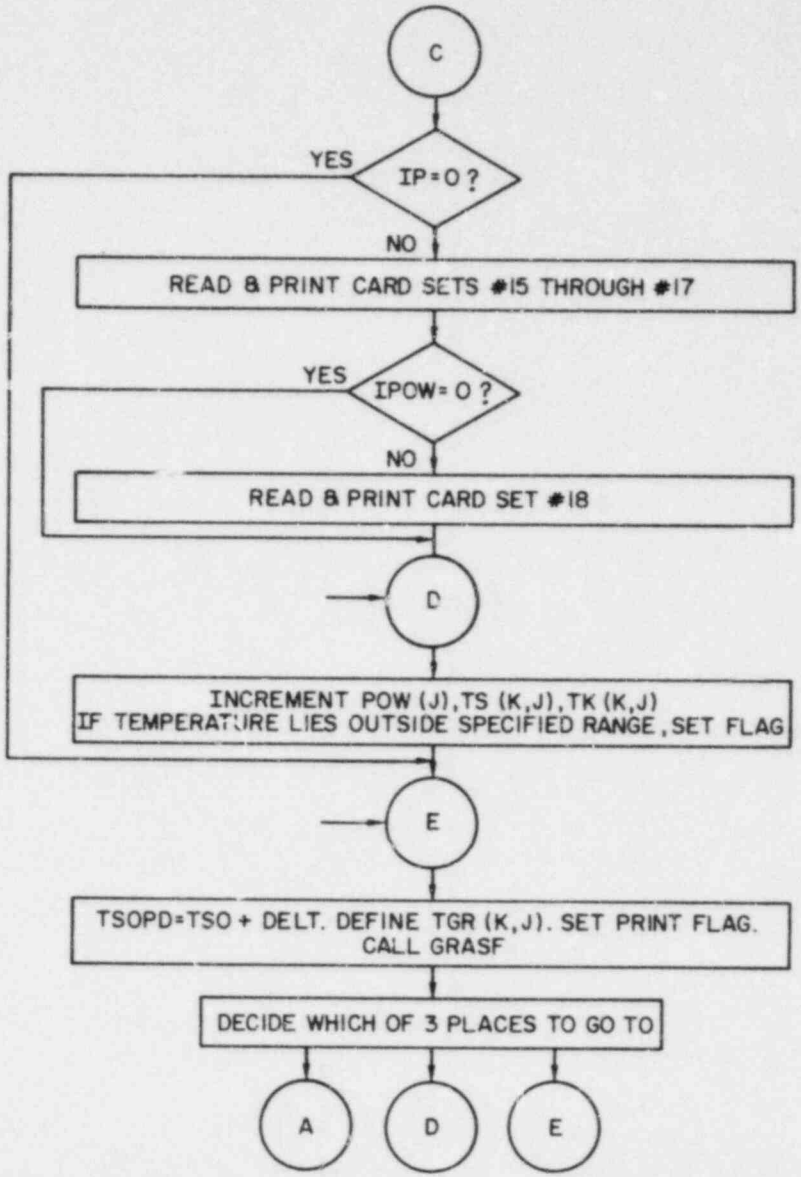

(c)

Fig. 32. (Contd.)

TABLE XI. Description of Driver Input

Card No.	Variable Name	Format	Description
1	ITLE	(19A4, 2X, I2)	ITLE (1-19) is a descriptive title
1	IRSTAR		IRSTAR = 0 for normal execution IRSTAR = 1 for problem restart from an external file
2	GRS	(2E10.4, 4I10, 4I5)	Initial amount of gas in fuel cladding
2	FL		Fuel rod length (cm)
2	NF		Total number of axial sections
2	KF		Total number of radial rings
2	IVPF		Unused
2	NOPT		NOPT = 0: No grain growth/grain boundary sweeping NOPT = 1: Integral grain growth law NOPT = 2: Differential grain growth law
2	J1		Calculation is done for axial fuel
2	J2		sections J1 through J2
2	MCRK		0: Invoke microcracking mode 1: Do not invoke microcracking mode
2	I14		Unused
3	I	(I5, E15.5, 2X, 2A4)	This card provides the capability of modifying any member in labeled
3	PROG(I)		COMMON/PROG/PROG(74). Last card of
3	LABEL		this set must have I = blank or zero
4	DELT	(E10.4, 6I10, 2I5)	Time step (s). If = 0, go to card #1
4	NPRINT		Printout option NPRINT = 1: No printout NPRINT > 1: Full printout

TABLE XI (Contd.)

Card No.	Variable Name	Format	Description
4	IREAD		IREAD = 0: No change in fuel properties and operating conditions for this time step IREAD = 1: Fuel operating conditions to be updated for this time step IREAD = 2: Fuel properties and operating conditions to be updated for this time step
4	IP		IP = 0: Do not input card sets 15-18 IP = 1: Input card sets 15-18 IP = 2: Input card sets 15-18, print card sets 16-18
4	IRSTAR		IRSTAR = 0: Do nothing IRSTAR < 0: Write restart dump on unit 16, stop IRSTAR > 2: Read card set #3, redefine constants.
4	ITRAN		ITRAN = 0: Steady-state mode ITRAN = 1: Transient mode
4	KFLX		Radial flux depression flag KFLX = 0: All FDP(K,J) = 1; do not include card #9 KFLX = 1: Include card set #9 to define (FDP(K,1),K = 1,KF). Code will internally set FDP(K,J) = FDP(K,1), J = 2, NF KFLX = 2: Include card set #9 to define J sets of (FDP(K,J),K = 1,KF)
4	NCRK		NCRK = 0: Do not read in card set #4A NCRK ≠ 0: Read in card set #4A

TABLE XI (Contd.)

Card No.	Variable Name	Format	Description
4	NOPT		NOPT = 0: No grain growth/grain boundary sweeping NOPT = 1: Integral grain growth law NOPT = 2, 3: Differential grain growth laws
4A	ALP(K,J)	(8E10.4)	Fraction of grain boundary area per unit volume separated by microcracks
If IREAD = 0 go to card #15			
5A-5S	TS(K,J)	(8E10.4)	Temperatures at boundaries of regions (K,J) (°C or K)
6A-6R	TK(K,J)	(8E10.4)	Average temperatures of regions (K,J) (K)
7A-7J	POW(J)	(8E10.4)	Linear power in axial sections (kW/ft)
8A-8R	PRSO(K,J)	(8E10.4)	Average hydrostatic pressure in regions (K,J) (psi)
9A-9N	FDP(K,J)	(8E10.4)	See KFLX on card #4
10	PLENP	(E10.4)	Plenum pressure (psi)
If IREAD =2 go to card #15			
11A-11R	RH(K,J)	(8E10.4)	Average fuel density in region (K,J) (g/cm^3) (not used in PARAGRASS, leave blank)
12A-12S	RS(K,J)	(8E10.4)	Radius of the boundary of region (K,J) (cm)
13A-13R	POROS(K,J)	(8E10.4)	Average fractional porosity in region (K,J)
14A-14R	GRSIZ(K,J)	(8E10.4)	Average grain diameter in region (K,J) (cm)
If IP = 0 go to card #4			

TABLE XI (Contd.)

Card No.	Variable Name	Format	Description
15	TMAX TDMIN TDMAX	(3E10.4, 4I10)	For IP = 1,2 the code will execute until total time $\geq$ TDMAX or the minimum fuel temperature TK (K,J) $\leq$ TDMIN
If IP = 0 go to card #4			
15	IPRINT JPRINT IWRITE		If NPRINT = JPRINT, printout for every IPRINT time step will be provided with NPRINT = IWRITE
	IPOW		IPOW = 0: Do not read in POW (J). IPOW = 1: Read in POW(J)
16	TD(K,J)	(8E10.4)	Temperatures TS(K,J) incremented by TD(K,J) during DELT
17	DPOW(J)	(8E10.4)	Power incremented by DPOW(J) during DELT
If IPOW = 0 go to card #4			
18	POW(J)	(8E10.4)	Linear power in axial section J (kW/ft)
			Repeat sequence starting with card #4.

TABLE XII. Dictionary of Variables in COMMON/PROG/

Index	Variable Name	Description
1-9	A(1-9)	Parameters in the calculation of the UO_2 yield strength
10	AADC1	Pre-exponential factor for gas atom diffusion coefficient (cm^2/s)
11	AADC2	Activation energy for gas atom diffusion (cal)
12	ACON	Parameter which relates grain boundary area per unit volume to the equivalent grain diameter
13	ASTAR	Fraction of areal coverage of grain face by bubbles required for channel formation
14	ATMVOL	Volume associated with one molecule of fuel
15	AVN	Avogadro's number
16-21	BADC1-6	Coefficients in the semi-empirical/ phenomenological expression for intragranular bubble diffusivities
22	BOLTZ	Boltzmann's constant
23	BVCRIT	Critical value of grain-edge swelling required for long-range tunnel interlinkage
24	CALCA	Proportionality constant between theoretical and actual grain boundary separation rate
25	CPOW	Converts linear power from kW/ft to W/cm
26	CRT	Relative error permitted in the integration
27	CR1	Convergence criterion in bubble radius computation
28	DELHV	Unused

TABLE XII (Contd.)

Index	Variable Name	Description
29	DVO	Pre-exponential factor in expression for lattice or grain-boundary vacancy diffusivity
30	DZERO	Pre-exponential factor in the expression for surface diffusion of UO_2
31	EV	Equal to the sum of migration and formation energies for vacancy diffusion
32	FAWGE	Average number of grain faces per grain
33-36	FGPF(1-4)	FGPF(1-3) are the number of noble gas atoms, iodine atoms and cesium atoms, respectively, produced per fission event. FGPF(4) is unused.
37	FN	Probability that two atoms which collide stick together to form a bubble nucleus
38	FPWS	Factor which determines the number of fissions/cm•s from the power in W/s
39-41	GBADC1-3	Coefficients in the semi-empirical/ phenomenological expression for intergranular bubble diffusivities
42	GBR	Multiplies RESCON to obtain effective irradiation-induced re-solution of gas atoms from grain boundary bubbles
43-44	G1-G2	Coefficients in the expression for UO_2 surface energy
45	PDSC	Converts hydrostatic stress from $in.^{-2}$ to $dynes/cm^2$
46	PTPL	Value of fabricated porosity above which this porosity contributes to PRF(K)
47	PZERO	Unused

TABLE XII (Contd.)

Index	Variable Name	Description
48	QS	Activation energy for surface diffusion (ergs/mole)
49	QSSTAR	Heat of transport for surface diffusion
50	QSURF	Activation energy (cal) for surface diffusion
51	REDIS	Average distance traveled by an atom ejected from a grain boundary bubble
52	RESCON	Re-solution constant
53	RG	Gas constant
54	RM	Constant which defines the geometric progression of bubble size ranges
55	SBCF	Width of distribution of grain-face channel formation probability
56	SIG	Unused
57	SIGPI	Width of distribution of grain edge porosity
58	THETA	Twice THETA is the dihedral equilibrium angle that a gas bubble makes with the grain boundary
59	WM1	Unused
60	WM2	Unused
61	XDL(1)	Control on time-step size as defined in the driver
62	XDL(2)	Control on time-step size as defined in the driver
63	XK	Parameter in the expression for the driving force on a bubble in a temperature gradient
64	XKP	Ratio of the thermal conductivity of a pore to the thermal conductivity of fuel

TABLE XII (Contd.)

Index	Variable Name	Description
65	XK1	Parameter in grain growth model
66	XK2	Parameter in grain growth model
67	XK3	Parameter in grain growth model
68	XRMPP	Power ramping criterion (kW/ft)
69	XRMPT	Temperature ramping criterion (K/s)

c. Integration of PARAGRASS into a Fuel Behavior Code; COMMON Blocks

The essence of integrating PARAGRASS into an existing Fuel Behavior Code (FBC) lies in removing the dummy FBC and the driver and supplying PARAGRASS with those quantities that the driver would normally provide. The following steps must be followed to integrate PARAGRASS into an FBC:

1. Remove dummy FBC, GDRIVE.
2. At time of initialization in FBC, place a call ZRDWR(0) to initialize PARAGRASS.
3. At time of run from restart in FBC, place a CALL ZRDWR(1) to read restart dump, and, if desired, a CALL ZRDWR(2) to make modifications in COMMON/PROG/.
4. Before entering the time-step loop, define any PARAGRASS quantities that remain fixed during that loop.
5. In the time-step loop, define PARAGRASS input parameters, and place a CALL GRASF to invoke gas release package.
6. At time of exit from FBC, provide facility to write a restart dump by a CALL ZRDWR(-1).

COMMON has been organized to facilitate code integration. Typically, block /WRKSPC/ is removed and its contents transferred to existing scratch memory that can be overwritten upon exit from subroutine GRASF.

d. Output Description

A sample PARAGRASS computer output is provided in Fig. 33. The parts of the output that appear between asterisks originate in the driver routine GDRIVE. When PARAGRASS is integrated into an FBC, GDRIVE is removed. Hence, these parts of the output will not appear in the PARAGRASS output from an integrated version of the code. Further, the output shown here is for fuel with one axial section (J=1) and one radial section (K=1).

Section A of the output illustrated in Fig. 33 prints the information in cards #1 - #3 as read in by GDRIVE. When GDRIVE is removed on integration of PARAGRASS into an FBC, this section will not appear.

Section B reproduces input as read in by GDRIVE in cards #4-17. This section of the output will also not appear when GDRIVE is removed.

Section C of the output should be understood in three stages. Stage C_1 refers to output quantities that are specific to a particular radial section and a particular axial section (here, K = 1 and J = 1). Stage C_2 refers to quantities that are averaged over all the radial sections for a particular axial section (J = 1 in the sample shown). Stage C_3 refers to output variables that are averaged for the whole fuel pin. The output variables are defined as follows:

Stage C_1

J	Axial section
K	Radial section
RS (K,J), RS (K + 1, J)	Radii of the two boundaries of region (K,J) (cm)

```
FTS.DATAT.DATA-1750K, .000C/CM, 10 UM AND 3.0 AT. BU                    IRSTAR= 0

A  GRT,FL= 0.0          1.000000D+00
   NF,KF,IVFP,NOPT,J1,J2,MCRK,I14=    1    1    0    0    0    0    0    1
   PROG(26)=    2.000000D-04

**********************************************************************************************
   DELT= 1.0000D-03     NPRINT,IREAD,IP,IRSTAR,ITRAN,KFLX,NCRK,NOPT=    4    2    0    0    0    0    0    0

   TS(K,J)=          1.5145D+03     1.5145D+03
   TK(K,J)=          1.7500D+03
B  FOH(J)=           1.0000D+00
   PRSO(K,J)=        1.0000D+03
   PLENP=            1.0000D+03
   RS(K,J)=          1.7825D-01     2.5329D-01
   POROS(K,J)=       7.4750D-02
   GRSIZ(K,J)=       1.0000D-03
**********************************************************************************************

                                  ********** GRASS OUTPUT **********

                                          TIME=  0.100000000D-02

   ------ AXIAL SECTION=  1 RADIAL SECTION=  1

   RS(K,J)=  1.7825500-01 RS(K+1,J)=  2.5329500-01 TS(K,J)=  1.5145200+03 TS(K+1,J)=1.5145200+03 POROS =  7.4750000-02
   DELT   =  1.0000000-03 VOLUME   =  1.0172630-01 PRFOLD =  0.0

   TKI= 1.7500000+03 TGRAD= 0.0        DTDT= 0.0        TFPV= 9.9980D+12 GSIN= 3.0994D+12 GRD= 1.0000D-03 DCIE= 1.9996D-17

   LATTICE SIZE CLASSES
         SAVG          RAD        BDSURF       BVSURF       BDLTCE       BDATOM       BVATOM
    1.00000D+00  2.4037D-08  3.6458D-08  0.0          8.9150D-16  8.9158D-16  0.0
    2.00000D+00  3.0443D-08  1.4169D-08  0.0          1.3210D-15  1.3210D-15  0.0
   FACE SIZE CLASS
C1  2.00000D+00  3.0443D-08  1.4169D-08  0.0
                 2.1367D-08
   EDGE SIZE CLASS
    2.00000D+00  3.0443D-08  1.4169D-08  0.0
                 2.1367D-08

   TAU=  1.0000000-03 H=  1.0000000-03 HNXT=  1.5000000-03 HH=  1.0000000+02

   DISTRIBUTIONS FOLLOW (NUMBER/CM**3)
   REGION 1  LTCE  3.0994D+09  3.4494D-13  FACE  3.1097D-01  EDGE  0.0

   FLUX(I)=  6.2194D+02  0.0          0.0          0.0                    PBKGBY(I)=  0.0          0.0          GBS=  0.0

    J  K          RPIN          BVKJ          RGK          PDSG
    1  1  2.2258750-22  1.8030860-13  5.2338830-16  1.0000000+03

   GSGEN= 5.2338766D-16 LTCEFR=1.0000000D+00 TKI=   1.7500000D+03 BVSL=  1.8030860D-13 EGRE=  0.0          ALPHA= 0.0
   GOUTK= 0.0           FACEFR=2.0066510D-10 TKIO=  1.7500000D+03 BVSF=  4.4051728D-24 EFRF=  0.0          ACAEN= 0.0
   FGRK=  0.0           EDGEFR=0.0           GKOUT= 0.0           BVSE=  0.0           PRC=   4.7790352D-02 BETAB= 0.0

C2 AXIAL TOTALS   J = 1
   BVS=   1.8030860D-13 RGJ=   5.2338832D-16 GSRJ=  0.0          RGGL=  1.0000000D+00 RGGF=  2.0066535D-10 RGGE=  0.0
   FGRJ=  0.0

   ROD TOTALS
C3 FGRT=  0.0           RGT=   5.2338832D-16 GTOUT= 0.0          GRFT=  0.0          GGT=   5.2338766D-16 ERR=   1.2680196D-06
   RETI=  1.8571820D-17 RETC=  3.1774695D-16 OUTI=  0.0          OUTC=  0.0

                          ********** END OF GRASS OUTPUT FOR THIS TIME STEP **********
```

Fig. 33. Sample PARAGRASS Output. See text for details.

Stage C_1 (Contd.)

TS (K,J), TS (K+1,J)	Temperatures of the two boundaries of region (K,J) (K)
POROS	Average fractional porosity in region (K,J)
DELT	Time step (s)
VOLUME	Volume of the region (K,J) (cm^3)
PRFOLD	Pore interlinkage probability fraction during the previous time step
TKI	Average temperature in region (K,J) (K)
TGRAD	Temperature gradient in region (K,J) (K/cm)
DTDT	Heating rate in region (K,J) (K/s)
TFPV	Fission rate per unit volume in region (K,J)
GSIN	Fission gas generation rate ($atoms/s/cm^3$)
GRD	Grain size (cm)
DCIE	Fission-enhanced diffusion coefficient (cm^2/s)
SAVG	Average number of gas atoms/bubble
RAD	Bubble radii (cm)
BDSURF	Diffusion coefficient for bubble movement based on surface diffusion (cm^2/s)
BVSURF	Bubble velocity based on surface diffusion (cm/s)

Stage C_1 (Contd.)

BDLTCE	Intragranular diffusion coefficient of atoms and bubbles used in the calculations (cm/s)
BDATOM	Semi-empirical/phenomenological diffusion coefficient (cm^2/s)
BVATOM	Bubble velocity based on BDATOM (cm/s)
TAU	Time for which integration has been completed (s)
H	Current time increment (s)
HNXT	Suggested value of time increment (s)
HM	Upper limit on the value of an integration step (s)
LTCE	Gas atom and gas bubble density in lattice ($1/cm^3$)
FACE, EDGE	Gas bubble density on the grain faces and edges, respectively ($1/cm^3$)
FLUX, PBKGBY	Rates of fission gas migration from within the UO_2 fuel to the grain boundaries
GBS	Rate of intergranular gas release due to grain boundary sweeping mechanism
RPIN	Fraction of retained intragranular fission gas that resides in bubbles
BVKG	Total strain due to gas bubbles
RGK	Amount of retained gas in region (K,J) (moles)
PRSG	PRSO(K,J) or PLENP, whichever is greater
GSGEN	Amount of gas generated (moles)

Stage C_1 (Contd.)

LTCEFR	Fraction of retained gas that resides in the lattice
TKI	Average fuel temperature (K)
BVSL	Fractional gas-bubble strain due to bubbles trapped in the lattice
EGRE	Rate of gas migration from grain faces to edges due to grain face channel formation
ALPHA	Fractional coverage of grain boundary area per unit volume by microcracks
GOUTK	Amount of fission gas retained (moles)
FACEFR	Fraction of retained gas that resides on the faces
TKIO	Previous value of TKI (K)
BVSF	Fractional gas-bubble strain owing to bubbles trapped on grain faces
EPRF	Number of gas atoms released owing to increased edge-tunnel interconnection
ACAEN	Separated grain boundary area per unit volume (cm^{-1})
FGRK	Fractional gas release from section (J,K)
EDGEFR	Fraction of retained gas that resides on the edges
GKOUT	Total gas release from section (J,K) during present time step
BVSE	Fractional gas-bubble strain due to bubbles trapped on grain edges
PRF	Probability of gas channel interlinkage

Stage C_1 (Contd.)

BETAB	Intragranular bubble nonequilibrium parameter

Stage C_2

J	Axial section
BVS	Average swelling strain in axial section J
RGJ	Amount of total generated gas that is retained in the fuel (moles)
GSRJ	Amount of gas released from axial section J (moles)
RGGL, RGGF, RGGE	Fraction of total gas generated that is retained in the fuel lattice, on the faces, and on the edges, respectively, for axial section J
FGRJ	Fractional gas release from axial section J

Stage C_3

FGRT	Total fractional gas release
RGT	Total retained gas (moles)
GTOUT	Gas released during time step (moles)
GRFT	Total amount of gas released (moles)
GGT	Total gas generated (moles)
ERR	Error defined as [GGT - (FGR + RETG)]/(GGT)
RETI	Amount of total generated iodine that is retained in the fuel (moles)

Stage C_3 (Contd.)

RETC	Amount of total generated cesium that is retained in the fuel (moles)
OUTI	Released iodine (moles)
OUTC	Released cesium (moles)

If there are several radial and axial sections, the average output variable values for each radial section in every axial section appear in Stage C_1 of the output, followed by average values for each axial section in Stage C_2, and finally the values pertaining to the whole fuel pin in Stage C_3.

5. Sample Problem and Results

Results from a sample problem are provided in Figs. 34 and 35 to enable the user to acquire a feel for PARAGRASS execution. The fuel is divided into one axial section and one radial section. The irradiation history for the sample problem is as follows: 1 cm of a UO_2 fuel rod with an outside radius of 0.25329 cm and an inside radius of 0.17825 cm is irradiated at a fission rate of $\sim 10^{13}$ fissions/cm^3/s and a constant temperature of 1750 K to a maximum burnup of 3 at. % (~30,000 MWd/MT). The results of the steady-state irradiation are shown in Fig. 34. The steady-state irradiation is followed by a transient temperature ramp of 1 K/s to a maximum temperature of 3123 K. The results of the transient simulation are shown in Fig. 35. A summary printout, provided by logical unit 14, appears at the end of the run (Fig. 35). The parameters have been defined previously. The printout gives the title first, followed by sets of output for each time that output was requested. Each set of output consists of all axial results followed by rod total results.

It should be noted that the time-step size (DELT) read in by the driver (GDRIVE) in the second card #4 (and printed out in the section between asterisks) does not necessarily coincide with the time step actually used (appearing after J = 1, K = 1). This cutting of the time-step size has been

done by subroutine GRASF, which has certain internal criteria for time step selection.

According to the results at the end of this simulation (steady-state + transient), the fractional release of noble gas (FGRT) is 65.7%. In this version of PARAGRASS, the fractional release of iodine and cesium is assumed to be the same as for the noble gases, and is not printed out separately. The actual molar releases of all three species (OUTG, OUTI, and OUTC) are also printed. Iodine and cesium molar releases (OUTI and OUTC) are scaled to reflect the effective fission product yield fractions of these species.

The grain boundary separation in units of grain boundary area per unit volume of fuel is ACAEN = 1106.9 cm^2/cm^3, and the fraction of grain boundary area per unit volume separated by microcracks is ALPHA = 0.233.

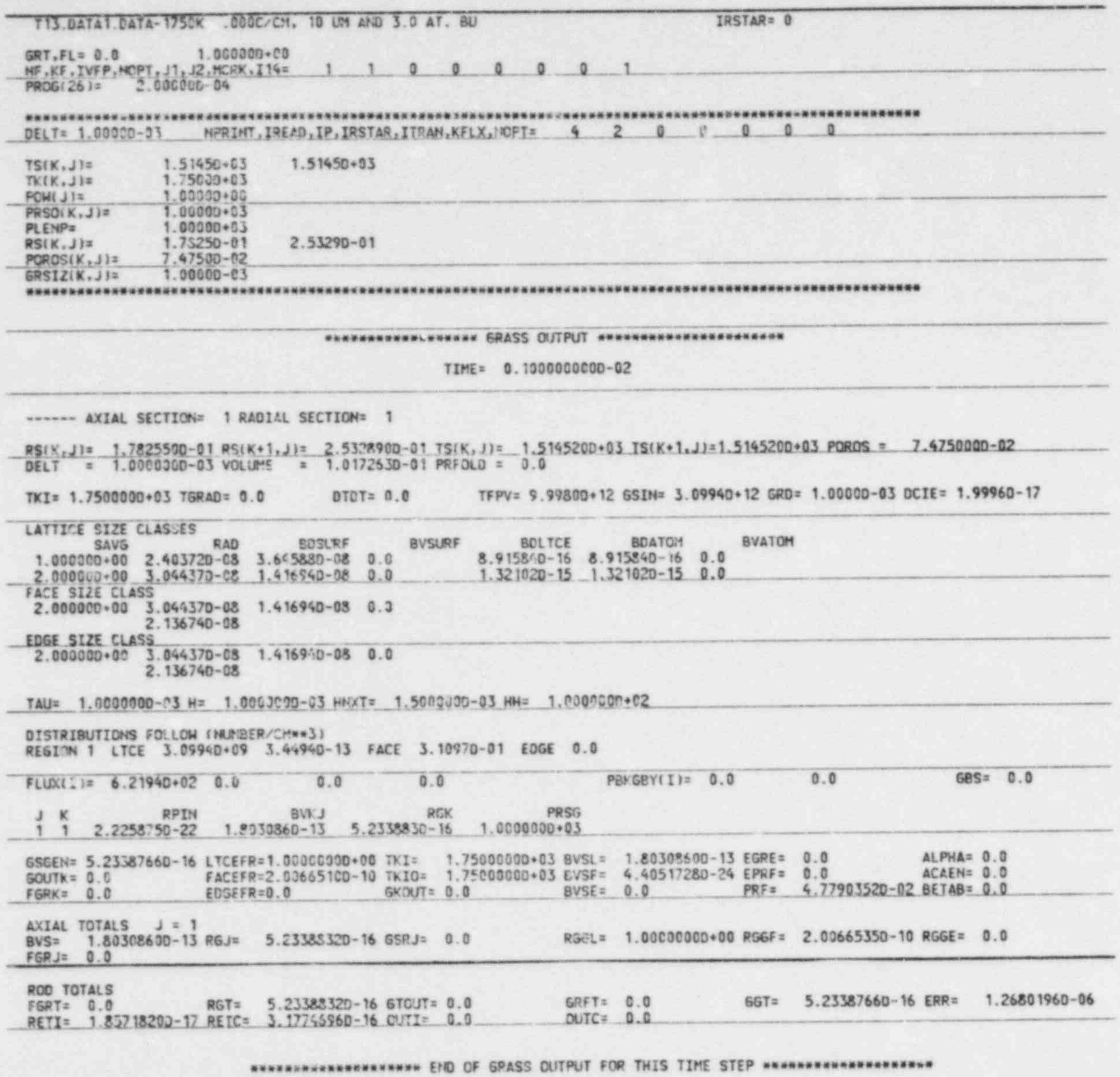

```
 T13.DATA1.DATA-1750K  .000C/CM, 10 UM AND 3.0 AT. BU                        IRSTAR= 0

 GRT,FL= 0.0          1.000000D+00
 NF,KF,IVFP,NOPT,J1,J2,MCRK,I14=    1    1    0    0    0    0    0    1
 PROG(26)=     2.000000D-04

 *****************************************************************************************
 DELT= 1.00000D-03      NPRINT,IREAD,IP,IRSTAR,ITRAN,KFLX,NOPT=    4    2    0    0    0    0    0

 TS(K,J)=          1.51450+03      1.51450+03
 TK(K,J)=          1.75000+03
 POW(J)=           1.00000+00
 PRSO(K,J)=        1.00000+03
 PLENP=            1.00000+03
 RS(K,J)=          1.75250-01      2.53290-01
 POROS(K,J)=       7.47500-02
 GRSIZ(K,J)=       1.00000-03
 *****************************************************************************************


                                   ********************* GRASS OUTPUT *********************

                                              TIME=  0.1000000000D-02


 ------ AXIAL SECTION=  1 RADIAL SECTION=  1

 RS(K,J)=  1.7825500-01 RS(K+1,J)=  2.5328900-01 TS(K,J)=  1.5145200+03 TS(K+1,J)=1.5145200+03 POROS =   7.4750000-02
 DELT   =  1.0000000-03 VOLUME    =  1.0172630-01 PRFOLD =  0.0

 TKI= 1.7500000+03 TGRAD= 0.0          DTDT= 0.0          TFPV= 9.99800+12 GSIN= 3.09940+12 GRD= 1.00000-03 DCIE= 1.99960-17

 LATTICE SIZE CLASSES
       SAVG          RAD        BDSURF          BVSURF        BDLTCE        BDATOM          BVATOM
  1.000000+00  2.403720-08  3.665880-08  0.0                8.915840-16  8.915840-16  0.0
  2.000000+00  3.044370-08  1.416940-08  0.0                1.321020-15  1.321020-15  0.0
 FACE SIZE CLASS
  2.000000+00  3.044370-08  1.416940-08  0.3
               2.136740-08
 EDGE SIZE CLASS
  2.000000+00  3.044370-08  1.416940-08  0.0
               2.136740-08

 TAU=  1.0000000-03 H=  1.0000000-03 HNXT=  1.5000000-03 HH=  1.0000000+02

 DISTRIBUTIONS FOLLOW (NUMBER/CM**3)
 REGION 1  LTCE  3.09940+09  3.44940-13  FACE  3.10970-01  EDGE  0.0

 FLUX(I)=  6.21940+02  0.0           0.0           0.0                    PBKGBY(I)=  0.0           0.0               GBS=  0.0

  J  K          RPIN            BVKJ            RGK             PRSG
  1  1   2.2258750-22   1.8030860-13   5.2338830-16   1.0000000+03

 GSGEN= 5.23387660-16 LTCEFR=1.00000000+00 TKI=    1.75000000+03 BVSL=  1.80308600-13 EGRE=  0.0              ALPHA= 0.0
 GOUTK= 0.0           FACEFR=2.00665100-10 TKIO=   1.75000000+03 EVSF=  4.40517280-24 EPRF=  0.0              ACAEN= 0.0
 FGRK=  0.0           EDGEFR=0.0           GKOUT= 0.0            BVSE=  0.0           PRF=   4.77903520-02 BETAB= 0.0

 AXIAL TOTALS   J = 1
 BVS=   1.80308600-13 RGJ=   5.23388320-16 GSRJ=  0.0            RGEL=  1.00000000+00 RGGF=  2.00665350-10 RGGE=  0.0
 FGRJ=  0.0

 ROD TOTALS
 FGRT=  0.0           RGT=   5.23388320-16 GTOUT= 0.0            GRFT=  0.0            GGT=   5.23387660-16 ERR=   1.26801960-06
 RETI=  1.85718200-17 REIC=  3.17746960-16 OUTI=  0.0            OUTC=  0.0

                      ******************** END OF GRASS OUTPUT FOR THIS TIME STEP ********************
```

Fig. 34. Execution of the Steady-State Portion of a Sample Problem with PARAGRASS. See text for details.

```
DELT= 7.5440D+03     NPRINT,IREAD,IP,IRSTAR,ITRAN,KFLX,NOPT=    1    0    1    0    0    0    0

TMAX,TDMIN,TDMAX=  9.0528D+05  2.0000D+02  3.1230D+03     IPRINT,JPRINT,IWRITE,IPOW=  120    1    4    0
TD(K,J)=        0.0            0.0
DPOW(J)=        0.0
```

********** GRASS OUTPUT **********

TIME= 0.9052800010+06

------ AXIAL SECTION= 1 RADIAL SECTION= 1

```
RS(K,J)=  1.7825500-01 RS(K+1,J)=  2.5328900-01 TS(K,J)=  1.5145200+03 TS(K+1,J)=1.5145200+03 POROS =  7.4750000-02
DELT   =  7.5440000+03 VOLUME    =  1.0172630-01 PKFOLD =  4.7790350-02

TKI= 1.7500000+03 TGRAD= 0.0        DTDT= 0.0        TFPV= 9.9980D+12 GSIN= 3.0994D+12 GRD= 1.0000D-03 DCIE= 1.9996D-17

LATTICE SIZE CLASSES
        SAVG          RAD          BOSURF       BVSURF       BOLTCE       BOATOM       BVATOM
 1.0000D+00  2.4037D-03  3.6458D-03  0.0          8.9150D-16  8.9150D-16  0.0
 1.4138D+01  5.9732D-08  9.5291D-10  0.0          3.2204D-16  3.2204D-16  0.0
FACE SIZE CLASS
 2.4080D+05  2.7770D-06  2.0165D-15  0.0
             7.4142D-06
EDGE SIZE CLASS
 2.0000D+00  3.0443D-08  1.4169D-08  0.0
             2.1367D-08

TAU=  7.5440000+03 H=  3.7720000+06 HNXT=  5.6580000+03 HH=  5.6580000+03

DISTRIBUTIONS FOLLOW (NUMBER/C.M**3)
REGION 1  LTCE  2.2133D+18  2.7655D+16  FACE  8.2258D+11  EDGE  0.0

FLUX(I)=  3.7200D+11  1.6929D+09  0.0          0.0                    PBKGBY(I)=  0.0          0.0              GBS=  0.0

 J  K          RPIN           BVKJ           PCK            PRSG
 1  1   1.5079430-01   6.4032400-04   4.7381190-07   1.0000000+03

GSGEN= 4.7381238D-07 LTCEFR=9.2889694D-01 TKI=   1.7500000D+03 BVSL=  1.5350954D-04 EGRE=  0.0          ALPHA= 0.0
GOUTK= 0.0           FALEFR=7.1103157D-02 TKIO=  1.7500000D+03 BVSF=  4.8681468D-04 EPRF=  0.0          ACAEN= 0.0
FGRK=  0.0           EDGEFR=0.0           GKOUT= 0.0           BVSE=  0.0           PRF=   4.7790352D-02 BETAB= 0.0

AXIAL TOTALS  J = 1
BVS=   6.4032402D-04 RGJ=   4.7381192D-07 GSRJ=  0.0          RGGL=  9.2889594D-01 RGGF=  7.1103088D-02 RGGE=  0.0
FGRJ=  0.0

ROD TOTALS
FGRT=  0.0           RGT=   4.7381192D-07 GTOUT= 0.0          GRFT=  0.0           GGT=   4.7381238D-07 ERR=   9.7017154D-07
RETI=  1.6812697D-08 RETC=  2.8764997D-07 OUTI=  0.0          OUTC=  0.0
```

********** END OF GRASS OUTPUT FOR THIS TIME STEP **********

Fig. 34 (cont.)

```
**********************************************************************************************************
DELT= 3.0176D+04     NPR...T,IREAD,IP,IRSTAR,ITRAN,KFLX,NOPT=    1    0    1    0    0    0    0

TMAX,TDMIN,TDMAX= 6.7876D+07  2.0000D+02  3.1230D+03     IPRINT,JPRINT,IWRITE,IPOW=  444    1    4    0
TD(K,J)=        0.0           0.0
DPOW(J)=        0.0
**********************************************************************************************************

                              ********** GRASS OUTPUT **********

                                    TIME= 0.143034240D+08

------ AXIAL SECTION=  1 RADIAL SECTION=  1

RS(K,J)= 1.782550D-01 RS(K+1,J)= 2.532890D-01 TS(K,J)= 1.514520D+03 TS(K+1,J)=1.514520D+03 PORDS =  7.475000D-02
DELT   = 3.017600D+04 VOLUME   = 1.017263D-01 PRFOLD =  5.339799D-01

TKI= 1.750000D+03 TGRAD= 0.0        DTDT= 0.0        TFPV= 9.9980D+12 GSIN= 3.0994D+12 GRD= 1.0000D-03 DCIE= 1.9996D-17

LATTICE SIZE CLASSES
      SAVG          RAD        BDSURF       BVSURF       BDLTCE       BDATOM       BVATOM
 1.0000D+00  2.4037D-08  3.6458D-03  0.0          8.9153D-16  8.9158D-16  0.0
 2.4623D+02  1.6650D-07  1.5837D-11  0.0          3.7798D-17  3.7798D-17  0.0
FACE SIZE CLASS
 1.7484D+06  6.7447D-06  5.8813D-18  0.0
             1.9978D-05
EDGE SIZE CLASS
 2.3173D+06  7.6320D-06  3.5874D-18  0.0
             2.3000D-05

TAU= 3.017600D+04 H= 1.5088D+04 HNXT= 2.2632D+04 HH= 2.2632D+04

DISTRIBUTIONS FOLLOW (NUMBER/CM**3)
REGION 1  LTCE  2.2141D+19  1.8964D+16  FACE  1.5282D+12  EDGE  2.9812D+12

FLUX(I)= 1.7256D+12  8.5391D+07  0.0        0.0                PBKGBY(I)= 0.0        0.0            GBS= 0.0

 J  K          RPIN          BVKJ          RGK          PRSG
 1  1  1.7428560-01   7.2020550-02  6.1460060-06  1.0000000+03

GSGEN= 7.4862356D-06 LTCEFR=7.3676985D-01 TKI=   1.7500000D+03 BVSL=  1.6547431D-03 EGRE=  6.5071102D-07 ALPHA= 0.0
GOUTK= 1.3402229D-06 FACEFR=7.3415982D-02 TKIO=  1.7500000D+03 BVSF=  1.7695562D-02 EPRF=  7.0362434D-03 ACAEN= 0.0
FGRK=  1.7902494D-01 EDGEFR=1.8981417D-01 GKOUT= 3.6057708D-09 BVSE=  5.2670244D-02 PRF=   5.3447462D-01 BETAB= 0.0

AXIAL TOTALS   J = 1
BVS=   7.2020550D-02 RGJ=   6.1460060D-06 GSRJ=  7.2086700D-09 RGGL=  6.0486902D-01 RGGF=  6.0272625D-02 RGGE=  1.5583253D-01
FGRJ=  1.7902494D-01

ROD TOTALS
FGRT=  1.7902494D-01 RGT=   6.1460060D-06 GTOUT= 7.2086700D-09 GRFT=  1.3402229D-06 GGT=   7.4862356D-06 ERR=   8.8620240D-07
RETI=  2.1808432D-07 RETC=  3.7312245D-06 OUTI=  4.7556297D-08 OUTC=  8.1364500D-07

********** END OF GRASS OUTPUT FOR THIS TIME STEP **********
```

Fig. 34 (cont.)

```
********** GRASS OUTPUT **********

TIME= 0.2770156800+08

------ AXIAL SECTION= 1 RADIAL SECTION= 1

RS(K,J)= 1.7825500-01 RS(K+1,J)= 2.5328900-01 TS(K,J)= 1.5145200+03 TS(K+1,J)=1.5145200+03 POROS = 7.4750000-02
DELT = 3.0176000+04 VOLUME = 1.0172630-01 PRFOLD = 7.6820170-01

TKI= 1.7500000+03 TGRAD= 0.0 DTDT= 0.0 TFPV= 9.9980D+12 GSIN= 3.0994D+12 GRD= 1.0000D-03 DCIE= 1.9996D-17

LATTICE SIZE CLASSES
      SAVG          RAD          BDSURF       BVSURF       BDLTCE       BDATOM       BVATOM
 1.0000D+00  2.4037D-08  3.6458D-08  0.0          8.9158D-16  8.9158D-16  0.0
 3.9953D+02  1.9946D-07  7.6893D-12  0.0          2.5905D-17  2.5905D-17  0.0
FACE SIZE CLASS
 1.7484D+06  6.7447D-06  5.8813D-18  0.0
             1.9978D-05
EDGE SIZE CLASS
 2.3173D+06  7.6320D-06  3.5874D-18  0.0
             2.3000D-05

TAU= 3.0176000+04 H= 1.5088000+04 HNXT= 2.2632000+04 HH= 2.2632000+04

DISTRIBUTIONS FOLLOW (NUMBER/CM**3)
REGION 1 LTCE 3.1011D+19 2.8464D+16 FACE 1.5337D+12 EDGE 4.0769D+12

FLUX(I)= 2.0720D+12 7.9297D+07 0.0 0.0 PBKGBY(I)= 0.0 0.0 GBS= 0.0

 J  K          RPIN          BVKJ          RGK          PRSG
 1  1  2.6838860-01  9.2538320-02  9.2060220-06  1.0000000+03

GSGEN= 1.4498659D-05 LTCEFR=7.7751355D-01 TKI= 1.7500000D+03 BVSL= 2.7502250D-03 EGRE= 7.8172871D-07 ALPHA= 0.0
GOUTK= 5.2926093D-06 FACEFR=4.9190585D-02 TKIO= 1.7500000D+03 BVSF= 1.7759665D-02 EPRF= 3.9060494D-08 ACAEN= 0.0
FGRK= 3.6504131D-01 EDGEFR=1.7329586D-01 GKOUT= 5.0440029D-09 BVSE= 7.2028427D-02 PRF= 7.6833831D-01 BETAB= 0.0

AXIAL TOTALS J = 1
BVS= 9.2538317D-02 RGJ= 9.2060221D-06 GSRJ= 1.0087009D-08 RGGL= 4.9368752D-01 RGGF= 3.1233897D-02 RGGE= 1.1003539D-01
FGRJ= 3.6504131D-01

ROD TOTALS
FGRT= 3.6504131D-01 RGT= 9.2060221D-06 GTOUT= 1.0087009D-08 GRFT= 5.2926093D-06 GGT= 1.4498659D-05 ERR= 1.8846826D-06
RETI= 3.2666627D-07 RETC= 5.5889629D-06 OUTI= 1.8780227D-07 OUTC= 3.2131261D-06

********** END OF GRASS OUTPUT FOR THIS TIME STEP **********
```

Fig. 34 (cont.)

```
********** GRASS OUTPUT **********

                                        TIME=  0.410997120D+08

------ AXIAL SECTION=  1 RADIAL SECTION=  1

RS(K,J)=  1.782550D-01 RS(K+1,J)=  2.532890D-01 TS(K,J)=  1.514520D+03 TS(K+1,J)=1.514520D+03 PORCS =   7.475000D-02
DELT   =  3.017600D+04 VOLUME   =  1.017263D-01 PRFOLD =  8.397830D-01

TKI= 1.750000D+03 TGRAD= 0.0        DTDT= 0.0        TFPV= 9.9980D+12 GSIN= 3.0994D+12 GRD= 1.0000D-03 DCIE= 1.9996D-17

LATTICE SIZE CLASSES
      SAVG          RAD          BDSURF        BVSURF       BDLTCE       BDATOM       BVATOM
 1.000000D+00  2.403720-08  3.645880-08  0.0          8.91584D-16  8.91584D-16  0.0
 5.07346D+02  2.182790-07  5.361530-12  0.0          2.14540D-17  2.14540D-17  0.0
FACE SIZE CLASS
 1.74847D+06  6.74474D-06  5.88134D-18  0.0
              1.99786D-05
EDGE SIZE CLASS
 2.31731D+06  7.63201D-06  3.58741D-18  0.0
              2.30000D-05

TAU=  3.017600D+04 H=  1.508800D+04 HNXT=  2.263200D+04 HH=  2.263200D+04

DISTRIBUTIONS FOLLOW (NUMBER/CM**3)
REGION 1  LTCE  3.6493D+19  3.5031D+16  FACE  1.5367D+12  EDGE  4.5175D+12

FLUX(I)=  2.2817D+12  7.5917D+07  0.0          0.0                    PBKGBY(I)=  0.0          0.0              GBS=  0.0

 J  K          RPIN          BVKJ          RGK          PRSG
 1  1   3.275543D-01   1.012556D-01   1.138592D-05   1.000000D+03

GSGEN= 2.1511082D-05 LTCEFR=8.0489051D-01 TKI=    1.7500000D+03 BVSL=  3.5490849D-03 EGRE=  8.6086471D-07 ALPHA= 0.0
GOUTK= 1.0125079D-05 FACEFR=3.9849665D-02 TKIO=   1.7500000D+03 BVSF=  1.7794000D-02 EPRF=  6.0932637D-08 ACAEN= 0.0
FGRK=  4.7069127D-01 EDGEFR=1.5525982D-01 GKOUT= 6.5754876D-09 BVSE=  7.9812504D-02 PRF=   8.3993029D-01 BETAB= 0.0

AXIAL TOTALS   J = 1
BVS=   1.0125559D-01 RGJ=   1.1385920D-05 GSRJ=  1.1524158D-08 RGGL=  4.2603245D-01 RGGF=  2.1092621D-02 RGGE=  8.2179777D-02
FGRJ=  4.7069127D-01

ROD TOTALS
FGRT=  4.7069127D-01 RGT=   1.1385920D-05 GTOUT= 1.1524158D-08 GRFT=  1.0125079D-05 GGT=   2.1511082D-05 ERR=   3.8820539D-06
RETI=  4.0401948D-07 RETC=  6.9124059D-06 OUTI=  3.5927698D-07 OUTC=  6.1469025D-06

********** END OF GRASS OUTPUT FOR THIS TIME STEP **********
```

Fig. 34 (cont.)

```
********** GRASS OUTPUT **********

TIME= 0.544978560D+08

------ AXIAL SECTION= 1 RADIAL SECTION= 1

RS(K,J)= 1.782550D-01 RS(K+1,J)= 2.532890D-01 TS(K,J)= 1.514520D+03 TS(K+1,J)=1.514520D+03 POROS = 7.4750J0D-02
DELT = 3.017600D+04 VOLUME = 1.017263D-01 PRFOLD = 8.704298D-01

TKI= 1.750000D+03 TGRAD= 0.0 DTDT= 0.0 TFPV= 9.9980D+12 GSIN= 3.0994D+12 GRD= 1.0000D-03 DCIE= 1.9996D-17

LATTICE SIZE CLASSES
      SAVG          RAD        BDSURF      BVSURF      BDLTCE      BDATOM      BVATOM
 1.00000D+00  2.40372D-08  3.64588D-08  0.0         8.91584D-16  8.91584D-16  0.0
 5.87964D+02  2.30850D-07  4.28565D-12  0.0         1.90829D-17  1.90829D-17  0.0
FACE SIZE CLASS
 1.74847D+06  6.74474D-06  5.88134D-18  0.0
              1.99786D-05
EDGE SIZE CLASS
 2.31731D+06  7.63201D-06  3.58741D-18  0.0
              2.30000D-05

TAU= 3.017600D+04 H= 1.508800D+04 HNXT= 2.263200D+04 HH= 2.263200D+04

DISTRIBUTIONS FOLLOW (NUMBER/CM**3)
REGION 1 LTCE 4.0309D+19 3.9839D+16 FACE 1.5386D+12 EDGE 4.7461D+12

FLUX(I)= 2.4277D+12 7.3343D+07 0.0 0.0 PBKGBY(I)= 0.0 0.0 GBG= 0.0

 J  K          RPIN          BVKJ          RGK          PNSG
 1  1  3.6756660-01  1.0606650-01  1.307452D-05  1.0000000+03

GSGEN= 2.8523505D-05 LTCEFR=8.2320220D-01 TKI= 1.7500000D+03 BVSL= 4.3979867D-03 EGRE= 9.1582710D-07 ALPHA= 0.0
GOUTK= 1.5448813D-05 FACEFR=3.4746459D-02 TKIO= 1.7500000D+03 BVSF= 1.7816276D-02 EPRF= 5.2462113D-08 ACAEN= 0.0
FGRK= 5.4161691D-01 EDGEFR=1.4205134D-01 GKOUT= 6.9350613D-09 BVSE= 8.3852240D-02 PRF= 8.7053239D-01 BETAB= 0.0

AXIAL TOTALS J = 1
BVS= 1.0606650D-01 RGJ= 1.3074515D-05 GSRJ= 1.2398793D-08 RGGL= 3.7733686D-01 RGGF= 1.5926974D-02 RGGE= 6.5113052D-02
FGRJ= 5.4151691D-01

ROD TOTALS
FGRT= 5.4161691D-01 RGT= 1.3074515D-05 GTOUT= 1.2398793D-03 GRFT= 1.5448813D-05 GGT= 2.8523505D-05 ERR= 6.2135262D-06
RETI= 4.6394070D-07 RETC= 7.9376037D-06 OUTI= 5.4818367D-07 OUTC= 9.3789243D-06

********** END OF GRASS OUTPUT FOR THIS TIME STEP **********
```

Fig. 34 (cont.)

```
********** GRASS OUTPUT **********

TIME= 0.6789600000D+08

------ AXIAL SECTION= 1 RADIAL SECTION= 1

RS(K,J)= 1.7825500-01 RS(K+1,J)= 2.5328900-01 TS(K,J)= 1.514520D+03 TS(K+1,J)=1.514520D+03 POROS = 7.4750000-02
DELT = 3.0176000+04 VOLUME = 1.0172630-01 PRFOLD = 8.8749930-01

TKI= 1.7500000+03 TGRAD= 0.0 DTDT= 0.0 TFPV= 9.9980D+12 GSIN= 3.0994D+12 GRD= 1.0000D-03 DCIE= 1.9996D-17

LATTICE SIZE CLASSES
      SAVG          RAD          EDSURF       BVSURF       BDLTCE       BDATOM       BVATOM
 1.0000D+00  2.4037200-03  3.6458800-08  0.0          8.9158400-16  8.9158400-16  0.0
 6.5071300+02  2.3995000-07  3.6716100-12  0.0          1.7600500-17  1.7600500-17  0.0
FACE SIZE CLASS
 1.7484700+06  6.7447400-06  5.8813400-18  0.0
               1.9978600-05
EDGE SIZE CLASS
 2.3173100+06  7.6320100-06  3.5874100-18  0.0
               2.3000000-05

TAU= 3.0176000+04 H= 1.5088000+04 HNXT= 2.2632000+04 HH= 2.2632000+04

DISTRIBUTIONS FOLLOW (NUMBER/CM**3)
REGION 1 LTCE 4.3142D+19 4.3523D+16 FACE 1.5400D+12 EDGE 4.8902D+12

FLUX(I)= 2.5361D+12 7.1218D+07 0.0 0.0 PBKGBY(I)= 0.0 0.0 GBS= 0.0

 J  K          RPIN          BVKJ          RGK          PRSG
 1  1  3.9632710-01  1.0925720-01  1.4436550-05  1.0000000+03

GSGEN= 3.5535928D-05 LTCEF= 3.3595064D-01 TKI= 1.7500000D+03 BVSL= 5.0284419D-03 EGRE= 9.5648699D-07 ALPHA= 0.0
GOUTK= 2.1099080D-05 FACEF= 3.1496086D-02 TKIO= 1.7500000D+03 BVSF= 1.7832026D-02 EPRF= 4.7521728D-08 ACAEN= 0.0
FGRK= 5.9373939D-01 EDGEFR=1.3255328D-01 GKOUT= 7.1965246D-09 BVSE= 8.6396772D-02 PRF= 8.8757999D-01 BETAB= 0.0

AXIAL TOTALS J = 1
BVS= 1.0925724D-01 RGJ= 1.4436547D-05 GSRJ= 1.3019970D-08 RGGL= 3.3960673D-01 RGGF= 1.2795352D-02 RGGE= 5.3850052D-02
FGRJ= 5.9373939D-01

ROD TOTALS
FGRT= 5.9373939D-01 RGT= 1.4436547D-05 GTOUT= 1.3019970D-08 GRFT= 2.1099080D-05 GGT= 3.5535928D-05 ERR= 8.4781500D-06
RETI= 5.1227525D-07 RETC= 8.7645638D-06 OUTI= 7.4867705D-07 OUTC= 1.2809184D-05

********** END OF GRASS OUTPUT FOR THIS TIME STEP **********
```

Fig. 34 (cont.)

```
**********
DELT= 1.0000D-01     NPRINT,IREAD,IP,IRSTAR,ITRAN,KFLX,NOPT=    1    0    1    1    1    0    0

TMAX,TDMIN,TDMAX=  1.0000D+07  2.0000D+02  3.1230D+03     IPRINT,JPRINT,IWRITE,IPOW= 2746    1    4    0
TD(K,J)=         1.0000D-01     1.0000D-01
DPOW(J)=         0.0
**********

                    ********** GRASS OUTPUT **********

                              TRANSIENT TIME=  0.2746000000D+03

------ AXIAL SECTION=  1 RADIAL SECTION=  1

RS(K,J)=  1.782550D-01 RS(K+1,J)=  2.532890D-01 TS(K,J)=  1.789120D+03 TS(K+1,J)=1.789120D+03 POROS =   7.4750000D-02
DELT   =  1.0000000-01 VOLUME   =  1.0172630-01 PRFOLD =  9.0018460-01

TKI= 2.0246000+03 TGRAD= 0.0       DTDT= 1.0000D+00 TFPV= 9.9980D+12 GSIN= 3.0994D+12 GRD= 1.0000D-03 DCIE= 1.9996D-17

LATTICE SIZE CLASSES
      SAVG          RAD        BDSURF       BVSURF       BDLTCE       BDATOM       BVATOM
 1.0000D+00  2.4083D-08  2.4486D-05  0.0          3.1086D-14  3.1086D-14  0.0
 1.6678D+04  9.3863D-07  1.0620D-12  0.0          3.2981D-16  3.2981D-16  0.0
FACE SIZE CLASS
 1.7484D+06  7.3798D-06  2.7794D-16  0.0
             2.2593D-05
EDGE SIZE CLASS
 2.3173D+06  8.3967D-06  1.6584D-16  0.0
             2.6009D-05

TAU=  1.000000D-01 H=  1.000000D-01 HNXT=  1.500000D-01 HH=  2.263200D+04

DISTRIBUTIONS FOLLOW (NUMBER/CM**3)
REGION 1  LTCE  4.1371D+19  1.8039D+15  FACE  2.1180D+08  EDGE  3.4624D+12

FLUX(I)=  8.4754D+13  5.5308D+07  0.0          0.0                    PBKGBY(I)=  0.0          0.0              GBS=  0.0

 J  K          RPIN          BVKJ          RGK          PRSG
 1  1   4.2103770-01   9.7141620-02   1.3421870-05   1.0000000+03

GSGEN= 3.5536072D-05 LTCEFR=3.9904816D-01 TKI=   2.0246000D+03 BVSL=  8.6708683D-03 EGRE=  2.2092275D-01 ALPHA= 2.2092275D-01
GOUTK= 2.2113899D-05 FACEFR=4.6591816D-06 TKIO=  2.0245000D+03 BVSF=  3.5467843D-06 EPRF=  0.0           ACAEN= 1.0471738D+03
FGRK=  6.2229441D-01 EDGEFR=1.0094718D-01 GKOUT= 1.2429423D-12 BVSE=  8.8467201D-02 PRF=   9.0015266D-01 BETAB= 1.6254866D-01

AXIAL TOTALS  J = 1
BVS=   9.7141616D-02 RGJ=   1.3421872D-05 GSRJ=  1.2429423D-12 RGGL=  3.3956790D-01 RGGF=  1.7597595D-06 RGGE=  3.8127460D-02
FGRJ=  6.2229441D-01

ROD TOTALS
FGRT=  6.2229441D-01 RST=   1.3421872D-05 GTOUT= 1.2429423D-12 GRFT=  2.2113899D-05 GGT=   3.5536072D-05 ERR=   8.6780787D-06
RETI=  4.7627066D-07 RETC=  8.1485581D-06 OUTI=  7.8466673D-07 OUTC=  1.3425277D-05

                    ********** END OF GRASS OUTPUT FOR THIS TIME STEP **********
```

Fig. 35. Execution of the Transient Portion of a Sample Problem with PARAGRASS. See text for details.

```
********** GRASS OUTPUT **********

TRANSIENT TIME=  0.549200000D+03

------ AXIAL SECTION=  1 RADIAL SECTION=  1

RS(K,J)=  1.7825500-01 RS(K+1,J)=  2.5320900-01 TS(K,J)=  2.0637200+03 TS(K+1,J)=2.0637200+03 POROS =  7.4750000-02
DELT   =  1.0000000-01 VOLUME   =  1.0172630-01 PRFOLD =  9.0836850-01

TKI= 2.0000000+03 TSRAD= 0.0      DTDT= 1.0000D+00 TFPV= 9.9980D+12 GSIN= 3.0994D+12 GRD= 1.0000D-03 DCIE= 1.9996D-17

LATTICE SIZE CLASSES
      SAVG          RAD        DCSURF       BVSURF       BDLTCE       BDATOM       BVATOM
 1.0000D+00  2.4151+D-08  5.9963?D-05  0.0          4.6404?0-13  4.6404?0-13  0.0
 2.5243?D+04  1.2151?D-06  9.3255?D-12  0.0          3.6736?D-15  3.6736?D-15  0.0
FACE SIZE CLASS
 1.7484?D+06  8.0881?D-06  4.7670?D-15  0.0
              2.5455?D-05
EDGE SIZE CLASS
 2.3173?D+06  9.1343?0-06  2.9305?D-15  0.0
              2.9305?0-05

TAU=  1.0000000-01 R=  1.0000000-01 RNXT=  1.5000000-01 RH=  2.2632?0D+04

DISTRIBUTIONS FOLLOW (NUMBER/CM**3)
REGION 1  LTCE  7.7889D+18  2.5159D+15  FACE  6.8024D+08  EDGE  2.4606D+12

FLUX(I)=  2.3649D+14  8.6028D+03  0.0          0.0                    FBKGBY(I)=  0.0          0.0                GBS=  0.0

 J  K          RPIN          BVKJ          RGK          PRSG
 1  1  8.9083?4D-01  1.0935470-01  1.3018530-05  1.0000000+03

GSGEN= 3.5536216D-05 LTCEFR=9.2602082D-01 TKI=   2.2992000D+03 BVSL=  1.9415689D-02 EGRE=  2.2508324D-01 ALPHA= 2.2508324D-01
GOUTK= 2.2517380D-05 FACEFR=1.5427828D-05 TKIO=  2.2991000D+03 BVSF=  1.6292669D-05 EPRF=  1.0439040D-04 ACAEN= 1.0668946D+03
FGRK=  6.3364597D-01 EDGEFR=7.3963755D-02 GKOUT= 1.4159958D-11 BVSE=  8.9922702D-02 PRF=   9.0836945D-01 BETAB= 1.4336511D-01

AXIAL TOTALS   J = 1
BVS=   1.0935468D-01 RGJ=   1.3018534D-05 GSRJ=  1.4159958D-11 RGGL=  3.3924360D-01 RGGF=  5.6519161D-06 RGGE=  2.7096293D-02
FGRJ=  6.3364557D-01

ROD TOTALS
FGRT=  6.3364597D-01 RGT=   1.3018534D-05 GTOUT= 1.4159958D-11 GRFT=  2.2517380D-05 GGT=   3.5536216D-05 ERR=   8.4782202D-06
RETI=  4.3195867D-07 RETC=  7.9036932D-06 OUTI=  7.9900381D-07 OUTC=  1.3670229D-05

********** END OF GRASS OUTPUT FOR THIS TIME STEP **********
```

Fig. 35 (cont.)

```
********** GRASS OUTPUT **********

TRANSIENT TIME=  0.8238000000D+03

------ AXIAL SECTION=  1 RADIAL SECTION=  1

RS(K,J)=  1.782550D-01 RS(K+1,J)=  2.532890D-01 TS(K,J)=  2.338320D+03 TS(K+1,J)=2.338320D+03 POROS =   7.475000D-02
DELT   =  1.000000D-01 VOLUME    =  1.017263D-01 PRFOLD =  9.183308D-01

TKI= 2.573800D+03 TGRAD= 0.0        DTDT= 1.0000D+00 TFPV= 9.9980D+12 GSIN= 3.0994D+12 GRD= 1.0000D-03 DCIE= 1.9996D-17

LATTICE SIZE CLASSES
      SAVG            RAD         BDSURF        BVSURF        BDLTCE        BDATOM        BVATOM
 1.000000D+00  2.423130-08  7.38410D-04  0.0           3.89075D-12  3.89075D-12  0.0
 8.801880+05   6.526670-06  1.40294D-13  0.0           6.39164D-15  6.39164D-15  0.0
FACE SIZE CLASS
 1.748470+06   8.783590-06  4.27694D-14  0.0
               2.867480-05
EDGE SIZE CLASS
 4.313760+06   1.285530-05  9.32122D-15  0.0
               4.504010-05

TAU=  1.000000D-01 H=  1.000000D-01 HNXT=  1.500000D-01 HH=  2.263200D+04

DISTRIBUTIONS FOLLOW (NUMBER/CM**3)
REGION 1  LTCE  9.7211D+16  8.0895D+13  FACE  1.6448D+08  EDGE  6.9193D+11

FLUX(I)=  2.3121D+13  4.8100D+07  0.0          0.0                  PBKGBY(I)=  0.0          0.0                GBS=  0.0

 J  K          RPIN           BVKJ           RGK          PRSG
 1  1   9.9863770-01   1.860206D-01   1.255457D-05   1.000000D+03

GSGEN= 3.5536359D-05 LTCEFR=9.5984297D-01 TKI=   2.5738000D+03 BVSL=  9.4213460D-02 EGRE=  2.2736806D-01 ALPHA= 2.2736806D-01
GOUTK= 2.2981493D-05 FACEFR=3.8683519D-06 TKIO=  2.5737000D+03 BVSF=  5.6313598D-06 EPRF=  0.0           ACAEN= 1.0777246D+03
FGRK=  6.4670363D-01 EDGEFR=4.0153162D-02 GKOUT= 1.0140183D-12 BVSE=  9.1801517D-02 PRF=   9.1831958D-01 BETAB= 4.8027022D-01

AXIAL TOTALS   J = 1
BVS=   1.8602061D-01 RGJ=   1.2554566D-05 GSRJ=  1.0140183D-12 RGGL=  3.3910090D-01 RGGF=  1.3666419D-06 RGGE=  1.4185626D-02
FGRJ=  6.4670363D-01

ROD TOTALS
FGRT=  6.4670363D-01 RGT=   1.2554566D-05 GTOUT= 1.0140183D-12 GRFT=  2.2981493D-05 GGT=   3.5536359D-05 ERR=   8.4781522D-06
RETI=  4.4549527D-07 RETC=  7.6220191D-06 OUTI=  8.1547232D-07 OUTC=  1.3951990D-05

********** END OF GRASS OUTPUT FOR THIS TIME STEP **********
```

Fig. 35 (cont.)

```
********** GRASS OUTPUT **********

TRANSIENT TIME=  0.109840000D+04

------ AXIAL SECTION=  1 RADIAL SECTION=  1

RS(K,J)=  1.782550D-01 RS(K+1,J)=  2.332890D-01 TS(K,J)=  2.612920D+03 TS(K+1,J)=2.612920D+03 POROS =   7.475000D-02
DELT   =  1.000000D-01 VOLUME   =  1.017263D-01 PRFOLD =  9.233147D-01

TKI= 2.848400D+03 TGRAD= 0.0        DTDT= 1.0000D+00 TFPV= 9.9980D+12 GSIN= 3.0994D+12 GRD= 1.0000D-03 DCIE= 1.9996D-17

LATTICE SIZE CLASSES
      SAVG          RAD        BDSURF       BVSURF       BDLTCE       BDATOM       BVATOM
 1.00000D+00  2.43358D-08  5.56705D-03  0.0          2.16499D-11  2.16499D-11  0.0
 3.97361D+06  1.33819D-05  6.08882D-14  0.0          1.23104D-14  1.23104D-14  0.0
FACE SIZE CLASS
 5.90108D+06  1.57099D-05  3.20559D-14  0.0
              5.95360D-05
EDGE SIZE CLASS
 5.40186D+06  1.51599D-05  3.69679D-14  0.0
              5.69620D-05

TAU=  1.000000D-01 H=  1.000000D-01 HNXT=  1.500000D-01 HH=  2.263200D+04

DISTRIBUTIONS FOLLOW (NUMBER/CM**3)
REGION 1  LTCE  1.4385D+16  1.7942D+13  FACE  7.1711D+07  EDGE  3.4559D+11

FLUX(I)=  1.6155D+13  2.0531D+07  0.0          0.0                  PBKGBY(I)=  0.0          0.0              GBS=  0.0

 J  K          RPIN          BVKJ          RGK          PRSG
 1  1  9.997984D-01  2.728759D-01  1.236242D-05  1.000000D+03

GSGEN= 3.5536503D-05 LTCEFR=9.7447755D-01 TKI=   2.8484000D+03 BVSL=  1.8010530D-01 EGRE=  2.2941500D-01 ALPHA= 2.2941500D-01
GOUTK= 2.3173786D-05 FACEFR=5.7804690D-06 TKIO=  2.8483000D+03 BVSF=  2.1974336D-05 EPRF=  4.0743616D-03 ACAEN= 1.0874271D+03
FGRK=  6.5211218D-01 EDGEFR=2.5516555D-02 GKOUT= 1.3006405D-10 BVSE=  9.2748619D-02 PRF=   9.2334592D-01 BETAB= 6.5025596D-01

AXIAL TOTALS   J = 1
BVS=   2.7287589D-01 RGJ=   1.2362415D-05 GSRJ=  1.3006405D-10 RGGL=  3.3900065D-01 RGGF=  2.0109058D-06 RGGE=  8.8766860D-03
FGRJ=  6.5211218D-01

ROD TOTALS
FGRT=  6.5211218D-01 RGT=   1.2362415D-05 GTOUT= 1.3006405D-10 GRFT=  2.3173786D-05 GGT=   3.5536503D-05 ERR=   8.4781079D-06
RETI=  4.3867704D-07 RETC=  7.5053654D-06 OUTI=  8.2229565D-07 OUTC=  1.4068731D-05

********** END OF GRASS OUTPUT FOR THIS TIME STEP **********
```

Fig. 35 (cont.)

```
********** GRASS OUTPUT **********

                    TRANSIENT TIME=  0.1373000000D+04

------ AXIAL SECTION=  1 RADIAL SECTION=  1

RS(K,J)=  1.7825500-01 RS(K+1,J)=  2.5328900-01 TS(K,J)=  2.8875200+03 TS(K+1,J)=2.8875200+03 POROS =   7.4750000-02
DELT   =  1.0000000-01 VOLUME    =  1.0172630-01 PRFOLD =  9.2918500-01

TKI= 3.1230000+03 TORAD= 0.0        DTDT= 1.0000D+00 TFPV= 9.9980D+12 GSIN= 3.0994D+12 GRD= 1.0000D-03 DCIE= 1.9996D-17

LATTICE SIZE CLASSES
        SAVG          PAD          BDSURF       BVSURF       BOLTCE       BDATOM       BVATOM
 1.000000+00  2.447830-08  2.915340-02  0.0          8.908180-11  8.908180-11  0.0
 1.016190+07  2.079110-05  5.601470-14  0.0          1.943520-14  1.943520-14  0.0
FACE SIZE CLASS
 1.327740+07  2.304280-05  3.712510-14  0.0
              1.016730-04
EDGE SIZE CLASS
 1.031000+07  2.090760-05  5.477710-14  0.0
              8.959390-05

TAU=  1.0000000-01 H=  1.0000000-01 HNXT=  1.5000000-01 HH=  2.2632000+04

DISTRIBUTIONS FOLLOW (NUMBER/CM**3)
REGION 1  LTCE  3.7901D+15  7.0146D+12  FACE  4.6127D+07  EDGE  9.0053D+10

FLUX(I)=  1.4942D+13  1.2663D+07  0.0          0.0                    PBKGBY(I)=  0.0          0.0              GBS=  0.0

 J  K          RPIN          BVKJ          RGK           PRSG
 1  1   9.999668D-01  3.581862D-01  1.219840D-05  1.000000D+03

GSGEN= 3.5536470-05 LTCEFR=9.87134440-01 TKI=   3.12300000+03 BVSL=  2.6407380D-01 EGRE=  2.3337735D-01 ALPHA= 2.3337735D-01
GOUTK= 2.3337942D-05 FACEFR=8.47835510-06 TKIO=  3.12290000+03 BVSF=  7.0398564D-05 EPRF=  0.0           ACAEN= 1.1062087D+03
FGRK=  6.5672886D-01 EDGEFR=1.28570810-02 GKOUT= 2.24248930-12 BVSE=  9.4042034D-02 FRF=   9.2914138D-01 BETAB= 7.1612977D-01

AXIAL TOTALS   J = 1
BVS=   3.5818623D-01 RGJ=   1.2198404D-05 GSRJ= 2.24248930-12 RGGL=  3.3884640D-01 RGGF=  2.9103028D-06 RGGE=  4.4133557D-03
FGRJ=  6.5672886D-01

ROD TOTALS
FGRT=  6.5672886D-01 RGT=   1.2198404D-05 GTOUT= 2.24248930-12 GRFT=  2.3337942D-05 GGT=   3.5536647D-05 ERR=   8.4780439D-06
RETI=  4.3285729D-07 RETC=  7.4057947D-06 OUTI=  8.2812051D-07 OUTC=  1.4168389D-05

********** END OF GRASS OUTPUT FOR THIS TIME STEP **********

DELT= 0.0          NPRINT,IREAD,IP,IRSTAR,ITRAN,KFLX,NOPT=   0   0   0   0   0   0   0


     TIME          RGGL          RGGF          RGGE          FGR
    T13.DATA1.DATA-175OK, .300C/CM, 10 UM AND 3.0 AT. BU
1.000000-03 1.000000+00 2.006650-10 0.0          0.0
9.052800+05 9.283960-01 7.110310-02 0.0          0.0
1.430340+07 6.048690-01 6.022260-02 1.558330-01 1.790250-01
2.770160+07 4.936880-01 3.123390-02 1.100350-01 3.650410-01
4.109970+07 4.260320-01 2.109260-02 8.217980-02 4.706910-01
5.449790+07 3.773370-01 1.592700-02 6.511310-02 5.416170-01
6.789630+07 3.396070-01 1.279540-02 5.385010-02 5.937390-01
2.746000+02 3.395680-01 1.759760-06 3.812750-02 6.222940-01
5.492000+02 3.392440-01 5.651920-06 2.709630-02 6.336660-01
8.238000+02 3.391010-01 1.366610-06 1.418560-02 6.467040-01
1.098400+03 3.390010-01 2.010910-06 8.876690-03 6.521120-01
1.373000+03 3.388460-01 2.910300-06 4.413360-03 6.567290-01
```

Fig. 35 (cont.)

III. CLAD PROPERTIES FOR CODE VERIFICATION

Principal Investigators:
H. M. Chung, F. L. Yaggee, and T. F. Kassner

A. Introduction

The Zircaloy cladding of light-water-cooled reactor fuel rods is susceptible to local breach-type failures, commonly known as pellet-cladding interaction (PCI) failures, during power transients after the fuel has achieved high burnup. As a result of the high burnup, the gap between the UO_2 fuel pellets and the cladding is closed and highly localized stress is believed to be imposed on the cladding by differential thermal expansion of the cracked fuel and cladding during power transients. In addition to the localized stress, a high-burnup fuel cladding is also characterized by high-density radiation-induced defects (RID), mechanical constraints imposed by pellet-cladding friction, compositional changes (e.g., oxygen and hydrogen uptake associated with in-service corrosion), and geometrical changes due to creep-down and bowing. It is possible that synergistic effects involving more than one of the above factors influence the deformation and fracture of the in-reactor fuel cladding, e.g., strain aging associated with impurity or alloying elements, irradiation- or stress-induced segregation of the elements, and subsequent formation of nonequilibrium phases. Although stress corrosion cracking (SCC, associated with volatile fission products such as I) and liquid metal embrittlement (LME, associated with elements such as Cd) mechanisms have been well established for local breach-type failures of irradiated and unirradiated Zircaloy cladding under out-of-reactor simulation conditions, conclusive evidence of these processes is not yet available for in-reactor PCI failures. Consequently, to provide a better understanding of the PCI phenomenon, a mechanistic study of deformation and fracture behavior of actual power-reactor fuel cladding, discharged after a high burnup, is in progress.

In this program, the effect of temperature, strain rate, and stress localization on the deformation and fracture characteristics of Zircaloy spent-fuel cladding is investigated by means of internal gas-pressurization-loading mandrel-loading experiments in the absence of simulated fission product species. The deformed and fractured spent-fuel cladding specimens are

then examined by optical microscopy, SEM, TEM, and HVEM. The data on microstructure and fracture properties will be used to develop a failure criterion for the cladding under PCI-type loading conditions. The information will be incorporated into fuel performance codes, which can be used to evaluate the susceptibility of extended-burnup fuel elements in commercial reactors to PCI failures during power transients in later cycles, and to evaluate cladding performance and reliability in new fuel element designs. An optimization of power ramp procedures to minimize cladding failures would result in a significant decrease in radiation exposure of plant personnel due to background and airborne radioactivity as well as in an extension of core life in terms of allowable off-gas radioactivity.

B. Chacteristics of Brittle-Type Fracture of High-Burnup Fuel Cladding Under Internal Gas-Pressurization Loading (H. M. Chung and F. L. Yaggee)

1. Introduction

Characteristics of PCI-like brittle-type fractures of Big Rock Point fuel cladding (Zircaloy-2) produced from internal gas-pressurization tests at 325°C have been reported previously.[36] A brittle-type PCI-like failure was usually characterized by small diametral strain at failure, negligible wall thinning, pinhole or tight-crack morphology of the failure site, numerous branching cracks extending partly through the wall near the through-wall crack, and pseudocleavage-plus-fluting features in the fracture surface. In some of the Big Rock Point cladding specimens, pseudocleavage-plus-fluting features were observed over about 95% of the wall thickness. H. B. Robinson cladding specimens, tested at 292-325°C under gas pressurization loading described in an earlier report,[37] have been evaluated during this period to identify brittle-type fractures.

2. SEM Examination of H. B. Robinson Cladding

Fracture surfaces of several Big Rock Point and H. B. Robinson cladding tubes that failed under internal gas-pressurization loading at 292 or 325°C were scanned by SEM, and the size of the fracture area characterized by the pseudocleavage-plus-fluting feature was determined. The specimen characteristics and test results are summarized in Table XIII. Typical SEM fractographs are shown in Fig. 36 for the 217C4B specimen described in Ref. 37.

TABLE XIII. Summary of Stress Rupture Test Results for Spent Zircaloy Fuel Cladding

Specimen Number	Reactor	Material	Fuel Burnup, MWd/kg U	Fluence, 10^{21} n/cm^2 (E > 0.1 MeV)	Test Temp., °C	Hoop Stress MPa	Hoop Stress ksi	Failure Time, h	Failure Diametral Strain, %	Average Diametral Strain Rate, s^{-1}	F_p[a]
165AC10	Big Rock Point[b]	Zircaloy-2	22.4	3.3	325	384	55.6	1.0	1.1	3.0×10^{-6}	0.95
165AE4A	↓	↓	↓	3.3	325	344	49.8	25.1	0.8	9.0×10^{-7}	0
165AE4B	↓	↓	↓	3.3	325	337	48.8	207.6	0.4	5.4×10^{-9}	0.78
165W-21	↓	↓	↓	4.0	325	514	74.5	7.9	1.0	3.5×10^{-7}	0
217A2G	H. B. Robinson[c]	Zircaloy-4	27.7	4.4	292	552	80.1	113.2	11.7	3.0×10^{-7}	0
217B2B	↓	↓	↓	↓	292	545	79.0	108.2	2.5	6.0×10^{-8}	-
217B4B	↓	↓	↓	↓	292	498	72.3	218.5	1.4	2.0×10^{-8}	0.14
217C2B	↓	↓	↓	↓	325	469	68.5	236.7	2.4	3.0×10^{-8}	0.17
217C4B	↓	↓	↓	↓	325	315	45.8	311.6	-	-	0.40
217A4B	↓	↓	↓	↓	325	315	45.8	294.2	-	-	0.12

[a]Maximum fraction of wall thickness exhibiting pseudocleavage-plus-fluting features in the fracture surface (see text).
[b]Oxide layer thickness: 0.5-10 μm on inner surface and 50-70 μm on outer surface.
[c]Oxide layer thickness: 0.5-7 μm on inner surface and 20-30 μm on outer surface.

Figure 36(A) shows the outer-surface crack morphology of the specimen, which indicates that the cracks initiated on the outer surface and propagated toward the inner surface. In the overall fracture surface map shown in Fig. 36(B), the areas bounded by the dark lines correspond to the pseudocleavage-plus-fluting feature, which is shown at higher magnifications in Figs. 36(C) and (F). Figures 36 (D) and (H) show ductile-fracture surface morphologies that were observed outside the bounded area. The fracture surface morphology of the transitional area [Area 4 of Fig. 36(E)] between the ductile (Area 5) and the psuedocleavage-plus-fluting (Area 3) regions is shown at high magnification in Fig. 36(G).

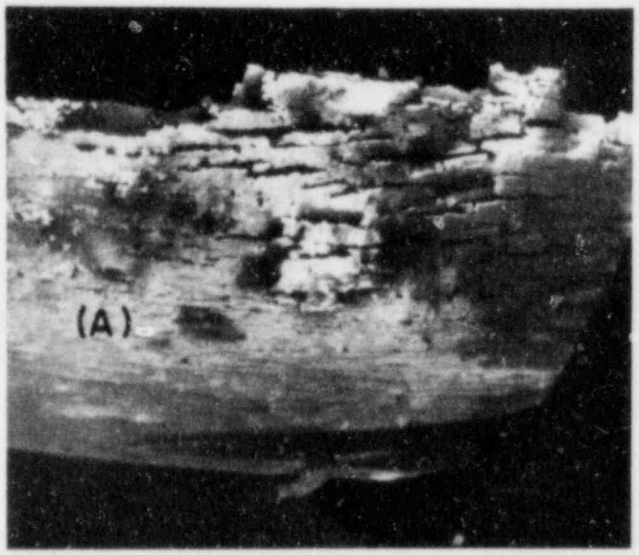

Fig. 36. SEM Fractographs of H. B. Robinson Reactor Cladding Specimen 217C4B (see Table XIII) after Fracture by Internal Gas Pressurization. (A) Outer-surface morphology; (B) overall fracture surface morphology showing pseudocleavage-plus-fluting areas bounded by dark lines near the outer surface; (C) higher magnification of Spot 1 of (B); (D) higher magnification of Spot 2 of (B); (E) higher magnification of Area L of (B); (F), (G), and (H) higher magnifications of Areas 3, 4, and 5 of (E), respectively.

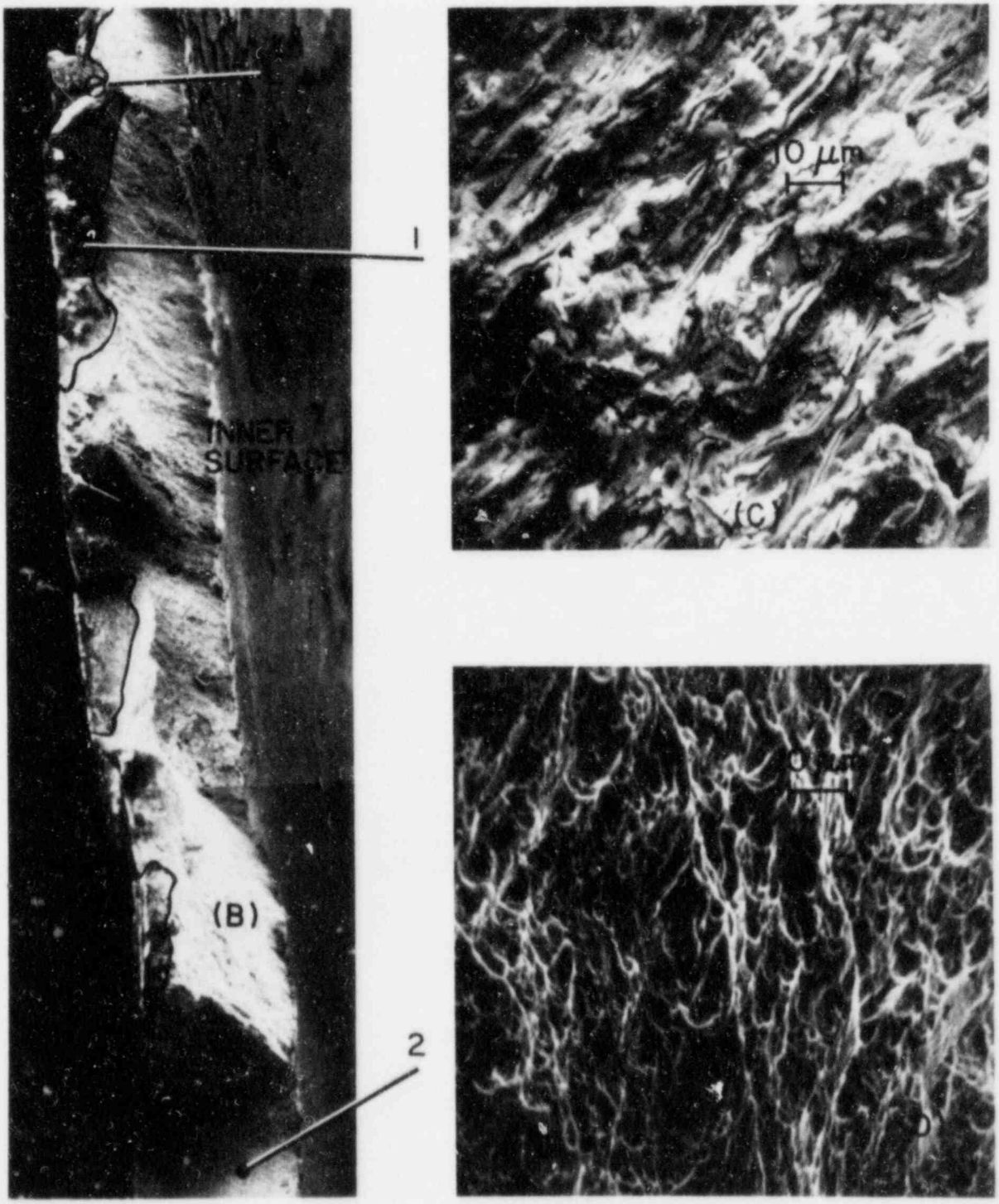

Fig. 36. (Contd.)

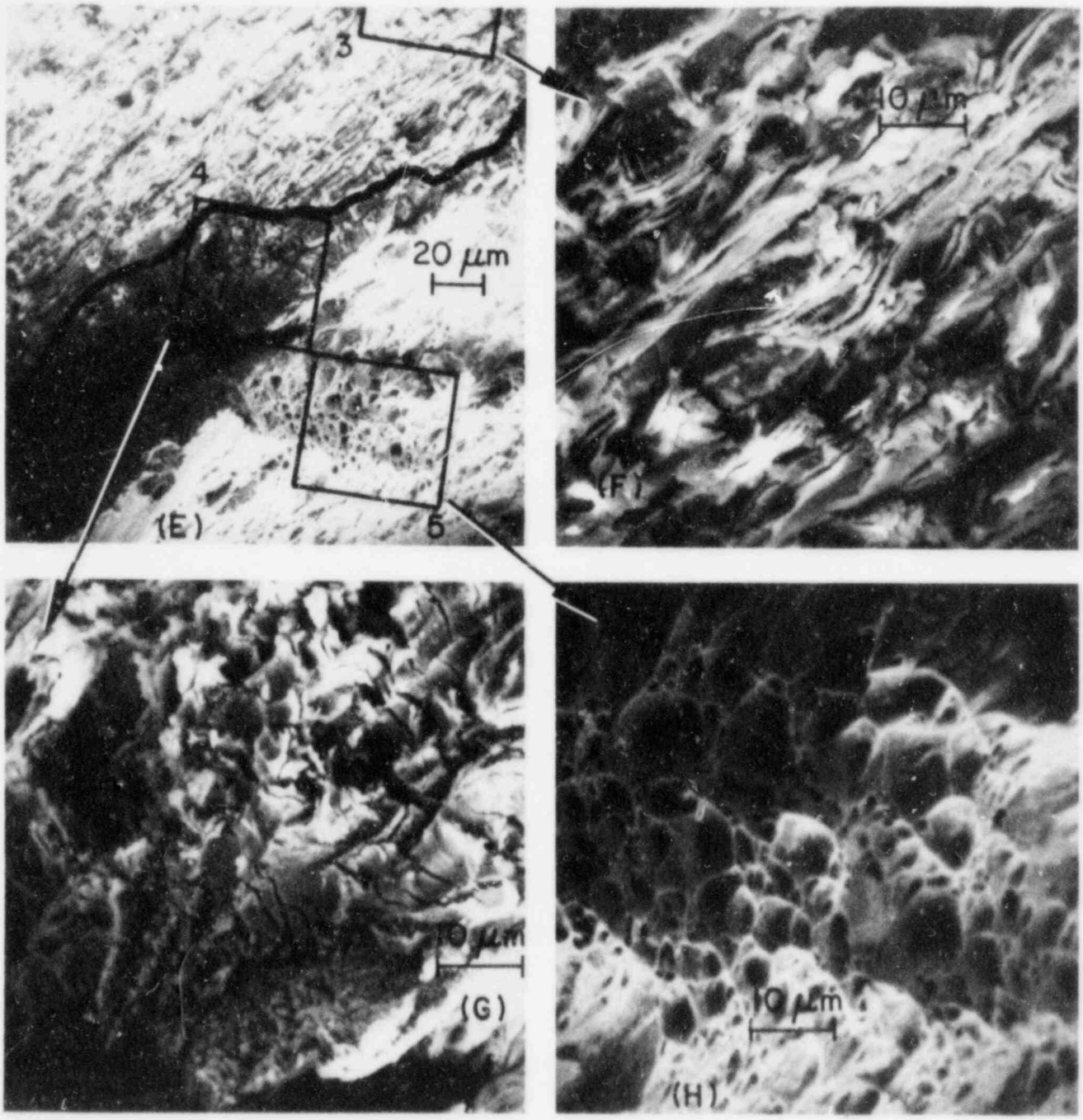

Fig. 36. (Contd.)

From the fracture surface maps similar to that of Fig. 36(B), the maximum penetration of the pseudocleavage-plus-fluting feature was determined for each specimen in terms of fractional wall thickness. For example, in Fig. 36(B), the maximum penetration corresponds to about 40% of the wall thickness. The fractional penetrations determined in this way, designated F_p parameters, are listed in Table XIII. Figure 37 shows an example of a Big Rock Point cladding fracture surface which corresponds to an F_p parameter of about 0.61. A similar fracture surface of an H. B. Robinson cladding tube shown in Fig. 38 corresponds to an F_p parameter of about 0.17. Failed

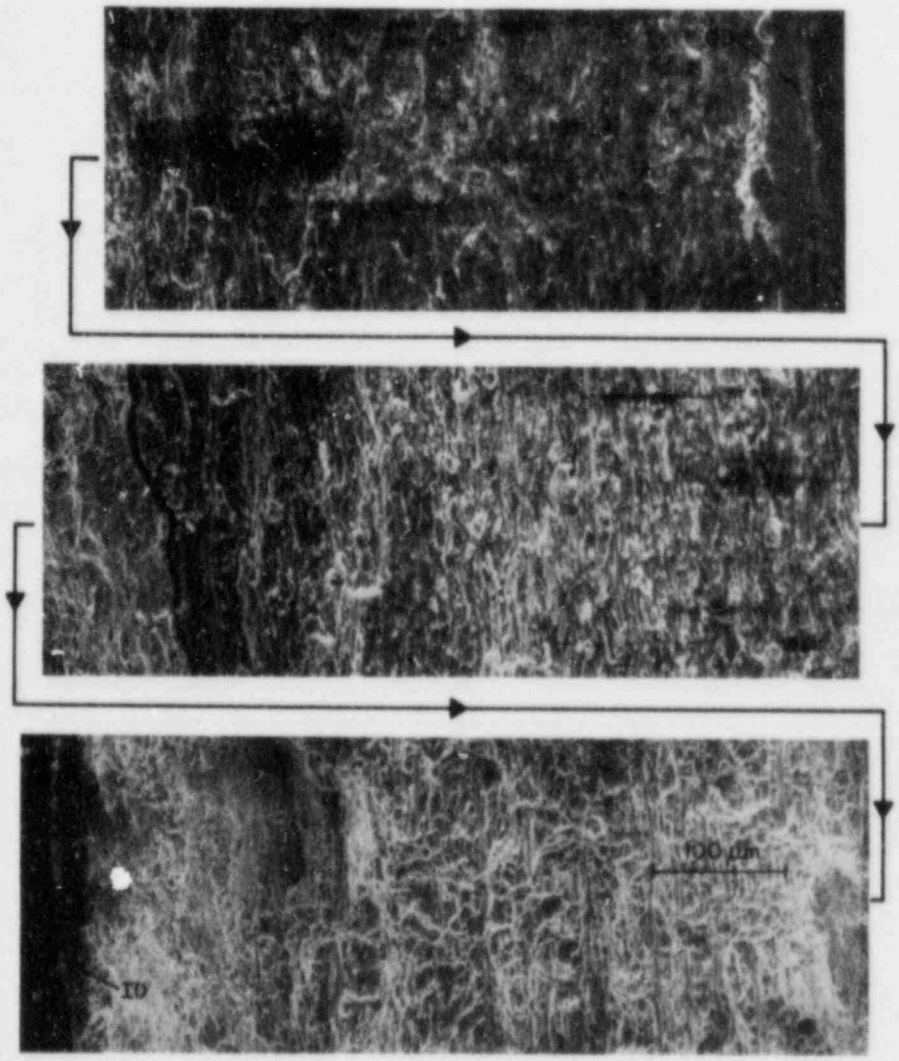

Fig. 37. Fracture Surface Morphology of Big Rock Point Reactor Cladding Specimen 165AE4B after Fracture by Internal Gas Pressurization. Pseudocleavage plus fluting is visible over ~60% of the distance from the outer to the inner surface.

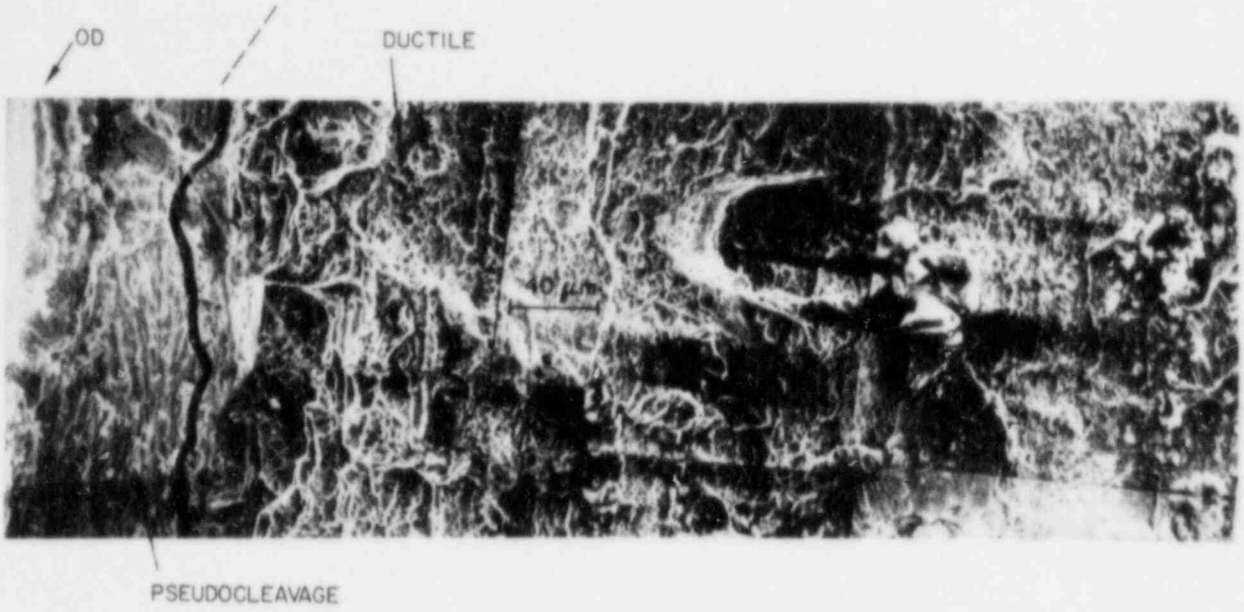

Fig. 38. Fracture Surface Morphology of H. B. Robinson Reactor Cladding Specimen 217C2B after Fracture by Internal Gas Pressurization. Pseudocleavage is visible over ~17% of the distance from the outer to the inner surface.

specimens with large F_p parameters were also associated with small diametral strains, usually less than about 1%, and with negligible wall thinning in the failure region.

3. Crack Initiation and Propagation

In all the specimens with non-zero F_p values (Table XIII), the through-wall cracks propagated from the outer to the inner surface of the cladding tube. Under internal gas-pressurization loading of the cladding tubes, the effective stress at the inner surface is slightly greater than that at the outer surface, i.e., by ~1% for the Big Rock Point cladding and ~0.3% for the H. B. Robinson cladding. However, at the outer surface, additional hoop stress is exerted on the metal as a result of the volume expansion associated with formation of the oxide layer (see Table XIII for oxide layer thicknesses). According to the measurement reported by Bradhurst and Heuer,[38] the order of magnitude of the intrinsic hoop stress is the same as that of the applied hoop stress listed in Table XIII; therefore, it is expected that the actual effective hoop stress is higher at the outer surface than at the inner

surface. This model is consistent with the crack distribution revealed in Fig. 39. In this figure, numerous cracks in the metal can be observed at the outer surface, which is covered by an oxide layer. However, in the region (bottom photograph of Fig. 39) in which the oxide layer spalled and tensile stress was thus relieved, no such cracks are observed.

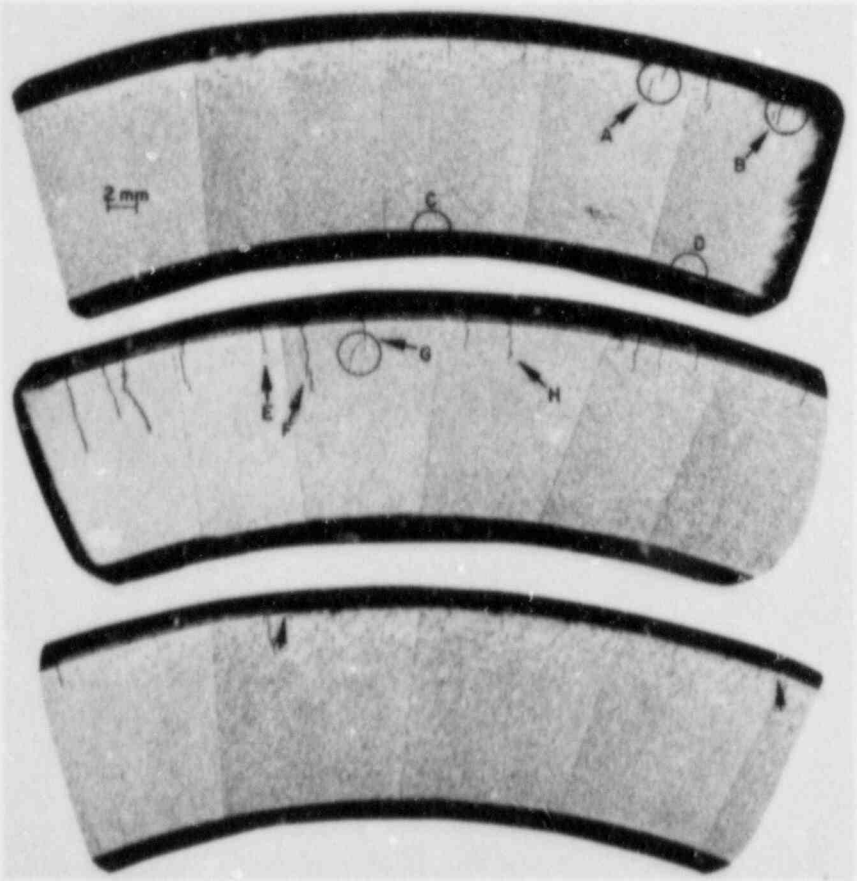

Fig. 39. Cross Sections Obtained from Regions Opposite the Brittle-Type Through-Wall Fracture Site of Big Rock Point Reactor Cladding Tube 165AE4B, Showing Distribution and Morphology of Numerous Partially Through-Wall Cracks. Note the absence of cracks in the outer-surface region (bottom) from which the oxide layer spalled; here, loss of the oxide layer relieved the intrinsic tensile stress associated with metal-to-oxide volume expansion.

To verify the hypothesis regarding the influence of the oxide layer on crack initiation and on propagation direction, the oxide layer on a smooth region of the outer surface of a Maine Yankee reactor cladding tube was removed by mechanical abrasion and the specimen was subsequently ruptured at

325°C as in the earlier experiments. The abrasion mark on the outer surface is visible in Fig. 40(A), which also shows a pinhole-type through-wall crack (circled). Figures 40(B) and (C) show the site of this crack at successively higher magnifications. The micrograph of Fig. 40(C) clearly indicates a ductile fracture near the outer surface. However, the morphologies of the inner surface opposite the outer-surface crack, shown in Figs. 40(D) and (E), reveal numerous brittle cracks parallel to the axial direction. The fracture surface morphology, partially revealed in Fig. 40(E) near the inner surface, is clearly brittle-type. Therefore, it is evident that the crack in this case initiated at the inner surface and propagated toward the outer surface. The observation described in association with Fig. 40 provides evidence of the effect of the oxide layer on crack initiation and propagation under simple gas-pressurization loading conditions. The observation is consistent with the inference discussed in association with Fig. 39.

If similar tests were performed with iodine added to the internal pressurizing gas, it is likely that the cracks would be nucleated on the inner surface and propagate toward the outer surface by an SCC process. However, if the outer-surface oxide layer were sufficiently thick, partial cracks might be nucleated on the outer surface in association with the oxide layer even in the presence of iodine. In fact, such partial cracks can be observed in micrographs (Figs. 4-5, 4-6, and 4-7 of Ref. 39) of Quad City reactor spent-fuel cladding, which was fractured under conditions similar to those in the present investigation but with iodine added to the inner-surface atmosphere.

C. TEM-HVEM Analysis of Zr_3O Precipitates (H. M. Chung)

1. Introduction

The morphology and orientation of the Zr_3O phase observed in association with the brittle-type, PCI-like failures of the Big Rock Point and H. B. Robinson spent fuel cladding has been reported previously.[36,40,41] Further results of TEM-HVEM analyses, reported below, provide a better understanding of the precipitation characteristics of the Zr_3O phase. Some orientations that differ from the previously reported ones[40,41] are described. The

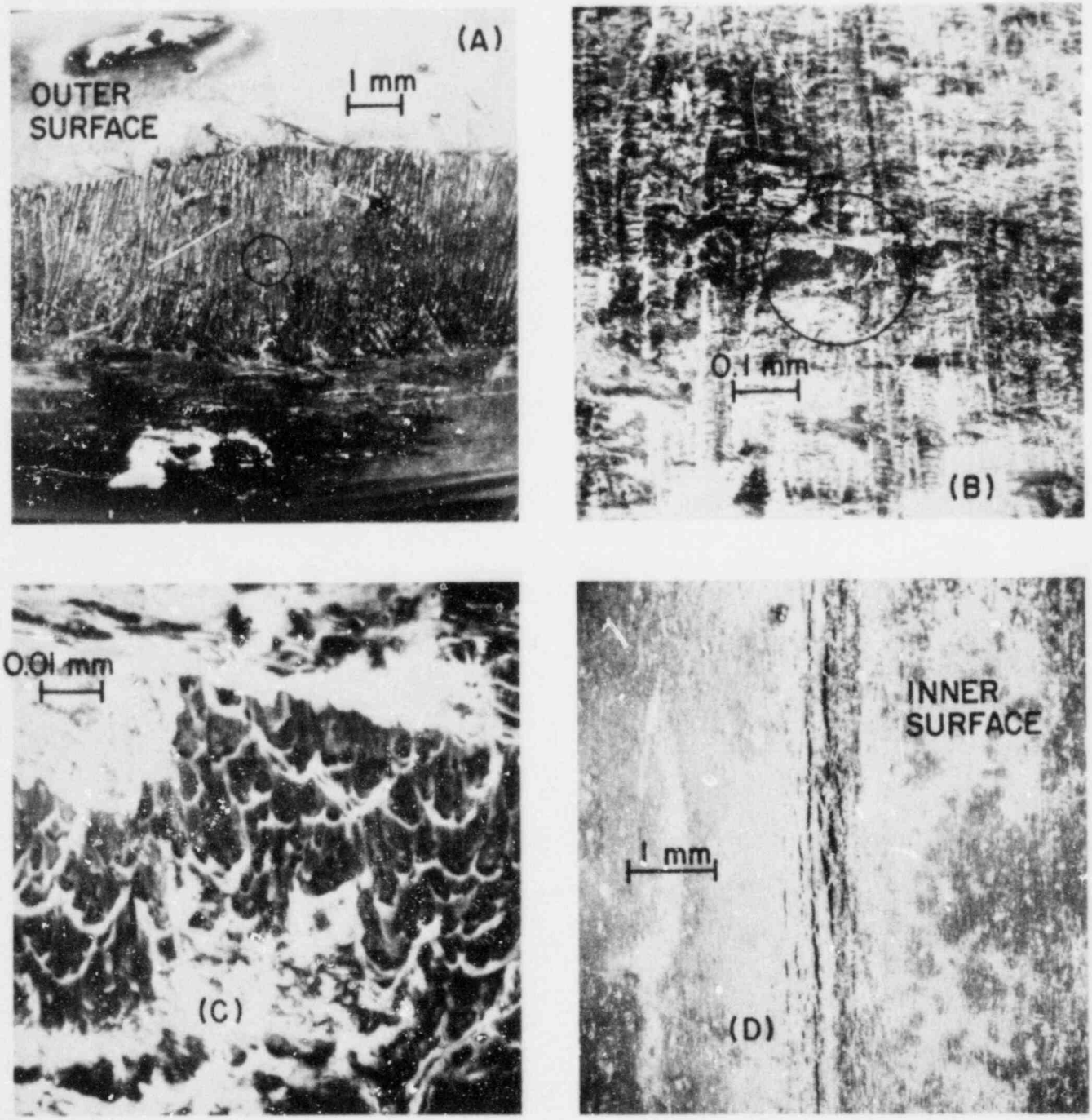

Fig. 40. SEM Micrographs of Maine Yankee Reactor Cladding Tube 217K2G after Removal of Oxide Layer from Part of the Outer Surface and Fracture by Internal Gas Pressurization. (A) Outer surface, with a pinhole failure site (circled) at the center of the region from which the oxide layer was removed; (B) higher magnification of the circled area of (A); (C) higher magnification of the circled area of (B), showing ductile fracture surface near the outer surface of the tube; (D) crack morphology of the inner surface, showing initiation of numerous partial cracks; and (E) higher magnification of (D).

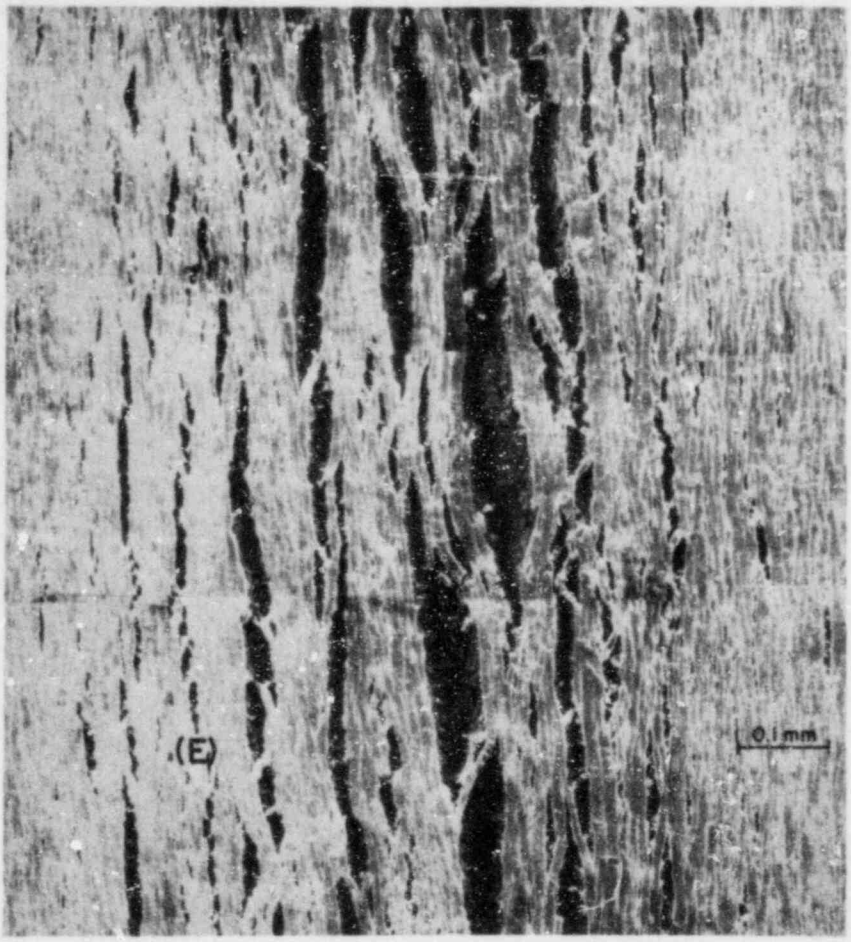

Fig. 40. (Contd.)

observed correlation between the Zr_3O precipitates and brittle-type PCI-like failure is then discussed on the basis of oxygen segregation phenomena associated with strain aging and radiation-induced segregation (RIS).

2. Diffraction Analysis

a. $(0001)_{Zr_3O}$ // $(10\bar{1}0)_\alpha$, $[\bar{1}2\bar{1}0]_{Zr_3O}$ // $[0001]_\alpha$ Orientation

The diffraction patterns containing reflections from α-Zr (α_I phase) and Zr_3O (α_{II}-phase) and indexed in Figs. 41 and 42 are similar to that of Fig. 14 of Ref. 41. Both patterns reveal an orientation $[1\bar{1}00]_{Zr_3O}$ // $[1\bar{2}13]_\alpha$, $(11\bar{2}1)_{Zr_3O}$ // $(0i\bar{1}1)_\alpha$ which is equivalent to $(0001)_{Zr_3O}$ // $(10\bar{1}0)_\alpha$, $[\bar{1}2\bar{1}0]_{Zr_3O}$ // $[0001]_\alpha$.[41] The diffraction analysis

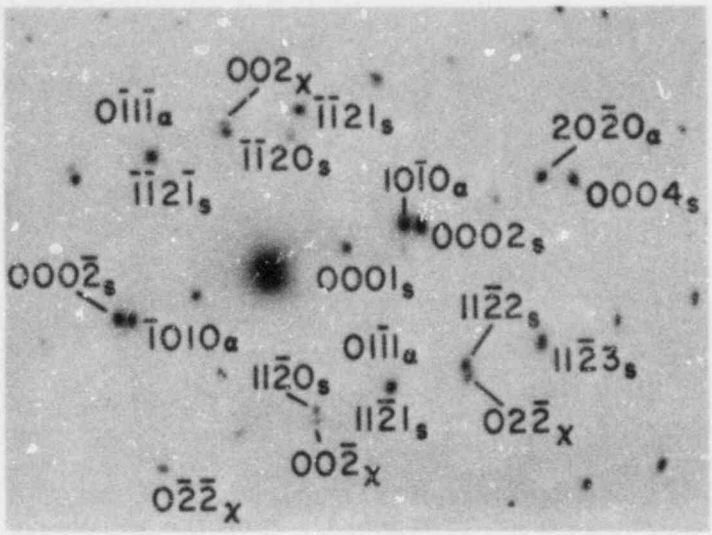

Fig. 41. A Selected Area Diffraction Pattern from Big Rock Point Reactor Cladding Specimen 165AG10 Showing Zone Axes $[1\bar{2}13]_\alpha$ // $[1\bar{1}00]_{Zr_3O}$ and Planes $(01\bar{1}1)_a$ // $(11\bar{2}1)_{Zr_3O}$. Subscripts α, s, and χ denote, respectively, reflections from α-Zr, Zr_3O precipitate, and χ-hydride.

shown in Fig. 43(C) reveals Zr_3O superlattice reflections of $(\bar{5}6\bar{1}1)_{Zr_3O}$ and $(5\bar{6}1\bar{1})_{Zr_3O}$ and the $[\bar{1}7\ 28\ \bar{1}\bar{1}\ 9]_\alpha$ zone axis of the α-Zr matrix. Numerous double diffraction spots arising from the Zr_3O reflections are visible in the selected area diffraction pattern of Fig. 43(C). The orientation revealed in Fig. 43(C) is also equivalent to $(0001)_{Zr_3O}$ // $(10\bar{1}0)_\alpha$, $[\bar{1}2\bar{1}0_{Zr_3O}$ // $[0001]_\alpha$. In Figs. 43(D) and (E), dark-field images of the double diffraction of $(5\bar{6}1\bar{1})_{Zr_3O}$ are shown. Zr_3O precipitates decorating short dislocations are visible near the arrow of Fig. 43(D). The precipitates on the dislocations could be observed most clearly by examining the original negative (photographed at about 30,000X) with a magnifying glass (~10X).

b. $(11\bar{2}\bar{1})_{Zr_3O}$ // $(01\bar{1}1)_\alpha$, $[1\bar{1}00]_{Zr_3O}$ // $[1\bar{2}13]_\alpha$ Orientation

The diffraction pattern indexed in Fig. 44 shows zones of α-Zr and Zr_3O identical to those of Figs. 41 and 42, i.e., $[1\bar{2}13]_\alpha$ and $[1\bar{1}00_{Zr_3O}$. However, in this orientation, the Zr_3O pattern is rotated 60° counterclockwise with respect to the $[\bar{1}2\bar{1}\bar{3}]_\alpha$ zone axis of the α-Zr. Thus, the orientation can be denoted by $(11\bar{2}\bar{1})_{Zr_3O}$ // $(01\bar{1}1)_\alpha$, $[1\bar{1}00)_{Zr_3O}$ // $[1\bar{2}13]_\alpha$. Another selected-area diffraction pattern that reveals an identical orientation is

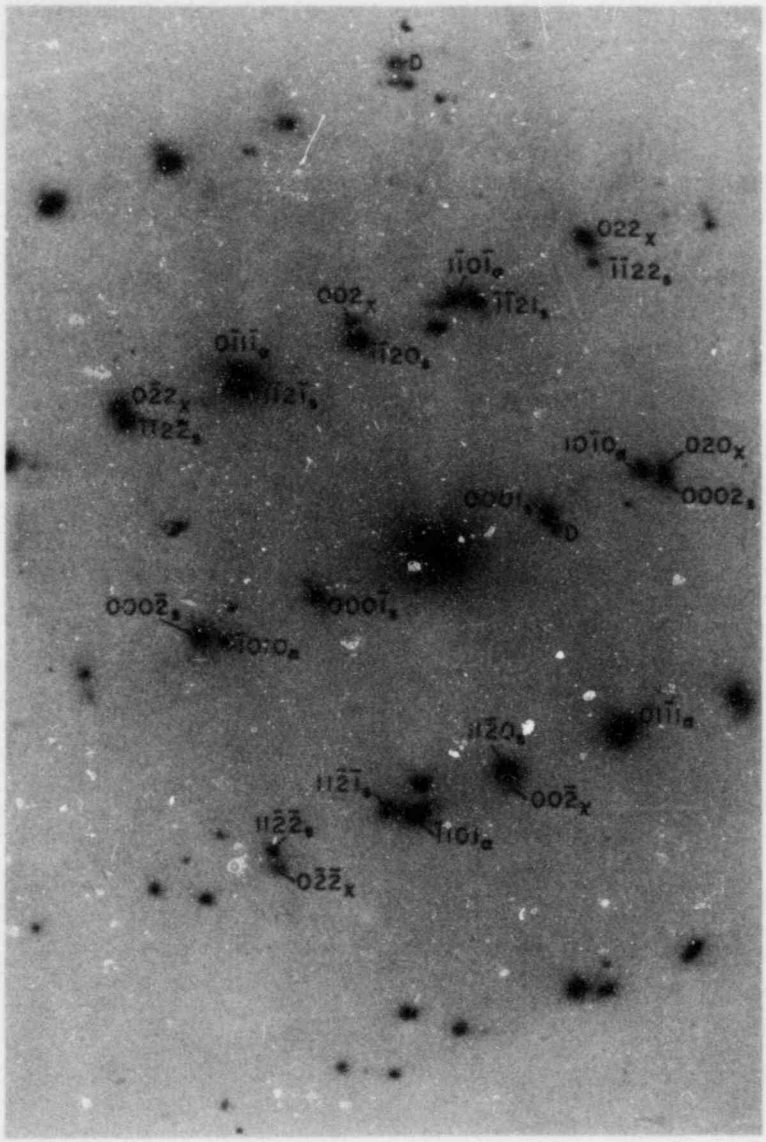

Fig. 42. A Selected Area Diffraction Pattern from Big Rock Point Reactor Cladding Specimen 165AG10 Showing an Orientation of α-Zr and Zr_3O Phases Similar to that of Fig. 41. Subscripts α, s, and χ denote, respectively, reflections from α-Zr, Zr_3O precipitate, and χ-hydride.

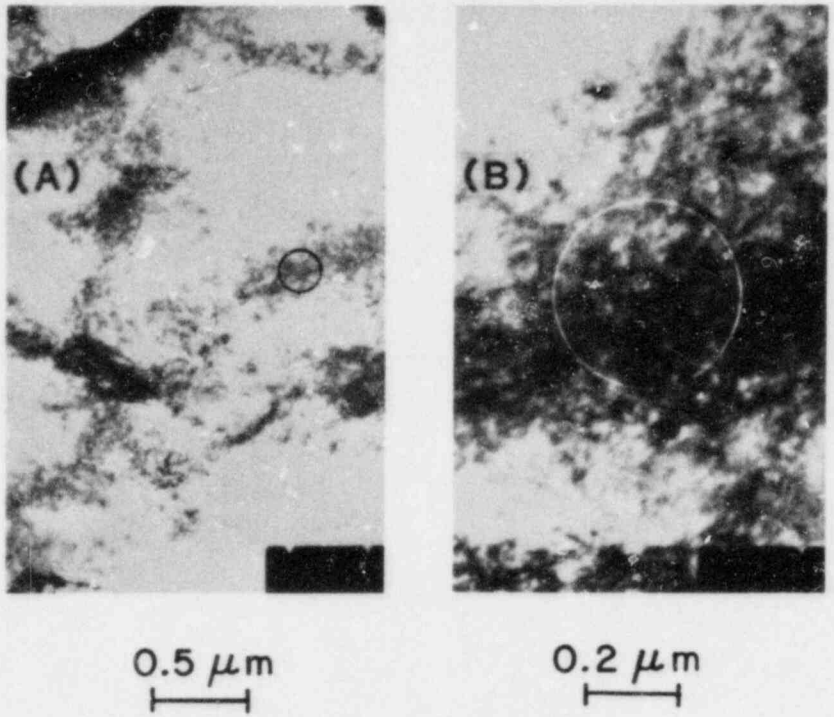

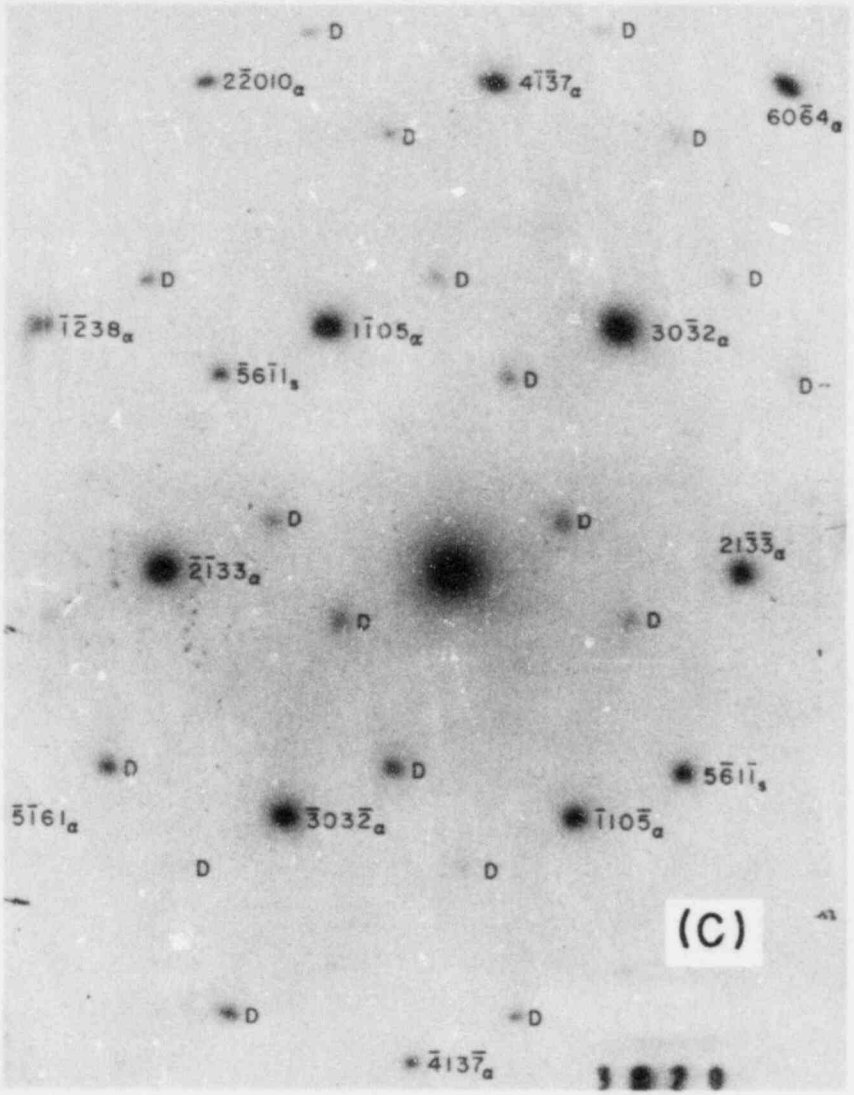

Fig. 43. 1-MeV HVEM Micrographs of a Thin Foil Specimen Obtained from a Region Adjacent to the Failure Site of Big Rock Point Reactor Cladding Specimen 165AG10. (A) Bright-field image of an area; (B) higher magnification of the center of (A); (C) indexed selected area [circled area of (B)] diffraction pattern; (D) dark-field image of the double diffraction of $(5\bar{6}1\bar{1})_{Zr_3O}$ showing Zr_3O phase distribution; and (E) higher magnification of (D). Subscripts α and s and the letter (D) in (C) denote, respectively, reflection from α-Zr, Zr_3O precipitate, and double diffractions.

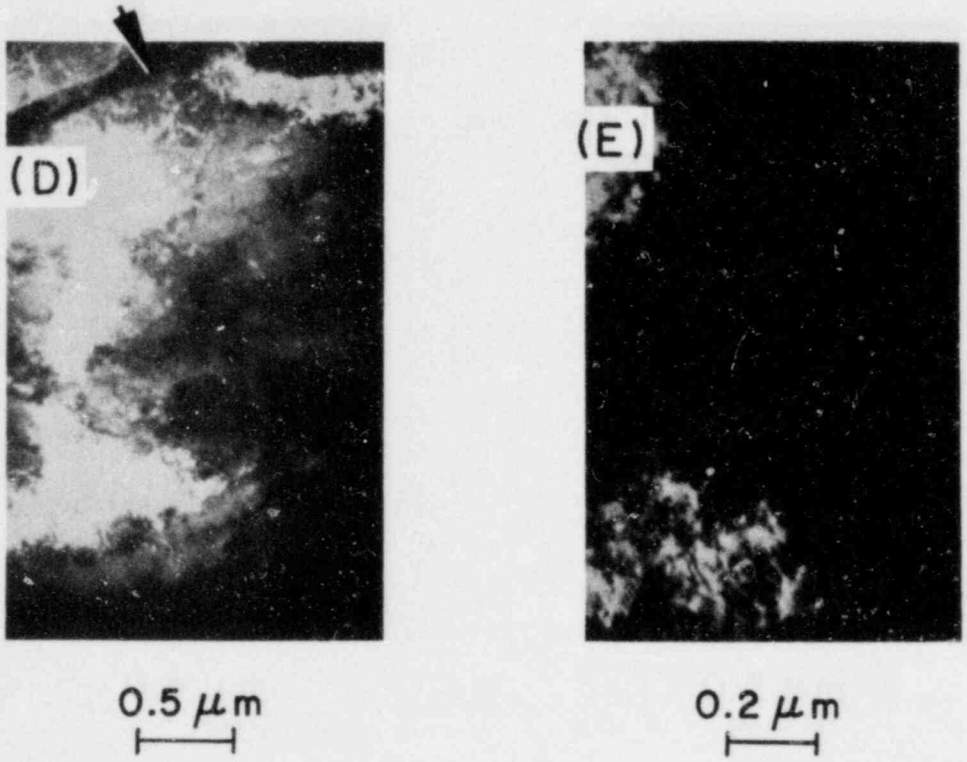

Fig. 43. (Contd.)

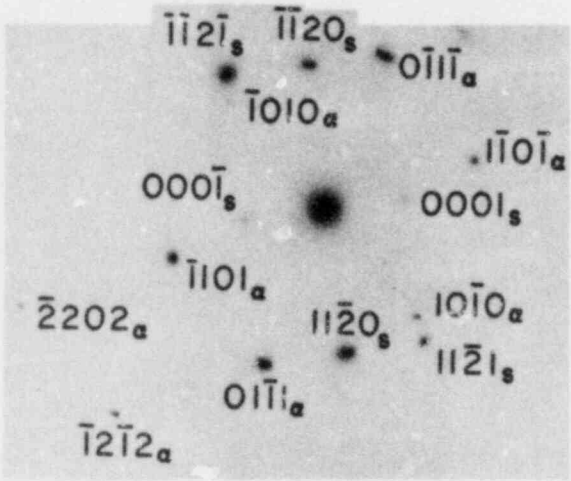

Fig. 44. A Selected Area Diffraction Pattern from a Big Rock Point Reactor Cladding Specimen Showing Zone Axes $[1\bar{2}13]_\alpha$ // $[1\bar{1}00]_{Zr_3O}$ and Planes $(01\bar{1}1)_\alpha$ // $(11\bar{2}1)_{Zr_3O}$. Subscripts α and s denote, respectively, reflections from α-Zr and Zr_3O precipitates.

shown in Fig. 45(C). In the bright-field image of Fig. 45(B), parallel moiré patterns were produced as a result of the strong superposed reflections of $(01\bar{1}1)_{\alpha}$ and $(11\bar{2}\bar{1})_{Zr_3O}$. The measured moiré fringe spacing is about 43.8 Å, and agrees well with the calculated value of 44.64 Å. The spacing can be calculated from the equation

$$D = \frac{d^{Zr_3O}_{11\bar{2}1} \cdot d^{\alpha}_{0111}}{d^{Zr_3O}_{11\bar{2}1} - d^{\alpha}_{01\bar{1}1}} , \tag{58}$$

where the interplanar spacings of $(11\bar{2}1)_{Zr_3O}$ and $(01\bar{1}1)_{\alpha}$ are given by, respectively,

$$d^{Zr_3O}_{11\bar{2}1} = 2.475 \text{ Å and } d^{\alpha}_{01\bar{1}1} = 2.461 \text{ Å}. \tag{59}$$

The bright-field images of Figs. 45(A) and (B) clearly show the morphologies of the Zr_3O phase observed in association with dislocation substructures. Similar morphology can also be observed in the bright- and dark-field images of Fig. 46, which were obtained from near the fracture site of Big Rock Point cladding specimen 165AE4B. In the dark-field images shown in Figs. 46(D) and (E), the morphology of the Zr_3O phase, which resembles small particles approximately 100-200 Å in size, can also be observed. The particle-like morphology of the Zr_3O precipitates strongly indicates that the oxygen atoms were segregated at the irradiation-induced defects of the spent-fuel cladding material.

3. Superlattice Reflections of Zr_3O Phase

The $(5\bar{6}1\bar{1})$ and $(\bar{5}6\bar{1}1)$ superlattice reflections of the Zr_3O phase, shown in Fig. 43(C), are characteristic of this phase. Similar superlattice reflections, produced from scattering by ordered oxygen atoms, have been reported elsewhere.[41] The HVEM micrograph shown in Fig. 47(C) also contains

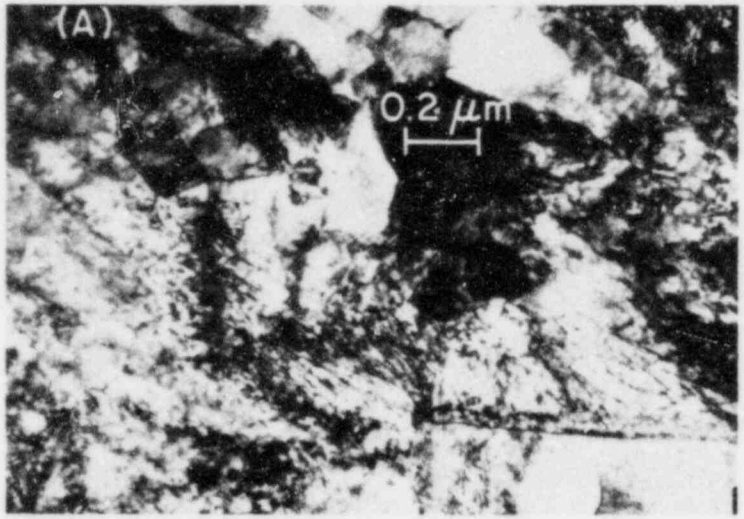

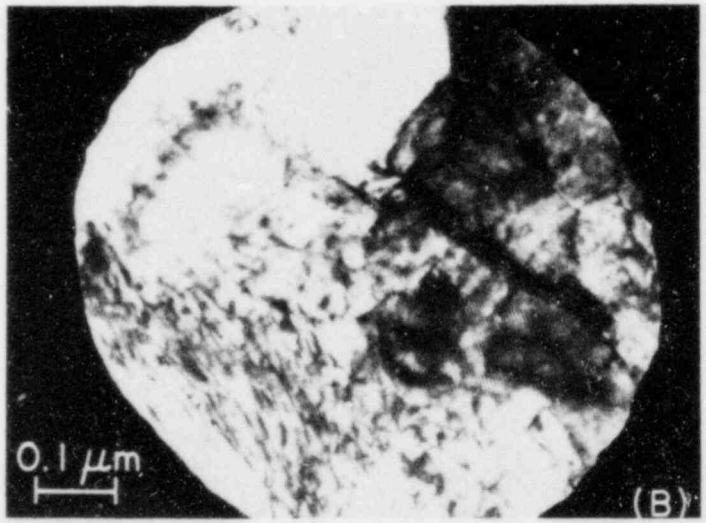

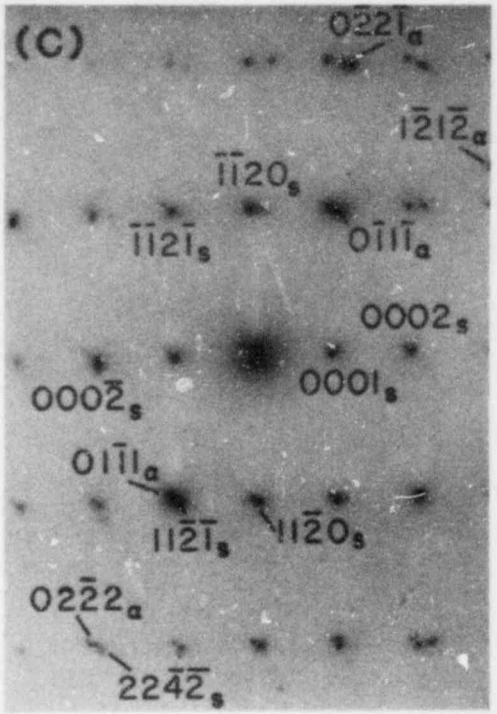

Fig. 45. TEM Micrographs of a Thin Foil Specimen Obtained fror Big Rock Point Reactor Cladding Tube 165AE4A. (A) Bright-field image of an area; (B) higher magnification of a selected area of (A) showing moiré fringes and dislocations; and (C) indexed diffraction pattern of (B) showing strong reflections of $(01\bar{1}1)_\alpha$ and $(11\bar{2}1)_{Zr_3O}$. Subscripts α and s in (C) denote, respectively, reflections from α-Zr and Zr_3O precipitates.

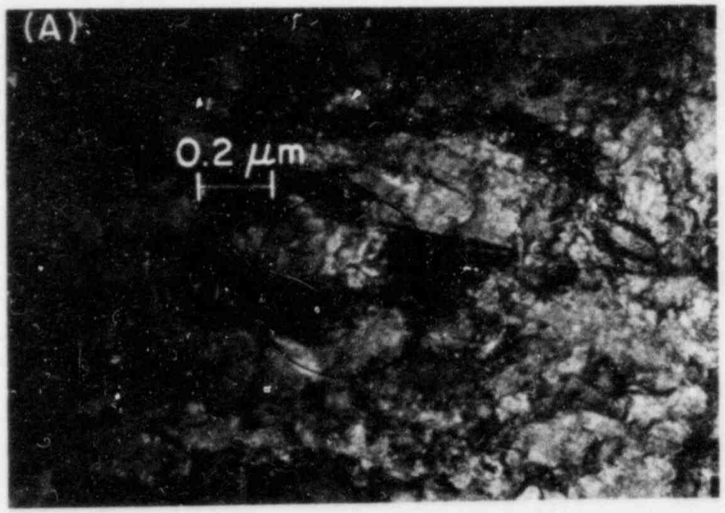

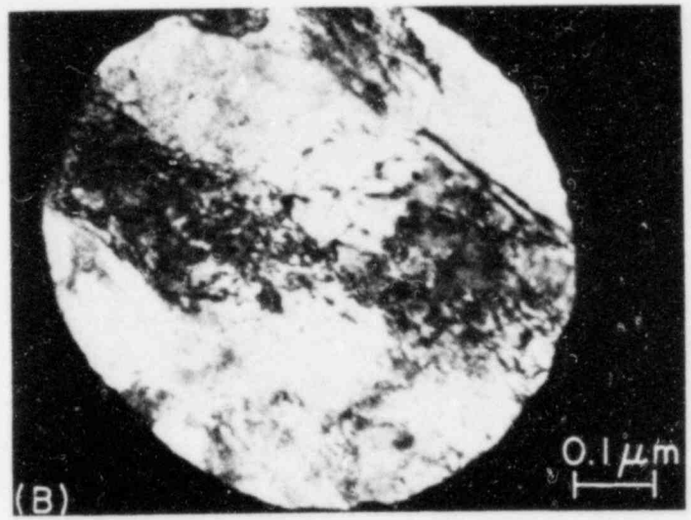

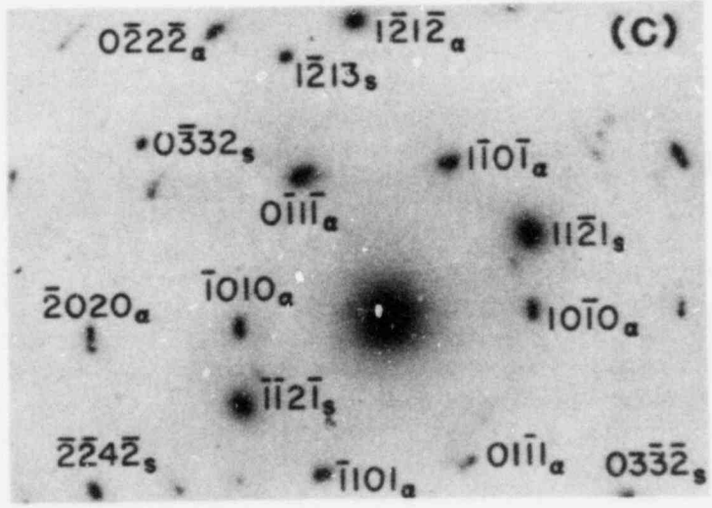

Fig. 46. TEM Micrographs of a Thin Foil Specimen Obtained from Big Rock Point Reactor Cladding Tube 165AE4B. (A) Bright-field morphology of an area; (B) higher magnification of a selected area of (A); (C) indexed diffraction pattern of (B), showing zone axes $[1\bar{2}13]_\alpha$ // $[4\bar{3}\bar{1}\bar{3}]_{Zr_3O}$; (D) dark-field image of $(11\bar{2}1)_{Zr_3O}$, showing small-particle-like morphology of the Zr_3O phase and a dense agglomeration at the center; and (E) higher magnification of the agglomeration of (D), showing dislocation substructures in association with the Zr_3O precipitates. Subscripts α and s in (C) denote, respectively, reflections from α-Zr and Zr_3O precipitates.

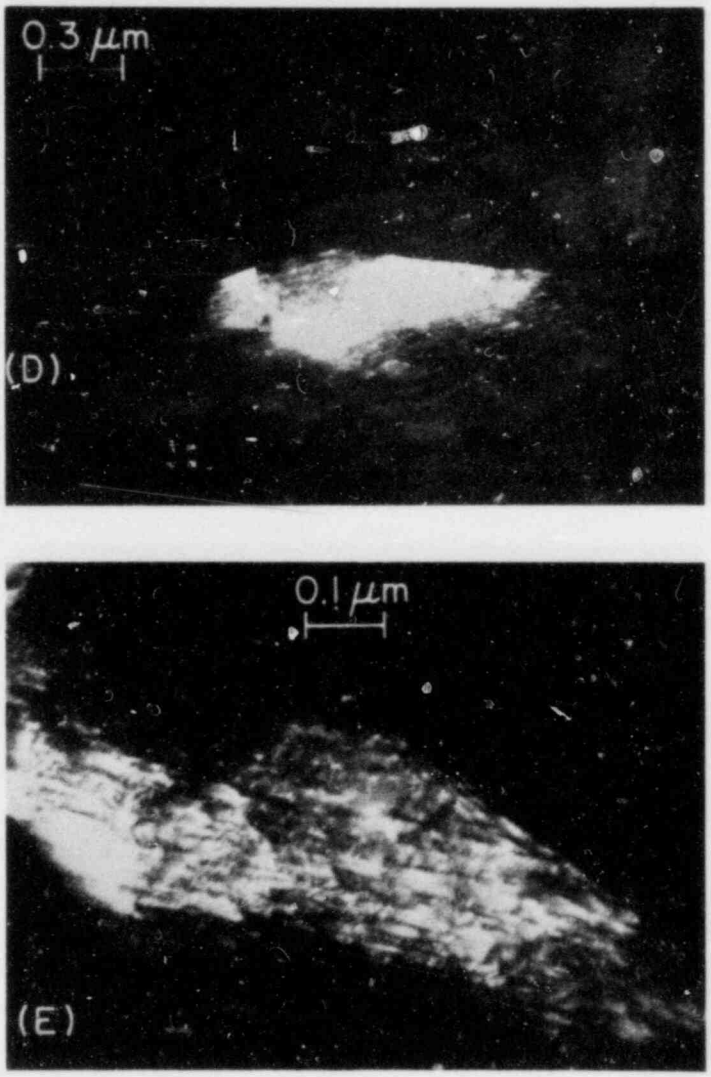

Fig. 46. (Contd.)

many Zr_3O superlattice reflections including $(\bar{2}203)_{Zr_3O}$ and $(31\bar{4}3)_{Zr_3O}$. The scattered amplitudes of the latter reflections[41] consist of an atomic scattering factor of oxygen (f_{ox}) only, and are given by

$$F^*F = 4\left(\cos\frac{\pi}{6}\right)^2 f_{ox}^{\ 2}. \qquad (60)$$

Observation of the superlattice reflections is convincing evidence for the existence of the Zr_3O phase.

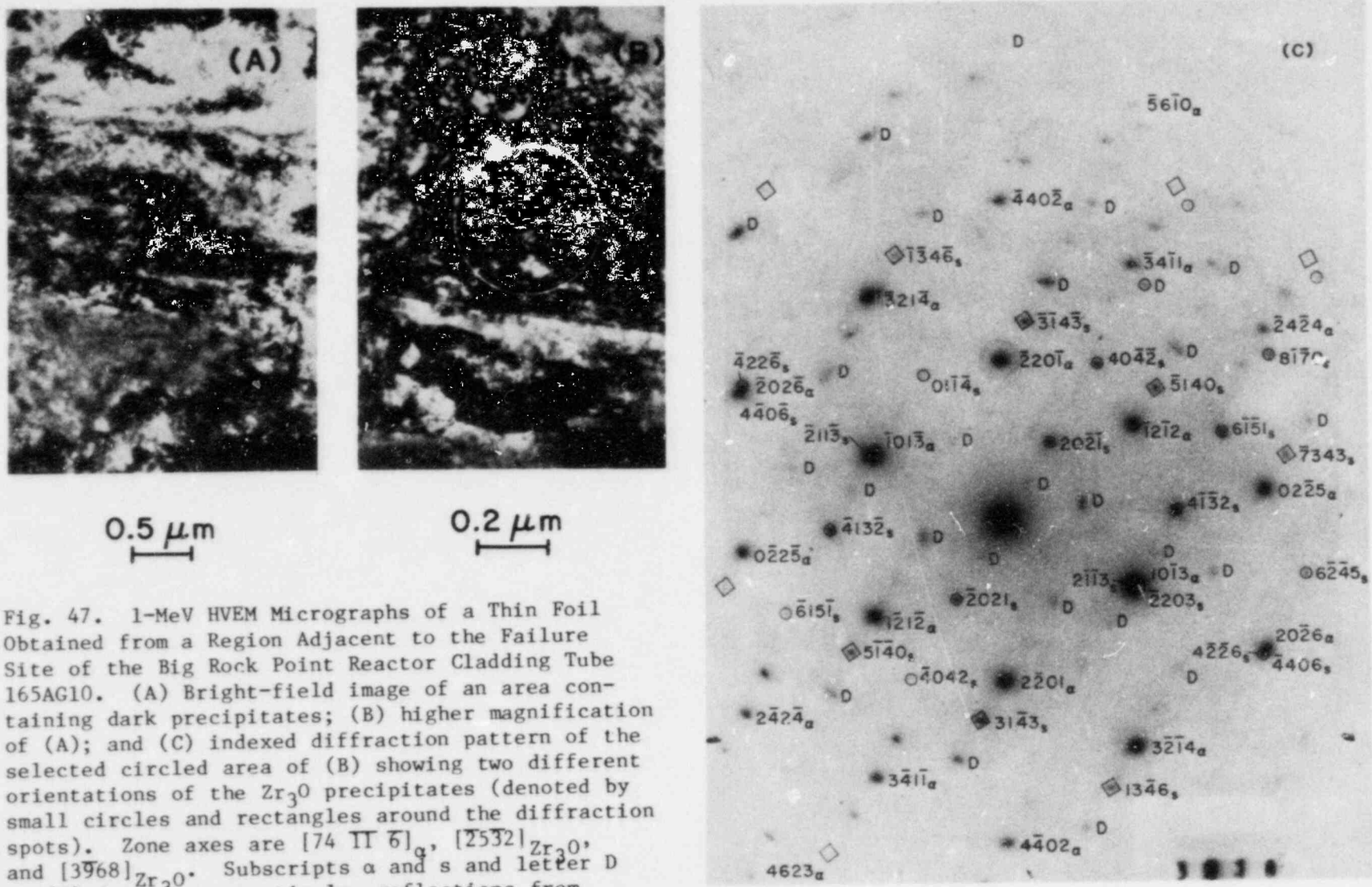

Fig. 47. 1-MeV HVEM Micrographs of a Thin Foil Obtained from a Region Adjacent to the Failure Site of the Big Rock Point Reactor Cladding Tube 165AG10. (A) Bright-field image of an area containing dark precipitates; (B) higher magnification of (A); and (C) indexed diffraction pattern of the selected circled area of (B) showing two different orientations of the Zr_3O precipitates (denoted by small circles and rectangles around the diffraction spots). Zone axes are $[74\ \overline{11}\ 6]_\alpha$, $[\overline{2}532]_{Zr_3O}$, and $[3\overline{9}68]_{Zr_3O}$. Subscripts α and s and letter D in (C) denote, respectively, reflections from α-Zr, Zr_3O precipitates, and double diffraction.

4. Discussion

The common observation of the Zr_3O phase in association with dislocation substructures and cell walls indicates that the phase was formed through segregation of oxygen atoms (present in the cladding either as an intrinsic alloying element or as extrinsic corrosion-product impurities) near the dislocation substructure. In some cases, an individual dislocation decorated by a second phase could be observed in high-magnification dark-field contrast. The reciprocal lattice points, from which the dark-field images [e.g., Fig. 43(D)] of the second phase were formed, were consistent with the Zr_3O structures, which indicates that the individual dislocations were decorated by the Zr_3O phase. The morphology of the Zr_3O phase observed in association with dislocations [i.e., Figs. 45(B) and 46(E)] is consistent with the model of strain aging which is attributed to migration of oxygen atoms and interaction with dislocations.[42-44] In this regard, one would expect to be able to identify the Zr_3O phase from a similar TEM-HVEM analysis of unirradiated Zr-O alloys that were strain aged at about 320°C. Veevers and Snowden[45] reported bright-field TEM images from such specimens, similar to what was observed in this investigation and subsequently identified as a Zr_3O phase. However, an analysis of corresponding diffraction patterns from the images was not reported in their study. The morphology of the Zr_3O phase, observed in association with dislocation substructures, and the lack of slip dislocations indicate that the brittle-type failures observed in the present investigation were produced essentially as a result of segregation of the oxygen atoms, which subsequently led to formation of an ordered phase between Zr and oxygen, immobilization of dislocations, and minimal plastic deformation.

However, transmission electron micrographs obtained for test specimens of unirradiated Zr alloys subjected to strain aging[42,44,45] indicate that it is unlikely that all the dislocations could be immobilized and prevented from breaking out of the cellular substructures of stress-relieved material by the mechanism of oxygen segregation alone. Accordingly, some dislocations should be operable, and ductile fracture would be expected in such specimens. However, in similar specimens containing high-density irradiation-induced damage, breakout and glide of dislocations may be more difficult because the defects may act as an extra barrier. Such a situation would be more conducive

to brittle-type fracture if the irradiation-induced defects were of sufficiently high density. Another possibility is a hitherto unknown synergistic effect involving the oxygen interstitials and irradiation-induced defects in the spent-fuel cladding. The small-particle-like morphology of the Zr_3O precipitates, discussed in association with Fig. 46, indicates a segregation and enrichment of oxygen at the irradiation-induced defects and subsequent formation of Zr_3O particles. The irradiation-induced formation of the Zr_3O phase is similar to segregation of oxygen interstitials to irradiation-induced defects reported in association with the radiation-anneal hardening phenomenon of Nb[46,47] and V[48-50]. Once oxygen atoms are segregated to the defects and Zr_3O precipitates are formed, the irradiation-induced defects will be strengthened as barriers to slip dislocations, and consequently, plastic deformation will be less likely.

During irradiation of the Zircaloy cladding in a reactor, vacancies as well as interstitials are produced in cascades. This in turn produces local vacancy and interstitial concentration gradients on a microscopic scale in the materials. Consequently, local mass transport can occur on a microscopic scale via vacancy as well as interstitial fluxes in the material. Although no changes occur on a macroscopic scale, local material components (i.e., ratio of solute to matrix atoms) can be altered. Preferential exchange of some substitutional alloying element with vacancies can occur, and this leads to a preferential flow of the element in the direction opposite that of vacancy flow. Strong binding between a solute atom and vacancies causes a "dragging" of the solute element in the direction of the vacancy flow. The flow of interstitials produced by irradiation can also induce solute segregation.[51] Because of their smaller atomic weight, undersized solute atoms (such as oxygen in Zircaloy) are likely to be knocked out of their positions by fast neutrons more easily than the matrix atoms. Subsequently, the undersized solute atoms are accommodated more readily in interstitial sites than are oversized or matrix atoms. Hence, the fraction of undersized solute atoms among irradiation-produced interstitials will be greater than average in the overall material. This will cause the ratio of undersized solute atoms (e.g., O) to matrix atoms (e.g., Zr) comprising the interstitial flux to exceed the ratio of the average concentration; this results in enrichment of the undersized solute atoms near the point defect sinks.[51] On the contrary,

oversized solute atoms will be preferentially accommodated in substitutional sites and will, therefore, tend to be depleted from defect sinks by vacancy flow. The competing transport of any given solute atoms via the interstitial flux to the defect sink and via the vacancy flux away from the sink has been treated by Wiedersich et al.[52] They showed that the enrichment of solute atoms occurs at the sinks when the preferential transport of the solute atoms via interstitial flux outweighs that via vacancy flux. Maximum enrichment occurs when the solute atoms (e.g., oxygen in α-phase Zircaloy) diffuse exclusively via an interstitial mechanism. Oxygen diffusion in α-Zr has been critically reviewed recently by Ritchie and Atrens,[53] and for 290-650°C, the diffusion is attributed to rate-controlling jumps of oxygen interstitials to nearest-neighbor interstitial sites on the basal plane; i.e., the oxygen diffuses via an interstitial mechanism. Therefore, according to the model of Wiedersich et al.,[52] segregation of oxygen is predicted to occur to irradiation-induced defect sinks in Zircaloy fuel cladding. This prediction is in agreement with the TEM-HVEM observation reported in this investigation.

IV. LONG-TERM EMBRITTLEMENT OF CAST DUPLEX STAINLESS STEELS IN LWR SYSTEMS

Principal Investigators:
O. K. Chopra, G. Ayrault, and W. J. Shack

A. Introduction

Cast duplex stainless steels are used extensively in the nuclear industry to fabricate pump casings, valve bodies, and piping in LWRs. The ferrite phase in the duplex austenitic-ferritic structure increases the tensile strength and improves the weldability, stress corrosion resistance, and soundness of castings of these steels. However, the precipitation of additional phases within the ferrite phase of the cast stainless steels leads to variability in properties, increased susceptibility to σ-phase embrittlement at high temperatures, and degradation of mechanical properties at low temperatures owing to a phenomenon known as "475°C embrittlement" which is associated with the temperature of maximum embrittlement.

At temperatures below 500°C, embrittlement of the duplex stainless steels is attributed to the precipitation of an α' phase in the iron-rich α matrix. Recent investigations of the aging behavior of CF-8 and -8M cast duplex stainless steels show substantial reductions in room temperature impact strength after 10,000 to 70,000 h at temperatures as low as 300°C.[54-56] The ferrite content of the cast structure has a pronounced influence on the embrittlement behavior. For example, at the operating temperature of LWRs, i.e., 316°C, the impact energy of cast structures will decrease below 40 J (~30 ft-lb) after ~19 yr of service for structures containing about 14% ferrite and after only 3 yr of service for those containing 40% ferrite.

In the temperature range of 300 to 400°C, the data[54] yield an activation energy of 24,000 cal/mole, a value that is much lower than expected for a mechanism controlled by solute bulk diffusion. These results suggest that the precipitation process may be controlled by another mechanism, e.g., spinodal decomposition, or that processes other than a' precipitation contribute to embrittlement. The available information on the microstructure of aged, cast duplex SS is not sufficient for correlating the microstructure with the mechanical properties or for determining the mechanism of low-temperature

embrittlement. Changes in composition of cast duplex SS also influence the aging behavior and add to the uncertainty of predicting the long-term embrittlement behavior.

The objectives of this program are to (1) characterize and correlate the microstructure of in-service reactor components and laboratory-aged material with loss of fracture toughness and identify the mechanism of embrittlement, (2) determine the validity of laboratory-induced embrittlement data to predict the toughness of component materials after long-term aging at reactor operating temperatures, (3) characterize the loss of fracture toughness in terms of fracture mechanics parameters in order to provide the data needed to assess the safety significance of embrittlement, and (4) provide additional understanding of the effects of key compositional and metallurgical variables on the kinetics and degree of embrittlement.

B. Technical Progress

1. Material Procurement

Nineteen different heats of stainless steel cast material, ASTM A-351 grades CF-8, -8M, and -3, have been obtained in the form of keel blocks from ESCO Corporation. The chemical compositions of the various heats are given in Table XIV. The composition of the heats was varied to provide different concentrations of nickel, chromium, carbon, and nitrogen in the material and ferrite contents in the range of 3 to 30%. Sections from five different centrifugally cast pipes (grades CR-8 and 8M), a pump impeller, and a pump casing (grade CF-8) were also procured. The commercial castings provide a range of chemical composition, microstructure, and ferrite content, as well as cast shapes and sizes. The OD and wall thickness of the cast pipes range from 0.6 to 0.9 m and 38.1 to 76.2 mm, respectively. Detailed drawings and a schedule for cutting the pieces of cast components and the keel blocks are being prepared to obtain blanks for Charpy impact and compact-tension specimens.

It is expected that this range of materials will encompass virtually all those materials encountered in reactor service. The testing will emphasize materials obtained from actual reactor components. The nineteen

TABLE XIV. Chemical Compositions of the Experimental Heats of Cast Stainless Steel[a]

Heat Number	Grade	Composition, wt %							Ferrite Content,[b] %
		Mn	Si	Mo	Cr	Ni	N	C	
61953	CF-8	0.70	1.28	0.35	19.62	8.86	0.045	0.07	7.8
61958		0.66	1.21	0.29	19.56	10.37	0.040	0.05	4.5
61957		0.69	1.24	0.28	18.45	8.94	0.041	0.06	4.7
61959		0.63	1.14	0.26	20.35	8.95	0.040	0.07	9.9
61961		0.70	1.20	0.27	20.54	8.59	0.060	0.06	12.1
61960		0.71	1.01	0.26	21.02	8.07	0.050	0.07	16.9
61956		0.60	1.16	0.30	19.33	8.93	0.031	0.06	8.1
61954		0.58	1.08	0.31	19.42	8.91	0.073	0.065	5.3
62047	CF-8M	0.71	0.60	2.36	19.41	9.13	0.030	0.06	17.9
61963		0.69	0.75	2.52	19.39	11.22	0.030	0.05	9.1
61962		0.84	0.64	2.46	18.38	11.35	0.030	0.07	4.2
61965		0.66	0.63	2.53	20.95	9.39	0.060	0.6	22.3
61964		0.70	0.71	2.41	20.87	9.01	0.030	0.05	32.2
61952	CF-3	0.63	1.04	0.31	19.51	9.07	0.049	0.021	10.9
61949		0.66	1.11	0.29	19.32	10.10	0.064	0.022	5.1
61950		0.67	1.26	0.28	17.83	8.84	0.064	0.019	4.4
61951		0.66	1.06	0.28	20.36	8.69	0.048	0.023	17.5
61947		0.65	1.23	0.45	19.67	10.04	0.027	0.018	10.2
61948		0.67	1.21	0.26	19.42	9.90	0.071	0.016	6.0

[a]Keel blocks, approximately 203 mm long x 127 tall with the third dimension tapered from 63 mm to 36 mm.

[b]Calculated from composition with Hull's equivalent factor.

experimental heats will be used as needed to ensure that the relevant range of variables is, in fact, covered, or in cases where careful control of one variable (e.g., composition) is needed to investigate the effect of another variable (e.g., temperature and time of aging). Material will be available for Charpy impact tests and microstructural studies over the entire range of compositions. However, it is prohibitively expensive to procure and age material for J_R curve testing for all compositions. A more restricted set of compositions will be chosen for these tests, e.g., compositions corresponding to heats 61953, 60, 54, 47, 65, and 51. The material for these tests will be obtained from ~2000-lb laboratory heats in the form of 76-mm-thick slabs. The large experimental heats will be used to fabricate 2T compact-tension specimens for J_R curve testing and Charpy impact specimens for evaluating the ductile-to-brittle transition temperature (DBTT).

Facilities for conducting long-term aging of cast material for Charpy impact and compact-tension specimens are being assembled. Preliminary tests were carried out to determine the temperature gradient in the furnaces and the accuracy of temperature control. The furnaces were lined with steel shells to increase the furnace heat capacity and to increase the size of the uniform-temperature zone. The cast material will be aged at 450, 400, 350, 320, and 290°C for up to 50,000 h.

2. Microstructural Evaluation

The initial experimental effort is focused on microstructural studies on cast duplex stainless steels aged at low temperatures for long times. Twenty fractured Charpy impact bars from three heats of aged cast duplex stainless steel (grades CF-8 and CF-8M) were obtained from George Fisher, Ltd. of Switzerland. The material was used earlier to study the long-term aging behavior of cast stainless steels.[54] The specimens from CF-8 cast stainless steel (heats 278 and 280) were aged for 3000, 10,000, and 70,000 h at 300, 350 and 400°C, while the specimens from CF-8M stainless steel (heat 286) were aged for 1000 and 10,000 h at 400°C.

Two ferritic alloys, heats 26-1S and 29-4-2, and a cast duplex stainless steel (heat B) were used to develop the technique for preparing

transmission electron microscope (TEM) samples from the cast materials. The ferritic alloys were supplied by Allegheny Ludlum Steel Corp., and have been used in a study of the "475°C embrittlement" phenomenon at temperatures between 371 and 593°C.[4] The chemical compositions of the various steels used for metallographic examination are given in Table XV. Material from the two ferritic alloys and cast stainless steel (heat B) was aged for 100 and 1000 h at 400 and 475°C for TEM inspection.

TABLE XV. Chemical Compositions of Steels Used for Microstructural Evaluation

Designation		Composition, wt %									Ferrite Content, %	
Heat	Grade	Mn	Si	Mo	Cr	Ni	P	S	N	C	Calc.[a]	Meas.
						Cast Stainless Steel						
B	CF-8A	0.89	1.34	0.52	21.13	8.44	0.019	0.014	0.165	0.046	9.2	-
278[b]	CF-8	0.28	1.00	0.13	20.20	8.27	0.008	0.019	0.027	0.038	19.00	15
280[b]	CF-8	0.50	1.37	0.25	21.60	8.00	0.015	0.006	0.029	0.028	38.7	38
286[b]	CF-8M	0.40	1.33	2.44	20.20	9.13	0.044	0.015	0.063	0.072	18.8	22
						Ferritic Steel						
26-1S	-	-	-	0.97	26.0	0.14	-	-	0.019	0.030	-	-
29-4-2	-	-	-	3.90	29.6	2.20	-	-	0.011	0.006	-	-

[a]Calculated from composition with hulls equivalent factor.
[b]Heats obtained from George Fisher, Ltd.

3. Sample Preparation

Work on sample preparation techniques has reached a stage where TEM foils from cast duplex stainless steels and the ferritic alloys can be produced routinely with a high success rate (>90%). Samples are prepared from bulk material by first cutting 0.75-mm wafers with an Isomet low-speed saw, and then grinding and mechanically polishing the wafers to 0.25-mm thickness. TEM disks 3 mm in diameter are punched from the wafer. The disks are then sequentially electropolished from both sides with a South Bay Technology model 550 single-jet polisher until perforation of the disks occurs.

Jet polishing is the only problematic step. Both the austenite and ferrite phases in A351 cast duplex stainless steels were found to polish well under a broad range of conditions, i.e., in a variety of electrolytes with different polishing potentials, temperatures, and electrolyte flow rates. However, it was found that matrix/inclusion interfaces in both the austenite

and ferrite phases were attacked preferentially under almost all polishing conditions. This often caused inclusions to fall out, leaving large holes (5 to 50 mm) with no surrounding sample area thin enough for TEM inspection. Thus, a major consideration in optimizing the polishing conditions was reduction of the preferential attack to as low a level as possible. The other major consideration was adjustment of the relative rate of attack on the austenite and ferrite phases. Uniform attack on both phases was rare. The more rapidly attacked phase is penetrated first and predominates in thin areas. Since low-temperature embrittlement is known to be caused by the ferrite phase, the polishing conditions were optimized so that most thin areas were in the ferrite phase.

An important factor in this optimization was the choice of polishing solution. Three polishing solutions that have proved especially successful for TEM sample preparation were tried: (1) 10% perchloric acid in acetic acid, (2) 20% sulfuric acid in methanol, and (3) a 17% perchloric acid, 19% ethanol, 27% butyl cellosolve, 37% water solution.

The perchloric/acetic acid polish (solution 1) consistently attacked the ferrite phase more strongly than the austenite and often produced a good ferrite thin area. However, preferential attack at inclusions was strong under most conditions and premature foil penetration at inclusion sites was common. Low polishing potentials (~20 V) coupled with low electrolyte flow rates significantly reduced the preferential attack and yielded an acceptable success rate. Additions of varying amounts of butyl cellosolve and glycerol to the perchloric/acetic acid solution did not improve the results. All polishing with perchloric/acetic acid solutions was done at room temperature.

The sulfuric acid/methanol polish (solution 2) was also tried with varying amounts of butyl cellosolve and ethylene glycol, and with variations in the sulfuric acid concentration; these alterations did not prove helpful. Under most conditions, these solutions attacked the austenite phase more readily than the ferrite phase and usually produced an austenite thin area. Attack on the inclusion/matrix interphase was less severe than for the perchloric/acetic acid solutions. The relative degree of attack on the austenite and ferrite phases could be equalized and finally reversed at low polishing potentials (between 10 and 20 V) and low electrolyte flow rates.

These conditions, however, often produced fine pitting of the ferrite. Optimum polishing conditions with the sulfuric acid/methanol solutions were achieved at temperatures between -30 and -70°C, but polishing was very slow at the low voltages employed. The solution had to be changed often to maintain good results.

Solution 3, described by Solomon and Levinson,[58] produced the best results with a high rate of success (>90%). This solution preferentially attacked the ferrite phase at polishing potentials between 20 and 30 V and produced TEM samples with good ferrite thin areas. Polishing temperatures were maintained in the range of -20 to -30°C.

4. Microstructure of Aged Cast Duplex Stainless Steel

Aging of the cast duplex stainless steel, heat B, at 475°C for 1000 h produced two types of precipitates in the ferrite phase - a general precipitate that is distributed uniformly in the ferrite phase and another type that is found only on the dislocations. The general precipitate had a mottled or "orange peel" appearance in bright-field images, as shown in Fig. 48(A), but produced no detectable changes in diffraction pattern. This precipitate is believed to be the α' phase. The TEM images generally confirm the presence of the α' phase in ferrite alloys[57,59,60] and duplex stainless steels.[56,58] However, the contrast mechanism for imaging α' is not well established. Stereo microscopy on the features shown in Fig. 48(A) revealed a great deal of contrast near the sample surface. This contrast most likely arises from thickness variation produced by differential thinning of the α' phase and the ferrite matrix during sample preparation.[56,61] The stereo pairs also show contrast from the sample interior. This is generally assumed to result from strain contrast due to α'-α lattice mismatch, but this has not been clearly demonstrated in any study of α' precipitation.

The precipitates observed on dislocations in the cast stainless steels produced distinct diffraction spots well away from the matrix reflections, and this shows that the precipitates are not α'. These precipitates were easily imaged in a dark field, as shown in Fig. 48(B). The diffraction pattern for the precipitates is shown in Fig. 49. Although there appears to

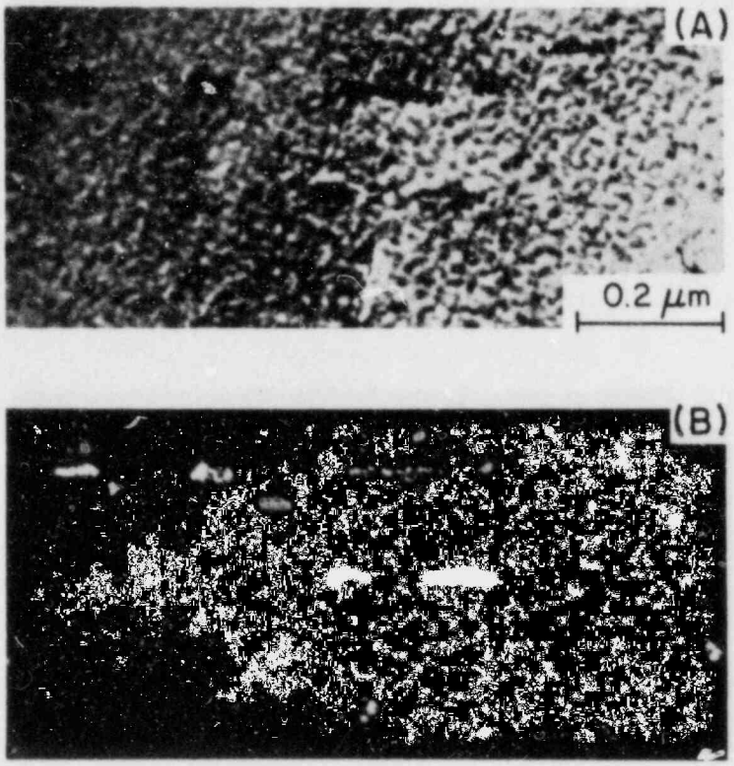

Fig. 48. Ferrite in A351 CF-8A Cast Duplex Stainless Steel Aged for 1000 h at 475°C. (A) Bright-field image showing mottled background due to α', and precipitates on dislocations; (B) dark-field image showing precipitates on dislocations.

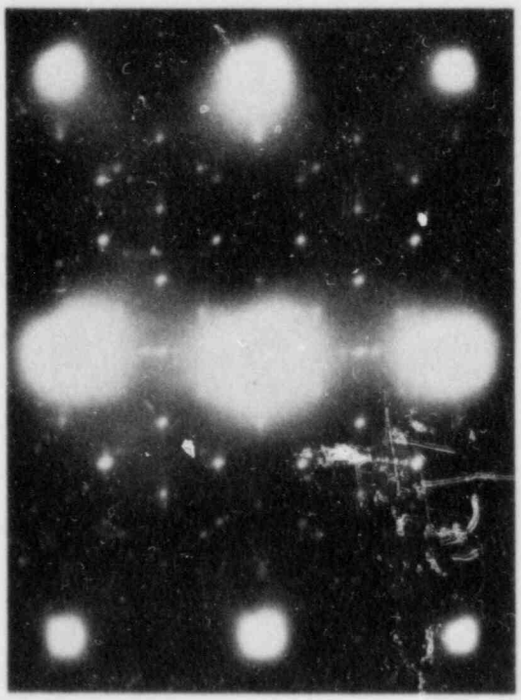

Fig. 49
Diffraction Pattern at (011) Orientation in Ferrite Phase of A351 CF-8A Cast Duplex Stainless Steel Aged for 1000 h at 475°C. The complex pattern of weak spots is due to precipitates that formed on dislocations.

be only one orientation variant (i.e., all diffraction spots produce images of all the precipitates), the diffraction pattern is complex and the phase has not been identified. Positive identification of the phase would probably require extraction of the precipitates from the matrix.

TEM work on the aged cast stainless steel specimens obtained from George Fisher, Ltd. was initiated with the CF-8 specimen that was aged at 400°C for 10,000 h. The most striking feature was of precipitates that formed at the dislocations, shown in Fig. 50. These precipitates were not observed in the "control" specimens aged at 300°C for 3000 h. The precipitates produced diffraction spots well away from the matrix reflections, indicating that the precipitates are not α'. However, the diffraction patterns were

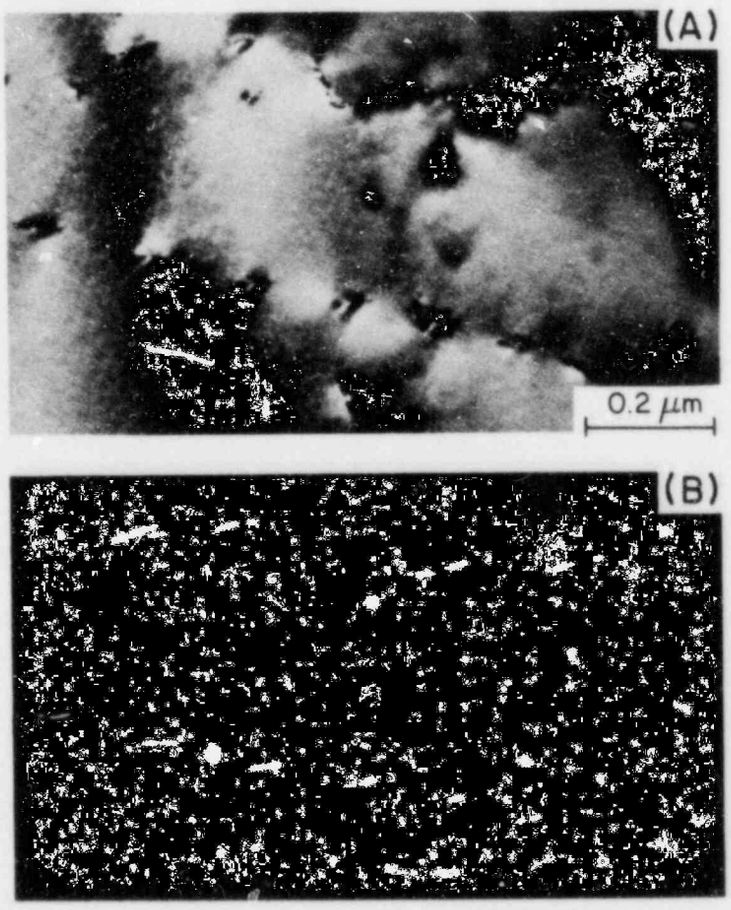

Fig. 50. Ferrite in A351 CF-8 Cast Duplex Stainless Steel Aged for 10,000 h at 400°C. (A) Bright-field image; (B) dark-field image showing precipitates on dislocations.

quite different from the ones observed earlier in the duplex stainless steel aged for 1000 h at 475°C. Figure 50 also shows a mottled structure of very fine texture in the bright-field image. This is probably due to a surface etching artifact unrelated to α' precipitation. A similar structure was also observed in the "control" specimen aged at 300°C for 3000 h, where α' precipitation is unlikely to occur.

5. Microstructure of Aged Ferritic Alloys

The microstructural observations for the aged ferritic alloys were essentially identical to those reported by Nichol et al.[57] Figure 51 shows the bright-field images of 29Cr-4Mo-2Ni and 26Cr-1Mo steels aged at 475°C for 1000 h. Both steels exhibit a mottled structure usually attributed to α' formation. The 29Cr-4Mo-2Ni steel also showed platelet precipitates on {100} planes. A comparison of 29Cr-4Mo-2Ni specimens aged at 475°C and 400°C (Fig. 52) shows that platelets form at both temperatures in this alloy; the

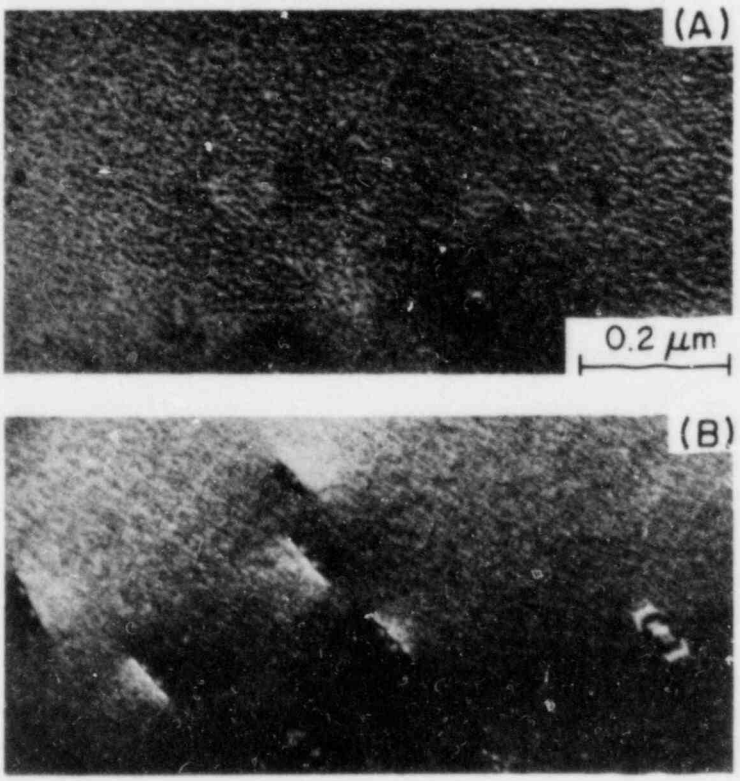

Fig. 51. Ferritic Steels Aged for 1000 h at 475°C.
(A) 29Cr-4Mo-2Ni; (B) 26Cr-1Mo.

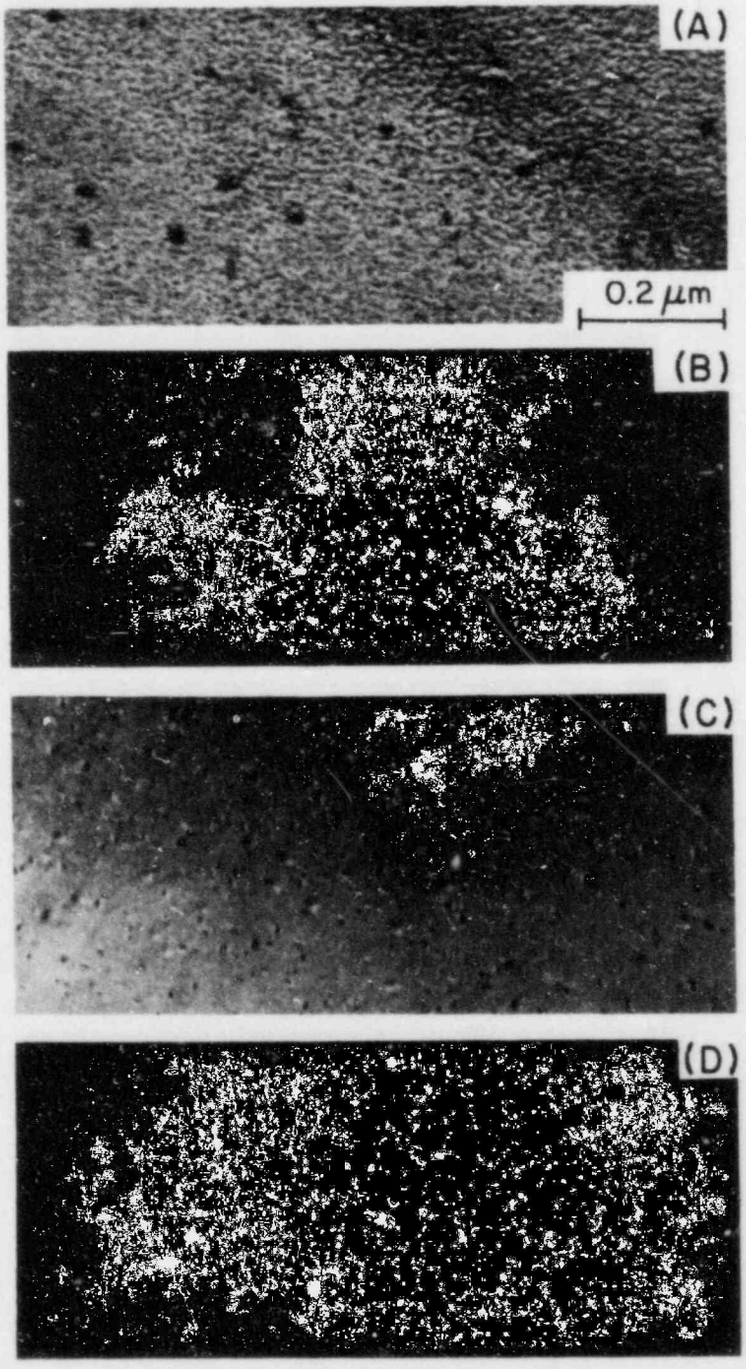

Fig. 52. 29Cr-4Mo-2Ni Aged for 1000 h at 400 and 475°C. (A) 475°C (bright field); (B) 475°C (dark field); (C) 400°C (bright field); (D) 400°C (dark field).

platelets formed at 400°C are smaller and higher in number density than those formed at 475°C. The platelet precipitates in 29Cr-4Mo-2Ni steel produced strong strain-field images in bright-field micrographs [Figs. 52(A) and 52(C)]. The platelets caused streaking of the ferrite diffraction spots, and the streaks were used to form the dark-field images presented in Figs. 52(B) and 52(D). Similar platelet precipitates were reported in 21Cr-0.02C-0.02N alloy aged at 475°C,[62] 22Cr-0.04N alloys aged at 500°C,[63] and 26Cr-5Ni-1Mo steel aged at 500°C.[64] Since the latter is close to the composition of the ferrite phase in CF-8M cast duplex stainless steel, the formation of platelet precipitates is anticipated in aged duplex stainless steels.

Most investigators[57,62,64] have interpreted the platelets as α' precipitates. However, Hendry et al.[63] have rejected this notion, noting that the α' precipitates have a very small lattice misfit with the α matrix (~0.5%) and should not form as platelets; they interpreted the platelets as chromium-nitrogen G. P. zones. The present results for 29Cr-4Mo-2Ni steel aged at 400°C also suggest that the platelets are not α'. Dark-field micrographs showed that the platelets were typically $\lesssim$5 nm in diameter and $\lesssim$2 nm thick after 1000 h at 400°C. Image contrast calculations performed for the Cu-Co system, where lattice mismatch is three times larger than in the α-α' system, show that spherical Co inclusions in Cu should not be visible until they are at least 5 nm in diameter.[65] Thus, it is highly unlikely that precipitates as small as those in Fig. 52(D) could produce the strong strain contrast visible in Fig. 52(C) if they were α'. Unfortunately, the streaked diffraction patterns provide little information for identification of the platelets. Furthermore, there is no evidence suggesting that these platelets are related to the precipitates formed on dislocations in the duplex stainless steels. The platelets in the ferritic steels are regarded as a third "non-α'" precipitate which is likely to form during long-term aging of cast stainless steel.

REFERENCES

1. C. K. W. Tami, Intensity Spectrum and Directivity of Turbulent Boundary Layer Noise, J. Acoust. Soc. Am. 57, 25 (1975).

2. J. R. Smith, G. V. Rao and R. Gopal, "Acoustic Monitoring for Leak Detection in Pressurized Water Reactors," in Acoustic Emission Monitoring of Pressurized Systems, ASTM STP 697, American Society for Testing and Materials, Philadelphia (1979), pp. 177-204.

3. D. S. Kupperman, R. N. Lanham, T. N. Claytor, and R. Groenwald, in Materials Science Division Light-Water-Reactor Safety Research Program: Quarterly Progress Report, April-June 1982, NUREG/CR-2970 Vol. II, ANL-82-41 Vol. II (May 1983), pp. 2-14.

4. V. Cihal, Intercrystalline Corrosion of Corrosion Resistant Steels, Zashch. Met., 4(6), 637-655 (1968).

5. J. Y. Park, in Environmentally Assisted Cracking in Light Water Reactors: Annual Report, October 1981-September 1982, NUREG/CR-3292, ANL-83-27 (February 1983), pp. 23-29.

6. W. J. Shack et al., Environmentally Assisted Cracking in Light Water Reactors: Critical Issues and Recommended Research, NUREG/CR-2541, ANL-82-2 (February 1982).

7. W. L. Clarke, The EPR Method for the Detection of Sensitization in Stainless Steels, NUREG/CR-1095, GEAP-24888 (April 1981).

8. J. Y. Park and W. J. Shack, in Materials Science and Technology Division Light-Water-Reactor Safety Research Program: Quarterly Progress Report, October-December 1982, NUREG/CR-2970 Vol. IV, ANL-82-41 Vol. IV (November 1983), pp. 32-36.

9. F. P. Ford, A Mechanism of Environmentally Controlled Crack-Growth of Structural Steels in High-Temperature Water, General Electric Co. Report 81-CRD-125 (August 1981).

10. P. M. Scott and A. E. Truswell, "Corrosion Fatigue Crack Growth in Reactor Pressure Vessel Steels in PWR Primary Water," in Aspects of Fracture Mechanics in Pressure Vessels and Piping, PVP Vol. 58, American Society of Mechanical Engineers, New York (1982), pp. 271-301.

11. J. R. Rice, "Mechanics of Crack Tip Deformation and Extension by Fatigue," in Fatigue Crack Propagation, ASTM STP 415, American Society for Testing and Materials, Philadelphia (1967), pp. 247-309.

12. P. S. Maiya and W. J. Shack, in Environmentally Assisted Cracking in Light Water Reactors: Annual Report, October 1981-September 1982, NUREG/CR-3292, ANL-83-27 (February 1983), pp. 35-65.

13. D. T. Powell and J. C. Scully, Stress Corrosion Cracking of Alpha Titanium Alloys at Room Temperature, Corrosion 24, 151 (1968).

14. R. N. Parkins, "Development of Strain-Rate Testing and Its Implications," in Stress Corrosion Cracking: the Slow-Strain-Rate Technique, ASTM STP 665, American Society for Testing and Materials, Philadelphia (1979), p. 5.

15. H. Takaku, M. Tokiwai, and H. Hirano, Effects of Cyclic Tensile Loading on Stress Corrosion Cracking Susceptibility for Sensitized Type 304 Stainless Steel in 290C High Purity Water, Corrosion 35(11), p. 523 (1979).

16. M. Takano, Effect of Strain Rate on Stress Corrosion Cracking of Austenitic Stainless Steel in $MgCl_2$ Solutions, Corrosion 30(12), 441 (1974).

17. P. S. Maiya and W. J. Shack, in Materials Science and Technology Division Light-Water-Reactor Safety Research Program: Quarterly Progress Report, October-December 1982, NUREG/CR-2970 Vol. IV, ANL-82-41 Vol. IV (November 1983), pp. 36-48.

18. F. P. Ford and M. Silverman, Mechanistic Aspects of Environment Controlled Crack Propagation in Steel/Aqueous Environment Systems, General Electric Co. Report HTGE 451-8-12 (1979).

19. D. F. Mowbray, "Derivation of a Low-cycle Fatigue Relationship Employing the J-Integral Approach to Crack Growth," in Cracks and Fracture, ASTM STP 601, American Society for Testing and Materials, Philadelphia (1976), pp. 33-46.

20. F. P. Ford, "Mechanisms of Stress Corrosion Cracking," in Aspects of Fracture Mechanics in Pressure Vessels and Piping, PVP Vol. 58, American Society of Mechanical Engineers, New York (1982), p. 229.

21. E. W. Hart, Constitutive Relations for the Non-Elastic Deformation of Metals, J. Eng. Mater. Technol. 93(3), 193 (1976).

22. A. K. Miller and T. Tanaka, in Development of an Engineering Model for Predicting IGSCC Damage-Particularly in Type 304 Stainless Steel in BWR Water Environments, Electric Power Research Institute Report EPRI NP-2808-LD, prepared by S. Levy, Inc., Campbell, California (February 1983), pp. C-1 to C-43.

23. W. E. Ruther, W. K. Soppet, G. Ayrault, and T. F. Kassner, in Environmentally Assisted Cracking in Light Water Reactors: Annual Report, October 1981-September 1982, NUREG/CR-3292, ANL-83-27 (February 1983), pp. 66-82.

24. W. E. Ruther, W. K. Soppet, and T. F. Kassner, in Materials Science and Technology Division Light-Water-Reactor Safety Research Program: Quarterly Progress Report, October-December 1982, NUREG/CR-2970 Vol. IV, ANL-82-41 Vol. IV (November 1983), pp. 49-52.

25. J. Rest, The Prediction of Transient Fission-Gas Release and Fuel Microcracking Under Severe Core-Accident Conditions, Nucl. Technol. 56, 553-564 (March 1982).

26. J. Rest, Evaluation of Volatile and Gaseous Fission Product Behavior in Water Reactor Fuel Under Normal and Severe Core Accident Conditions, Nucl. Technol. 61(1), 33-48 (April 1983).

27. S. M. Gehl, The Release of Fission Gas During Transient Heating of LWR Fuel, ANL-80-108 (May 1982).

28. R. J. DiMelfi and L. W. Deitrich, The Effects of Grain Boundary Fission Gas on Transient Fuel Behavior, Nucl. Technol. 43, 328 (1979); see also ANL/RAS-78-32 (1978).

29. M. F. Wood and J. R. Matthews, On the Use of Grain Boundary Loss Terms in Fission Gas Release and Swelling Models, J. Nucl. Mater. 89, 53-61 (1980).

30. J. R. Matthews and M. H. Wood, An Efficient Method for Calculating Diffusive Flow to a Spherical Boundary, Nucl. Eng. Des. 56, 439-443 (1980).

31. J. Rest, M. Piasecka, and S. A. Zawadzki, in Materials Science Division Light-Water-Reactor Safety Research Program: Quarterly Progress Report, April-June 1982, NUREG/CR-2970 Vol. II, ANL-82-41 Vol. II (May 1983), pp. 60-71.

32. M. O. Marlowe and A. I. Kaznoff, "Fission Gas Re-Solution Mechanisms and Kinetics," in Proc. Intl. Conf. on Nuclear Fuel Performance (British Nuclear Energy Society, London, 1973), pp. 79.1-79.6.

33. J. A. Turnbull and M. O. Tucker, Swelling in UO_2 Under Conditions of Gas Release, Philos. Mag. 30, 47 (1972).

34. J. Rest, GRASS-SST: A Comprehensive, Mechanistic Model for the Prediction of Fission-Gas Behavior in UO_2-Base Fuels During Steady-State and Transient Conditions, ANL-78-53 (June 1978).

35. J. Rest and S. M. Gehl, The Mechanistic Prediction of Transient Fission-Gas Release from LWR Fuel, Nucl. Eng. Des. 56(1), 233-256 (1980).

36. H. M. Chung, in Materials Science and Technology Division Light-Water-Reactor Safety Research Program: Quarterly Progress Report, April-June 1982, NUREG/CR-2980 Vol. II, ANL-82-41 Vol. II (April 1983), pp. 72-78.

37. F. L. Yaggee, in Materials Science and Technology Division Light-Water-Reactor Safety Research Program: Quarterly Progress Report, July-September 1982, NUREG/CR-2970 Vol. III, ANL-82-41 Vol. III (June 1983), pp. 20-21.

38. D. H. Bradhurst and P. M. Heuer, The Influence of Oxide Stress on the Breakway Oxidation of Zircaloy-2, J. Nucl. Mater. 37, 35 (1970).

39. F. L. Yaggee, R. F. Mattas, and L. A. Neimark, Characterization of Irradiated Zircaloys: Susceptibility to Stress-Corrosion Cracking, Electric Power Research Institute Report EPRI NP-1155 (September 1979).

40. H. M. Chung, in Materials Science and Technology Division Light-Water-Reactor Safety Research Program: Quarterly Progress Report, October-December 1982, NUREG/CR-2940 Vol. IV, ANL-82-41 Vol. IV (November 1983), pp. 82-98.

41. H. M. Chung, "TEM-HVEM Observation of Ordered Zirconium-Oxygen Phase in Zircaloy Spent-Fuel Cladding", in Proc. Intl. Symp. on Environmental Degradation of Materials in Nuclear Power Systems-Water Reactors, August 22-24, 1983, Myrtle Beach, SC, in press.

42. P. M. Kelly and P. D. Smith, Strain-aging in Zirconium-Oxygen Alloys, J. Nucl. Mater. 46, 23 (1973).

43. W. R. Thorpe and I. O. Smith, Tensile Properties of Zr-1 wt% Nb Alloy, J. Nucl. Mater. 78, 49 (1978).

44. W. R. Thorpe and I. O. Smith, Static Strain Aging of Zr-1 wt% Nb Alloy, J. Nucl. Mater. 80, 35 (1979).

45. K. Veevers and U. K. Snowden, Strain Aging of Quenched Zircaloy-2, J. Nucl. Mater. 47, 311 (1973).

46. J. M. Williams, J. T. Stanley, and W. E. Brundage, The Interaction of Radiation Produced Defects and Interstital Impurity Atoms in Niobium, Oak Ridge National Laboratory Report ORNL-4097 (April 1967), pp. 30-41.

47. N. Igata, K. Miyahara, K. Ohno, and K. Hakomori, Detrapping of Nitrogen and Oxygen Atoms from Neutron Irradiation Induced Defects of Niobium During Post-Irradiation Annealing, J. Nucl. Mater. 108&109, 234 (1982).

48. M. S. Wechsler, D. G. Alexander, R. Bajaj, and O. N. Carlson, in Proc. Intl. Conf. on Defects and Defect Clusters in B.C.C. Metals and Their Alloys, August 14-16, 1973, Gaithersburg, MD, ed. R.J. Arsenault, pp. 127-146.

49. D. F. Hasson, "Anneal Hardening in Neutron Irradiated Vanadium Alloys," ibid., pp. 147-162.

50. R. P. Agarwala, B. M. Pande, and M. S. Anand, Interaction of Oxygen with Radiation-Induced Defects in Dilute Vanadium Alloys, J. Nucl. Mater. 108&109, 240 (1982).

51. P. R. Okamoto and H. Wiedersich, Segregation of Alloying Elements to Free Surface During Irradiation, J. Nucl. Mater. 53, 336 (1974).

52. H. Wiedersich, P. R. Okamoto, and N. Q. Lam, A Theory of Radiation-Induced Segregation in Concentrated Alloys, J. Nucl. Mater. 83, 98 (1979).

53. I. G. Ritchie and A. Atrens, The Diffusion of Oxygen in Alpha-Zirconium, J. Nucl. Mater. 67, 254 (1977).

54. A Trautwein and W. Gysel, Influence of Long Time Aging of CF8 and CF8M Cast Steel at Temperatures Between 300 and 500 Deg. C on the Impact Toughness and the Structure Properties, Spectrum, Technische Mitteilungen aus dem GF Konzern, No. 5, May 1981; Stainless Steel Castings, eds. V. G. Behal and A. S. Melilli, ASTM STP 756 (1982), p. 165.

55. E. I. Landerman and W. H. Bamform, Fracture Toughness and Fatigue Characteristics of Centrifugally Cast Type 316 Stainless Steel Pipe after Simulated Thermal Service Conditions, Ductibility, and Toughness Considerations in Elevated Temperature Service, ASME MPC-8 (1978), p. 99.

56. G. Baudry and C. Pichard, "Evolution During Long Holding Times at 300 and 450°C of the Mechnaical Properties of Austeno-Ferritic Steel Castings and Welded Joints Used in Pressurized Water Nuclear Reactors," Troisieme Congres National Sur La Technologie Des Appareils à Pression, Vol. 2, Materiaux, A.F.I.A.P. (1980), p. 673.

57. T. J. Nichol, A. Datta, and G. Aggen, "Embrittlement of Ferritic Stainless Steels," Metall. Trans. 11A, 573 (1980).

58. H. D. Solomon and L. M. Levinson, Mössbauer Effect Study of 475°C Embrittlement of Duplex and Ferritic Stainless Steels, Acta Met. 26, 429 (1978).

59. R. Lagneborg, Metallography of the 475°C Embrittlement in an Iron-30% Chromium Alloy, Trans. ASM 60, 67 (1967).

60. M. Courtnall and R. B. Pickering, The Effect of Alloying on 475°C Embrittlement, Met. Sci. J. 10, 273 (1976).

61. M. J. Marcinkowski, R. M. Fisher, and A. Szirmae, Effect of 500°C Aging on the Deformation Behavior of an Iron-chromium Alloy, Trans. AIME 230, 676 (1964).

62. M. J. Blackburn and J. Nulling, Metallography of an Iron-21% Chromium Alloy Subjected to 475°C Embrittlement, J. Iron Steel Inst. 202, 610 (1964).

63. A. Hendry, Z. F. Mazur, and K. H. Jack, Influence of Nitrogen on 475°C Embrittlement of High-chromium Ferritic Steels, Met. Sci. J. 13, 482 (1979).

64. P. D. Southwick and R. W. K. Honeycombe, Decomposition of Ferrite to Austenite in 26% Cr-5% Ni Stainless Steel, Met. Sci. J. 14, 253 (1980).

65. M. F. Ashby and L. M. Brown, Diffraction Contrast from Spherically Symmetrical Coherency Strains, Philos. Mag. 8, 1083 (1963).

Distribution for NUREG/CR-3689 Vol. I (ANL-83-85 Vol. I)

Internal:

R. P. Anderson
R. Avery
G. Ayrault
E. S. Beckjord
M. Blander
F. A. Cafasso
Y. S. Cha
O. K. Chopra
H. M. Chung
T. N. Claytor
L. W. Deitrich
C. E. Dickerman
D. R. Diercks
F. Y. Fradin
B. R. T. Frost
E. E. Gruber
G. L. Hofman
M. Ishii
W. D. Jackson
C. E. Johnson
T. F. Kassner (12)
K. L. Kliewer
J. M. Kramer
A. B. Krisciunas
D. S. Kupperman
Y. Y. Liu
P. A. Lottes
P. S. Maiya
L. McUmber
K. Natesan
L. A. Neimark
F. A. Nichols
F. S. Onesto
R. G. Palm
J. Y. Park
D. R. Pepalis
D. R. Perkins
R. B. Poeppel
J. J. Puro
K. J. Reimann
J. Rest (10)
W. E. Ruther
R. Schlueter
W. J. Shack (3)
W. K. Soppet
E. M. Stefanski (2)
R. P. Stein
R. V. Strain
C. E. Till
H. C. Tsai
R. A. Valentin
A. Villalobos
R. W. Weeks
H. Wiedersich
F. L. Yaggee
R. S. Zeno
ANL Patent Dept.
ANL Contract File
ANL Libraries (3)
TIS Files (6)

External:

NRC, for distribution per R3 and R5 (450)
DOE-TIC (2)
Manager, Chicago Operations Office, DOE
R. Tom, DOE-CH
Materials Science and Technology Division Review Committee:
B. Alcock, U. Toronto
A. Arrott, Simon Fraser U.
R. C. Dynes, Bell Labs., Murray Hill
A. G. Evans, U. California, Berkeley
L. M. Falicov, U. California, Berkeley
H. K. Forsen, Bechtel Group, San Francisco
E. Kay, IBM San Jose Research Lab.
B. Maple, U. California, San Diego
C. L. McCabe, Cabot Corp., Kokomo, Ind.
P. G. Shewmon, Ohio State U.
J. Tien, Columbia U.
R. B. Adamson, General Electric Co., Vallecitos Nuclear Center, P. O. Box 460, Pleasanton, Calif. 94566
P. L. Andresen, General Electric Corporate Research and Development, Schenectady, N. Y. 12301
G. A. Arlotto, Office of Nuclear Regulatory Research, USNRC, Washington
D. Atteridge, Battelle Pacific Northwest Lab., P. O. Box 999, Richland, Wash. 99352
W. Berry, Battelle-Columbus Labs., 505 King Ave., Columbus, O. 43201
J. Boulton, Whiteshell Nuclear Research Establishment, AECL, Pinawa, Manitoba, ROE 1LO, Canada
D. L. Burman, Westinghouse PWR Systems Div., P. O. Box 355, Pittsburgh, Pa. 15230
L. K. Chan, Office of Nuclear Regulatory Research, USNRC, Washington

C. Y. Cheng, Office of Nuclear Reactor Regulation, USNRC, Washington
R. A. Clark, Battelle Pacific Northwest Lab., P. O. Box 999, Richland, Wash. 99352
F. D. Coffman, Jr., Office of Nuclear Reactor Regulation, USNRC, Washington
W. J. Collins, Office of Inspection and Enforcement, USNRC, Washington
G. Cragnolino, Dept. of Metallurgical Engineering, Ohio State U., Columbus, O. 43210
D. Cubiciotti, Electric Power Research Inst., P. O. Box 10412, Palo Alto, Calif. 94304
J. C. Danko, Electric Power Research Inst., P. O. Box 10412, Palo Alto, Calif. 94304
B. J. Elliot, Office of Nuclear Reactor Regulation, USNRC, Washington
R. Foulds, Office of Nuclear Reactor Regulation, USNRC, Washington
M. Fox, Fox Enterprises, 7490 Stanford Place, Cupertino, Calif. 95014
Y. S. Garud, S. Levy, Inc., 1901 S. Bascom Ave., Campbell, Calif. 95008
S. M. Gehl, Electric Power Research Inst., P. O. Box 10412, Palo Alto, Calif. 94304
J. H. Gittus, Springfields Nuclear Power Development Labs., U. K. Atomic Energy Authority, Springfields, Salwick, Preston, PR4 ORR, England
D. O. Harris, 750 Welch Rd., Palo Alto, Calif. 94304
W. S. Hazelton, Office of Nuclear Reactor Regulation, USNRC, Washington
R. R. Hobbins, EG&G/INEL, 1520 Sawtelle Dr., Idaho Falls, Idaho 83401
R. E. Johnson, Office of Nuclear Reactor Regulation, USNRC, Washington
W. V. Johnston, Office of Nuclear Reactor Regulation, USNRC, Washington
R. L. Jones, Electric Power Research Inst., P. O. Box 10412, Palo Alto, Calif. 94304
K. R. Jordan, Nuclear Fuel Div., Monroeville Nuclear Center, Westinghouse Electric Corp., Monroeville, Pa. 15146
J. N. Kass, General Electric Co., 175 Curtner Ave., San Jose, Calif. 95125
E. Kohn, Atomic Energy of Canada Ltd., Sheridan Park Research Community, Mississauga, Ont., Canada L5K 1B2
P. M. Lang, Office of Converter Reactor Deployment, USDOE, Washington, D. C. 20545
D. D. Lanning, Battelle Pacific Northwest Lab., P. O. Box 999, Richland, Wash. 99352
R. A. Lorenz, Oak Ridge National Lab., P. O. Box X, Oak Ridge, Tenn. 37830
P. MacDonald, EG&G/INEL, 1520 Sawtelle Dr., Idaho Falls, Idaho 83401
G. P. Marino, Office of Nuclear Regulatory Research, USNRC, Washington
C. E. McCracken, Office of Nuclear Reactor Regulation, USNRC, Washington
S. McDonald, Westinghouse Electric Corp. R&D Center, Beulah Rd., Pittsburgh, Pa. 15235
K. R. Merckx, Exxon Nuclear, Inc., 2955 George Washington Way, Richland, Wash. 99352
A. C. Millunzi, Office of Breeder Reactor Programs, USDOE, Washington, D. C. 20545
J. Muscara, Office of Nuclear Regulatory Research, USNRC, Washington
D. M. Norris, Electric Power Research Inst., P. O. Box 10412, Palo Alto, Calif. 94304
D. R. O'Boyle, Commonwealth Edison Co., P. O. Box 767, Chicago, Ill. 60690
R. N. Oehlberg, Electric Power Research Inst., P. O. Box 10412, Palo Alto, Calif. 94304
M. F. Osborne, Oak Ridge National Lab., P. O. Box X, Oak Ridge, Tenn. 37830
D. E. Owen, EG&G Idaho, P. O. Box 88, Middletown, Pa. 17057

T. P. Papazoglou, Lynchburg Research Center, Babcock & Wilcox Co., P. O. Box 1260, Lynchburg, Va. 24505
J. T. A. Roberts, Electric Power Research Inst., P. O. Box 10412, Palo Alto, Calif. 94304
E. J. Rowley, Commonwealth Edison Co., P. O. Box 767, Chicago, Ill. 60690
E. F. Rybicki, Dept. of Mechanical Engineering, Univ. of Tulsa, Tulsa, Okla. 74110
R. A. Sallach, Sandia National Labs., Albuquerque, N. Mex. 87185
H. H. Scott, Office of Nuclear Regulatory Research, USNRC, Washington
C. Z. Serpan, Office of Nuclear Regulatory Research, USNRC, Washington
L. Shao, Office of Nuclear Regulatory Research, USNRC, Washington
R. D. Silver, Office of Nuclear Reactor Regulation, USNRC, Washington
P. Smerd, Combustion Engineering, Inc., P. O. Box 500, Windsor, Conn. 06095
A. A. Solomon, School of Nuclear Engineering, Purdue U., West Lafayette, Ind. 47907
A. Taboada, Office of Nuclear Regulatory Research, USNRC, Washington
B. Turovlin, Office of Nuclear Regulatory Research, USNRC, Washington
R. Van Houten, Office of Nuclear Regulatory Research, USNRC, Washington
R. A. Watson, Carolina Power and Light Co., P. O. Box 1551, Raleigh, N. C. 27602
J. R. Weeks, Brookhaven National Lab., Upton, N. Y. 11973
K. R. Wichman, Office of Nuclear Reactor Regulation, USNRC, Washington

NRC FORM 335 (11 81)

U.S. NUCLEAR REGULATORY COMMISSION

BIBLIOGRAPHIC DATA SHEET

1. REPORT NUMBER (Assigned by DDC)
NUREG/CR-3689 Vol. I
ANL-83-85 Vol. I

4. TITLE AND SUBTITLE (Add Volume No., if appropriate)
Materials Science and Technology Division Light-Water-Reactor Safety Research Program: Quarterly Progress Report January-March 1983

2. (Leave blank)

3. RECIPIENT'S ACCESSION NO.

7. AUTHOR(S)
W. J. Shack et al.

5. DATE REPORT COMPLETED
MONTH | YEAR

9. PERFORMING ORGANIZATION NAME AND MAILING ADDRESS (Include Zip Code)
Argonne National Laboratory
9700 South Cass Avenue
Argonne, Illinois 60439

DATE REPORT ISSUED
MONTH: April | YEAR: 1984

6. (Leave blank)

8. (Leave blank)

12. SPONSORING ORGANIZATION NAME AND MAILING ADDRESS (Include Zip Code)
Division of Reactor Safety Research
Office of Nuclear Regulatory Research
U.S. Nuclear Regulatory Commission
Washington, D. C. 20555

10. PROJECT/TASK/WORK UNIT NO.

11. FIN NO.
A2016, A2017, A2212, A2243

13. TYPE OF REPORT
Technical

PERIOD COVERED (Inclusive dates)
January-March 1983

15. SUPPLEMENTARY NOTES

14. (Leave blank)

16. ABSTRACT (200 words or less)

This progress report summarizes the Argonne National Laboratory work performed during January, February, and March 1983 on water reactor safety problems. The research and development areas covered are Environmentally Assisted Cracking in Light Water Reactors, Transient Fuel Response and Fission Produce Release, Clad Properties for Code Verification, and Long-Term Embrittlement of Cast Duplex Stainless Steels in LWR Systems.

17. KEY WORDS AND DOCUMENT ANALYSIS

17a. DESCRIPTORS

fission product modeling
fission product release
pipe cracking
water chemistry

17b. IDENTIFIERS/OPEN-ENDED TERMS

18. AVAILABILITY STATEMENT
Unlimited

19. SECURITY CLASS (This report)
unclassified

21. NO. OF PAGES
152

20. SECURITY CLASS (This page)
unclassified

22. PRICE
$

NRC FORM 335 (11 81)